# OPTICAL PHASE-MODULATED SYSTEMS: NUMERICAL ESTIMATION AND EXPERIMENTAL MEASUREMENT OF PHASE JITTER

A Dissertation
Presented to
The Academic Faculty

By

David Boivin

In Partial Fulfillment
of the Requirements for the Degree
Doctor of Philosophy
in
Electrical and Computer Engineering

School of Electrical and Computer Engineering
Georgia Institute of Technology
December 2006

# OPTICAL PHASE-MODULATED SYSTEMS: NUMERICAL ESTIMATION AND EXPERIMENTAL MEASUREMENT OF PHASE JITTER

Approved by:

Dr. Steve McLaughlin, Committee Chair
*Professor, School of ECE*
*Georgia Institute of Technology*

Dr. William Rhodes
*Professor, School of ECE*
*Georgia Institute of Technology*

Dr. Gee-Kung Chang, Advisor
*Professor, School of ECE*
*Georgia Institute of Technology*

Dr. Gisele Bennett
*Associate Professor, School of ECE*
*Georgia Institute of Technology*

Dr. John Barry, Advisor
*Associate Professor, School of ECE*
*Georgia Institute of Technology*

Dr. Michael Chapman
*Professor, School of Physics*
*Georgia Institute of Technology*

Date Approved: August 22, 2006

# DEDICATION

*To my parents Alain and José, my sister Gaëlle*

# ACKNOWLEDGMENTS

The research work presented in this manuscript has been done partly in Metz (Laboratoire FEMTO-ST/GTL-CNRS Telecom) and in Atlanta (Optical Networking Research Group, Georgia Institute of Technology). First, I would like to thank Jean-Pierre Goedgebuer for welcoming me to his lab and making me work under the thoughtful supervision of Marc Hanna to whom I am deeply grateful for his support, insightful guidance, enthusiasm, understanding and encouragement during all these years. I also want to thank my co-advisors, Professor John Barry and Gee-Kung Chang, who made my Ph.D work a positive and memorable experience. I would like to thank the members of my committee, Professors Steve McLaughlin, William Rhodes, Gisele Bennett, and Michael Chapman for their advice.

During these years, I met many persons now dear to me for very different reasons: Alexandre Soujaeff for our jazz listening/green tea sessions at le Port Saint-Marcel, before he leaves for Japan, Xavier and Lydie Bavard, for supporting and always being there for me, Jérôme and Muriel Vasseur, for listening always and their attention, Matthieu Bloch, for being a model in terms of rigor and perseverance, Nicolas Gastaud (Assistant Coach), for the millions of important favors given in Metz, Paris, and Atlanta, Johann Cussey, Yannick Phulpin, *yeehaaaa!* Matthias Messer, *jawohl*, Demijan Klinc, the last roommate but not the least ! To be completely honest, I will miss our everyday discussions on our respective interests . . . Good luck ! Badri Vellambi, if only more people were like him . . . Thank you for all our discussions and introducing me to Indian culture and philosophy, Arnaud Bistoquet (Coach), Alessandro Fais and his family, Will Leven and Maneli Noorkami, Martin Tobias, and Kevin Chan.

The team of the REES program (Ministère des affaires étrangères/JISTEC) and the Mitsubishi Lightwave Communications division in Ōfuna, particularly Ishida and Mizuochi san.

The staff in GTL: Josyane Roschitz, Florence Stoia, Audrey Steinbach, Sandrine Cadamuro.

My friends from Supelec: Olivier, Anthony, Arnaud, Elodie, Benoît, and Stéphane,

My other friends: Samuel Moec, Olivier Konne, Pierre-Ambroise Lacourt, Alexandre Locquet, Frédéric Patois, Aurélien Palavisini, Stéphane Poinsot, Stéphane Daunet, Deric Waters, Yogesh Sankarasubramaniam, David Miliner, Kevin McFall, Mike Haberman, Damien Nirousset, Nicolas Royer, Serge Grop, Stéphanie Barthes, Eva Bookjans, Xavier Le Faucheur, Olivier Hamard, Gregory Dubos, Guillermo Narsilio, Tommaso and Violetta Melodia, Dario Pompili, Nitin Suresh, Parasuram Rao, Arumugam C. Kannan, Prathap Muthana, Mina Sartipi, Sibel Yaman, Rajbabu Velmurugan, Ramanam and Arun Subramaniam, Nazanin and Reza Rahnavard.

My labmates in Atlanta: Arshad Chowdhury, Chunpeng Xiao, Claudio Estevez, Zhenshen Jia, Yin-Jung Chang, Muhammad Haris, and Oladeji Akanbi.

Finally, I would like to thank my whole family for constant support.

# TABLE OF CONTENTS

# LIST OF TABLES

# LIST OF FIGURES

# SUMMARY

There has recently been a renewed effort to develop coherent optical communication systems. In particular, differential phase-shift keying (DPSK), which does not require a local oscillator to perform decoding, is the focus of the attention and is perceived to be the promising candidate for future optical communication systems updates. This motivates us to exploit DPSK in wavelength-division multiplexed systems. First, modulation formats based on phase show an increased robustness to nonlinear impairments such as cross-phase modulation (XPM) and nonlinear polarization rotation, primarily because the time dependence of the optical power is deterministic and periodic. Second, coherent formats allow a higher spectral efficiency since both in-phase and quadrature dimensions of the signal space are available to encode information. Optical phase is also used in intensity-modulated direct detection systems as an extra degree of freedom, for example to provide better resistance to intrachannel four-wave mixing (FWM) or to increase spectral efficiency in duobinary modulation. Finally, phase modulation outperforms its intensity counterpart in terms of sensitivity since a 3 dB improvement can be achieved when balanced detection is used. Nevertheless, DPSK-based formats show a different behavior to noise accumulated along the propagation. Noise-induced power fluctuations are converted into phase fluctuations by the Kerr effect and become a penalty source that limits the transmission system reach. In this context, there have been intense research activities for evaluating phase uncertainties, but the previous studies assume an analytically determined pulse shape and a constant-dispersion optical link that is far from reflecting the actual and future structures of transmission lines. The objective of the proposed research is to investigate new and more efficient techniques in numerical evaluation and experimental measurement of phase jitter impact on more general communication systems, including dispersion management, filtering, and spectral inversion schemes.

# CHAPTER 1

# INTRODUCTION

1990: 1 Tbit/month,

2000: 35000 Tbit/month.

These two figures give an idea of the huge amount of data carried by the American backbone networks. It gives us perspectives on the challenges that the optical telecommunications industry had to face in the last ten years and will have to face in the future. Approximately doubling each year, the data traffic seems to follow an evolution comparable to Moore's law for semi-conductors. In this constant quest toward more and more efficient systems, wavelength-division multiplexing (WDM) has emerged as the enabling technique for the design of transmission lines with impressive capacities. In this context, each information channel is associated with a particular wavelength before being multiplexed and transmitted. Nevertheless, the usable range of wavelength (about 160 nm) is limited by optical amplification technology. The system is also limited by other constraints. During its propagation in the optical fiber, the signal is impaired by many factors that interact in a complex way: the chromatic dispersion, the nonlinear effects, and the amplified spontaneous emission (ASE) noise that occurs in optical amplifiers. Systems designs and their optimizations rely on fine trade-offs to minimize their deleterious consequences on the detected signal.

There has recently been a renewed effort to develop coherent optical communication systems, particularly differential phase-shift keying (DPSK) [4–6], which does not require a local oscillator to perform decoding. The motivation to use DPSK in wavelength-division multiplexed systems is two-fold. First, modulation formats based on phase show an increased robustness to nonlinear impairments such as cross-phase modulation [7] (XPM) and nonlinear polarization rotation [8], mostly because the time dependence of the optical

power is deterministic and periodic. Second, coherent formats may allow a higher spectral efficiency [9] since both in-phase and quadrature dimensions of the signal space are available to encode information. Optical phase is also used in intensity-modulated direct detection systems as an extra degree of freedom, for example to provide better resistance to intrachannel four-wave mixing [10] (FWM) or to increase spectral efficiency in duobinary modulation.

Nevertheless, the physical mechanism that limits performance in coherent systems is amplified spontaneous emission (ASE) noise-induced phase jitter [11]. Analytic derivations of the phase uncertainty for soliton systems were carried out using perturbation theory and the variational method. These studies assume an analytically determined pulse shape and a constant-dispersion optical link [12, 13]. These considerations motivated our research. Our objective is to investigate new and more efficient techniques for evaluating the impact of phase jitter on a more general communication system, including dispersion management, filtering, and/or midlink spectral inversion.

In Radio-Frequency (RF) communications, continuous phase modulated formats have already shown that they were spectrally efficient and tolerant to nonlinearities. However, they have not been implemented for optical communications yet and represent a potential candidates for the upgrade of WDM systems. On-Off signalling has always been used in phase-modulated systems resulting in abrupt switchings in the time domain that translate into large spectral side lobes outside of the main spectral band. We present the first implementation of a partial response optical continuous phase-modulated (CPM) system based on a 3 level (duobinary) phase response.

This manuscript is divided into 3 chapters. The first one introduces the basic notions of optical fiber communications from the ”simple” propagation medium to the full transmission line and its latest developments. The second chapter presents and further analyzes the main limitation of coherent modulation format: phase jitter. In particular, we propose

a semi-analytic approach that is valid for arbitrary pulses in dispersion-managed (DM) optical links following the methodology presented in [14]. This approach is validated by comparison with direct Monte Carlo simulations. We also characterize the impact of phase jitter on WDM transmissions and propose a new method for its measurement. Finally, the last chapter details the study and the experimental characterization of a novel modulation format based on phase modulation and duobinary signalling. Its performances are compared to its conventional counterparts in a 10 Gb/s recirculating loop experiment.

# CHAPTER 2

# OPTICAL COMMUNICATIONS SYSTEMS

The objective of this chapter is to give a general description of optical communications systems by starting from their basic elements, the optical fiber, then presenting the different techniques and concepts that allow the design of transmission lines and more general systems.

## 2.1 Optical fiber: transmission medium

### 2.1.1 Attenuation

Optical fiber is a suitable medium to transmit information in modern communication systems. Although the physical principles at the origin of the light confinement in the core of the fiber have been known from the XIX century, the field has only recently developed because of the refinement in the fiber fabrication process. Several factors play a role in the attenuation of this medium:

- the intrinsic absorption of the silica: if UV and IR vibrational resonances don't absorb much between 0.2 and 2 $\mu$m, residual impurities can lead to non negligible absorption levels. In particular, OH ions give the typical attenuation curve of the 90's (Figure 1) with two peaks at 1.23 and 1.4 $\mu$m. The constant improvement in the technique and fabrication process got rid off this constraint. Optical fibers were able to transmit from 1.26 to 1.62 nm with attenuations less than 0.5 dB/km.

- Rayleigh scattering: coming from the local variations of the refraction index, this effect proportional to $\lambda^{-4}$ is dominant at shorter wavelengthes and scatters the light in all directions. It gives the attenuation shown in dashed lines on Figure 1.

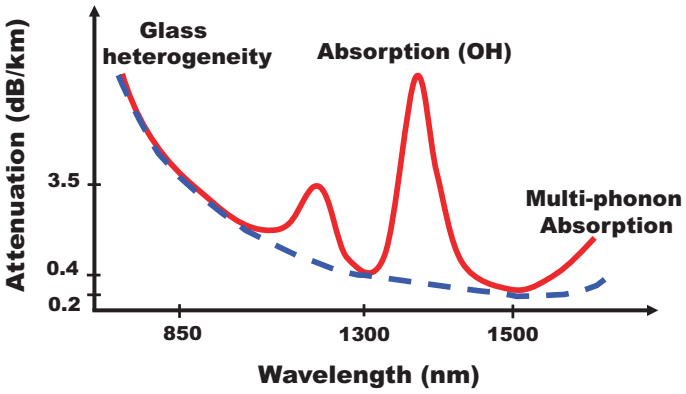


**Figure 1. Attenuation of a single mode fiber. The solid line represents the typical shape observed in the 90's, the dashed line represents the actual shape.**

The relation existing between the optical power transmitted at distance $z$ and the power initially injected defines the **linear** attenuation of the fiber $\alpha$

$$P(z) = P(0).e^{-\alpha z} \tag{1}$$

$\alpha$ is usually expressed in dB/km according to

$$\alpha_{dB} = -\frac{10}{z}\log(\frac{P(z)}{P(0)}) = \frac{10}{\ln 10}\alpha\ . \tag{2}$$

Nowadays, attenuation of standard fibers is about 0.2 dB/km at 1.55 $\mu$m, where it reaches its minimum value. One should also consider the losses due to microcurves and splicing.

### 2.1.2 Chromatic dispersion

The response of a dielectric medium to an electro-magnetic wave depends on its frequency $\omega$. The medium is said to be dispersive and its refraction index varies with wavelength. This property will play a crucial role in the propagation of short optical pulses because their different spectral components will travel at different speeds $\frac{c}{n(\lambda)}$, modifying their initial profile in the time domain. The resulting pulse broadening induces symbol interferences which limit the total reach of the communication system.

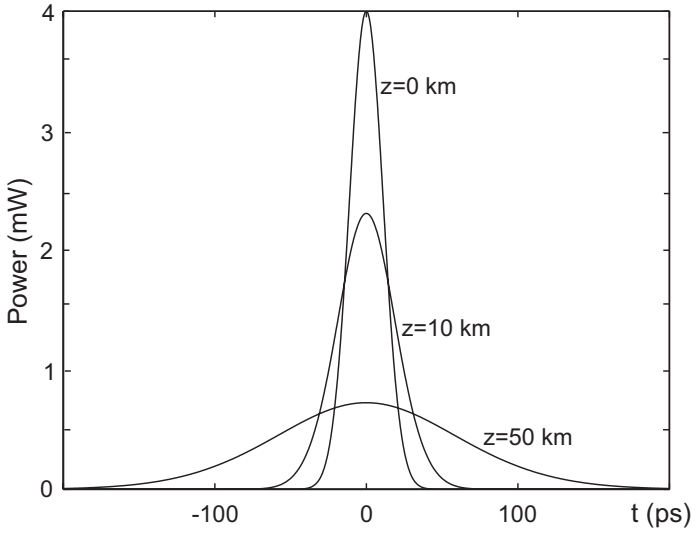


**Figure 2. Dispersion effect of a standard single mode fiber (D=16 ps/(nm.km)) on the temporal width of a Gaussian pulse. The launched pulse has a 4 mW peak power and a 20 ps temporal width at half maximum.**

For a quasi-monochromatic wave centered at pulsation $\omega_0$, the dispersion effects are mathematically expressed by developing its wave vector $\beta(\omega)$ around $\omega_0$

$$\beta(\omega) = n(\omega)\frac{\omega}{c} = \beta_0 + \beta_1(\omega - \omega_0) + \frac{1}{2}\beta_2(\omega - \omega_0)^2 + \frac{1}{6}\beta_3(\omega - \omega_0)^3 + ... \tag{3}$$

where $\beta_i = \left(\frac{d^i\beta}{d\omega^i}\right)_{\omega=\omega_0}$.

The pulse envelop propagates at group velocity $v_g = \frac{1}{\beta_1}$ whereas the coefficient $\beta_2$ represents the dispersion of this group velocity. Chromatic dispersion is often expressed by way of the dispersion parameter $D = \frac{d\beta_1}{d\lambda}$

$$D = \frac{d\beta_1}{d\lambda} = -\frac{2\pi c}{\lambda^2}\beta_2. \tag{4}$$

D is usually expressed in $ps/(nm.km)$ and $\beta_2$ in $ps^2/km$. According to the sign of D, one can distinguish between normal dispersion ($D < 0$ or $\beta_2 > 0$) –the red wavelengthes are travelling faster than the blue ones– and anormal dispersion. Single mode fibers (SMF) have zero dispersion around 1.31 $\mu$m. It is not the case in the 1.55 $\mu$m window where the attenuation is minimum. Nevertheless, there exists other types of fibers whose characteristics have been modified to have a dispersion profile different than the one of pure silica

(Figure 3). We have fibers with

- zero dispersion (DSF, *Dispersion Shifted Fiber*) or small dispersion (NZ-DSF, *Non-Zero Dispersion Shifted Fiber*) around 1.55 $\mu$m. The advantage of NZ-DSF lies in the considerable reduction of the nonlinear effects that require phase matching like FWM (*four-wave mixing*).

- constant dispersion over a large window (DFF, *Dispersion Flattened Fiber*).

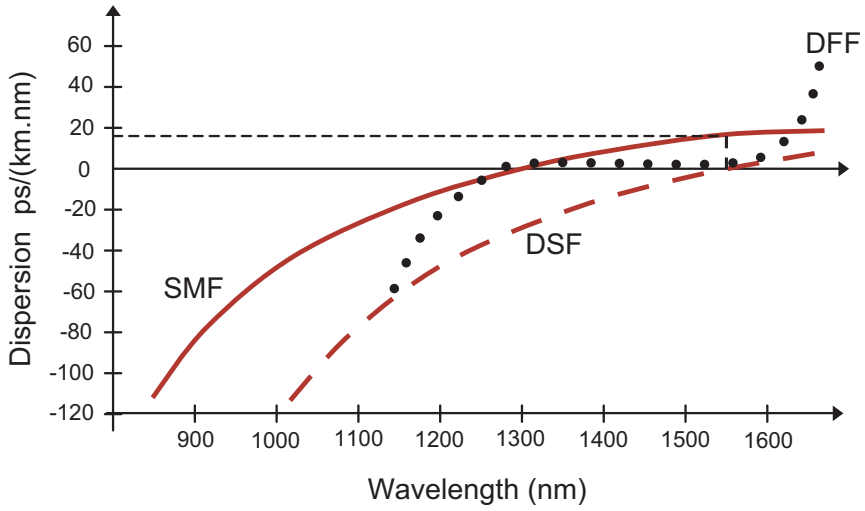


**Figure 3. Dispersion profile of various type of fiber. SMF: single mode fiber, DSF: dispersion shifted fiber, DFF: dispersion flattened fiber.**

### 2.1.3 Nonlinear effects

The goal of this paragraph is to present the different phenomena occurring in a fiber where high optical powers are confined in 50 to 65 $\mu m^2$. In this case, the response of the dielectric medium to this intense electro-magnetic field is nonlinear. We will make the distinction between inelastic and elastic nonlinearities whether there is respectively an exchange of energy with the medium or not.

#### *2.1.3.1 Electro-magnetic description:*

In a dielectric medium where an external electric field is applied, the effective electric field **D**(**r**,t) is linked with the apparition of elementary bipolar moments **p**(t) induced by the

opposite movement of the equilibrium positions of the linked charges. The macroscopic polarization field **P**(**r**,t) is the average bipolar moment per volume unit. The nonlinear response of the medium is expressed by a nonlinear polarization field **P** which satisfies the development

$$\mathbf{P} = \epsilon_0 \chi^{(1)} \times \mathbf{E} + \epsilon_0 \chi^{(2)} \times \mathbf{EE} + \epsilon_0 \chi^{(3)} \times \mathbf{EEE} + ... \tag{5}$$

where $\chi^{(i)}$ is a $(i+1)^{th}$ order tensor.

The amorphous characteristic of silica makes all the even order of nonlinear polarizations zero. In particular, $\chi^{(2)} = 0$ and we will consider the terms of higher than the $3^{rd}$ order as negligible. We then have

$$\mathbf{P} = \underbrace{\epsilon_0 \chi^{(1)} \times \mathbf{E}}_{\mathbf{P}_L(\mathbf{r},t)} + \underbrace{\epsilon_0 \chi^{(3)} \times \mathbf{EEE}}_{\mathbf{P}_{NL}(\mathbf{r},t)} . \tag{6}$$

Although $\chi^{(3)}$ is small, it will be responsible for most of the nonlinear effects occurring during the electric field propagation. Highly confined in the core of the fiber, it will create high power densities. Moreover, the large interaction distances (around 20 km for a 0.2 dB/km attenuation) play a key role in the manifestation of the nonlinear effects.

#### *2.1.3.2 $\chi^{(3)}$ effects: the optical Kerr effect*

The $\chi^{(3)}$ coefficient is at the origin of the 3 main elastic nonlinear effects:

- Self phase modulation (SPM)
- Cross phase modulation (XPM)
- Four wave mixing (FWM)

Considering the propagation equation directly derived from the Maxwell equations

$$\Delta \mathbf{E} - \frac{1}{c^2} \frac{\partial^2 \mathbf{E}}{\partial t^2} - \mu_0 \frac{\partial^2 \mathbf{P}}{\partial t^2} = \mathbf{0} , \tag{7}$$

we can also write according to Equation (6)

$$\Delta \mathbf{E} - \frac{1}{c^2}(1 + \chi^{(1)}).\frac{\partial^2 \mathbf{E}}{\partial t^2} - \mu_0 \frac{\partial^2 \mathbf{P}_{NL}}{\partial t^2} = \mathbf{0}. \tag{8}$$

Using the approximation of a slowly varying envelope, **E** is written as

$$\mathbf{E}(\mathbf{r},t) = \frac{1}{2}\left[\, E(\mathbf{r},t)\,.\,e^{-j\omega_0 t} + c.c\,\right]\mathbf{x} \tag{9}$$

where E(**r**,t) is slowly depending on time when compared with the optical period and **x** the polarization direction. One obtains the same type of expressions for $\mathbf{P}_L(\mathbf{r},t)$ and $\mathbf{P}_{NL}(\mathbf{r},t)$:

$$\mathbf{P}_L(\mathbf{r},t) = \frac{1}{2}\left[\, P_L(\mathbf{r},t)\,.\,e^{-j\omega_0 t} + c.c\,\right]\mathbf{x} \tag{10}$$

$$\mathbf{P}_{NL}(\mathbf{r},t) = \frac{1}{2}\left[\, P_{NL}(\mathbf{r},t)\,.\,e^{-j\omega_0 t} + c.c\,\right]\mathbf{x} \tag{11}$$

When (9) is substituted in (6) with the hypothesis of an instantaneous nonlinear response, the expression of $\mathbf{P}_{NL}(\mathbf{r},t)$ contains two terms oscillating at $\omega_0$ and $3\omega_0$. The last term requires phase-matching which is difficult to satisfy in the fiber. It will later be neglected. Using (11), $P_{NL}(\mathbf{r},t)$ is given by

$$P_{NL}(\mathbf{r},t) \approx \epsilon_0 \epsilon_{NL} E(\mathbf{r},t) \tag{12}$$

where the nonlinear contribution to the dielectric constant is defined by

$$\epsilon_{NL} = \frac{3}{4}\chi^{(3)}_{xxxx}\,|E(\mathbf{r},t)|^{\,2}\,. \tag{13}$$

Obtaining the propagation equation for the slowly varying envelope $E(\mathbf{r},t)$ in the frequency domain is not possible in general because $\epsilon_{NL}$ depends on the intensity. As the nonlinear effects are weak, the nonlinear polarization $\mathbf{P}_{NL}$ is considered as a small perturbation for the total induced polarization. This approach allows us to view $\epsilon_{NL}$ as a constant when deriving the propagation equation. Substituting $P_{NL}(\mathbf{r},t)$ in (8) and taking the Fourier transform, we have

$$\Delta\tilde{E} - \epsilon(\omega)\frac{\omega^2}{c^2}\,\tilde{E} = 0 \tag{14}$$

where the dielectric constant $\epsilon(\omega)$ is defined by $\epsilon(\omega) = 1 + \chi^{(1)}_{xx}(\omega) + \epsilon_{NL}$.

The refraction index also depends on the intensity:

$$n = n_L + n_2|E|^{\,2} \text{ avec } n_2 = \frac{3}{8n}\mathcal{R}e\{\chi^{(3)}_{xxxx}\}. \tag{15}$$

The propagation equation is solved by searching a separated variables solution of the following form

$$\tilde{E}(\mathbf{r},\omega) = F(x,y)\,\tilde{A}(z,\omega)\,.\,e^{j\beta_0 z}\,. \tag{16}$$

Neglecting dispersion, the perturbation theory gives the evolution of the slowly varying envelope $A(z,t)$ to the first order [15]

$$\frac{\partial A}{\partial z} - j\gamma|A|^2 A = 0 \tag{17}$$

with $\gamma = \dfrac{n_2\,\omega}{A_{eff}\,c}$ and $A_{eff}$ being the fiber effective mode area.

*2.1.3.3 Self phase modulation (SPM):*

Mathematically, the solution of (17) is

$$A(z,t) = A(0,t)\,.\,e^{-j\gamma|A(0,t)|^2 z}. \tag{18}$$

During the propagation, the time dependence of the electric field intensity $|E|^2$ induces, via the nonlinearity of the refraction index $n$, a phase shift proportional to $|E|^2$, hence the name of self phase modulation to describe this phenomenon. The instantaneous frequency –proportional to the derivative of the phase with respect to time– is also depending on time

$$\nu(z,t) \sim \frac{\partial \phi_{NL}}{\partial t} = \gamma\, z\,.\,\frac{d|A(0,t)|^2}{dt}\,, \tag{19}$$

and we observe its shift called chirp. The chirp respectively consists in a red/blue frequency shift at the beginning/end of the optical pulse. In other words, the SPM effect is a parasite frequency modulation which increases/decreases the instantaneous frequency at the rising/trailing edge of the pulse (Figure 4).

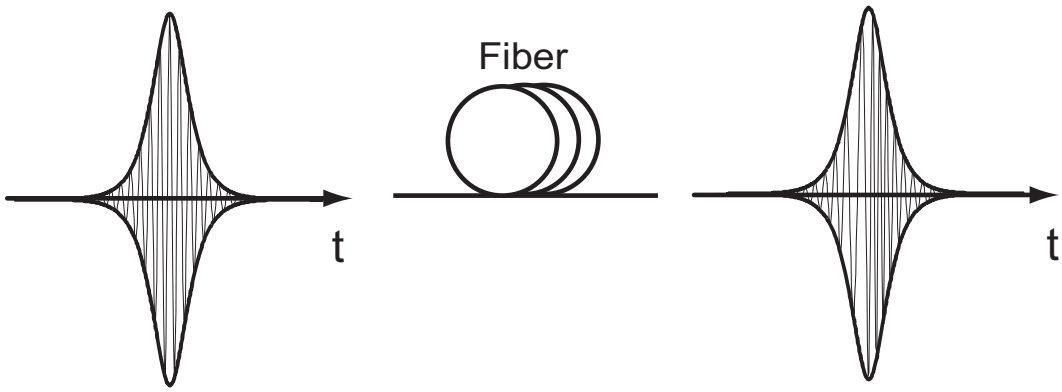


**Figure 4. SPM effect on a short pulse.**

The chirp results in a broadened optical spectrum. The broadening is increased with distance and the briefness of the optical pulse. This effect is represented on Figure 5 when a picosecond Gaussian pulse (20 ps at half width maximum) with a high peak power (6 mW) is launched in a DSF fiber.

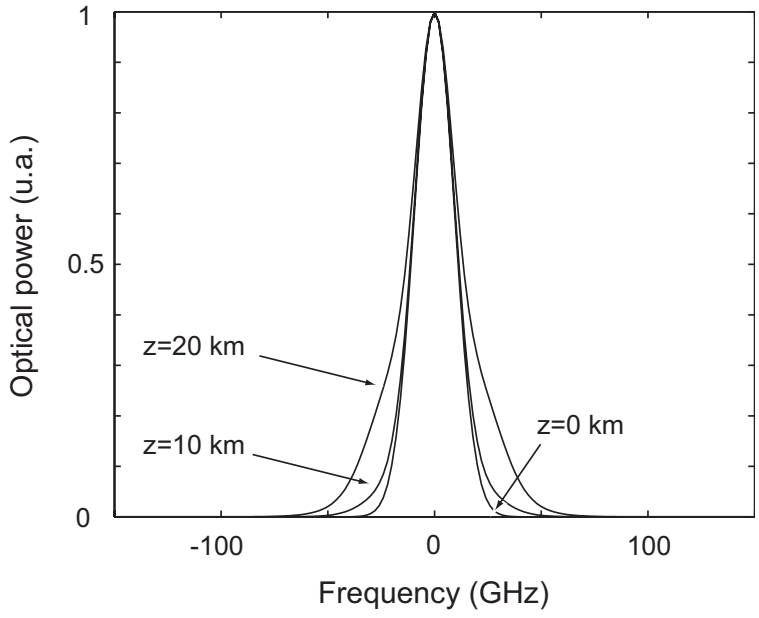


**Figure 5. SPM effect on a picosecond Gaussian pulse propagating in a DSF fiber with nonlinear index** $n_2 = 3.10^{-20}\ m^2$**/W.**

*2.1.3.4 Cross phase modulation (XPM):*

In the case where chromatic dispersion is neglected, the fiber can couple two signals which have different wavelengths or polarizations without any energy transfers between them. In the case of two different wavelengths, the XPM effect occurs because the refraction index $n^1$ effectively seen by the electric field $\mathbf{E}_1$ in the nonlinear medium not only depends on its intensity but also on its neighbor $\mathbf{E}_2$ propagating with him at the same time

$$n^1 = n_L + n_2(|E_1|^2 + 2|E_2|^2)\,. \tag{20}$$

The factor 2 in the last equation shows that, with equal intensity, XPM is twice as effective as SPM. The XPM effect is revealed by the pump/probe technique [16] in which the distortion level induced by a modulated channel (pump $\lambda_{pump}$) on its constant intensity neighbor (probe $\lambda_s$). The XPM-induced phase modulation is converted into an intensity modulation through the fiber chromatic dispersion after 5 spans of 60 km of SMF exactly compensated by 12 km of DCF ($\beta_2 = 108.5$ ps$^2$/km). The two channels are 50 GHz spaced.

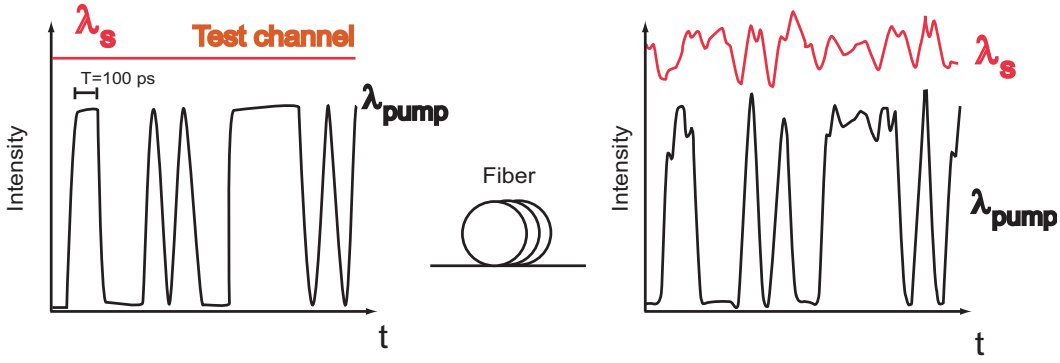


**Figure 6. XPM effect on a non-modulated signal.**

In the case where the two signals have the same wavelength but orthogonal polarizations $E_x$ and $E_y$, the fiber shows a nonlinear birefringence. It affects the refractive index seen by $E_x$ as follow

$$n_x = n_L + n_2(|E_x|^2 + \frac{2}{3}|E_y|^2)\,. \tag{21}$$

*2.1.3.5 Four wave mixing (FWM):*

Four wave mixing is the intermodulation product resulting from the interaction of several fields at different frequencies. In general, two fields called pumps interact with a third one called signal. When two pump photons are annihilated, two photons are created: the first one at the signal frequency, the other one at a complementary frequency called idler (Figure 7 a). In a WDM context, this resulting power transfer impairs the transmission since it produces a crosstalk between the channels [17]. Nevertheless, this process requires a phase-matching condition that is not spontaneously satisfied when the local chromatic dispersion is non zero. For this reason (Figure 7 b), FWM will not be the dominant nonlinear effect in our study.

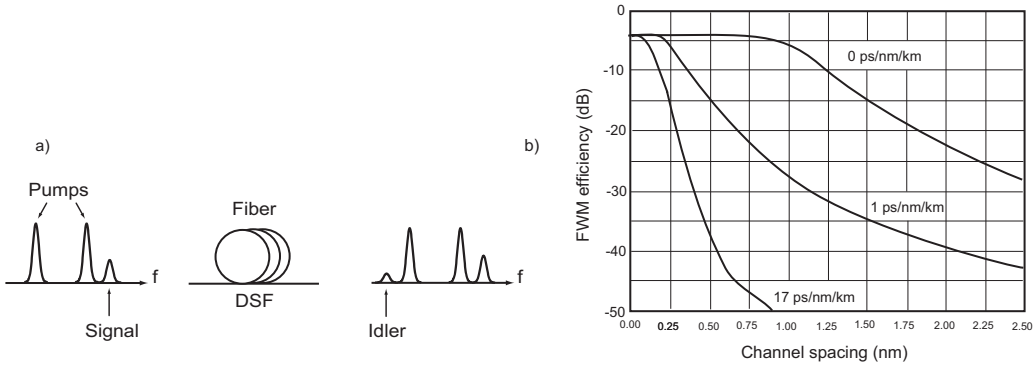


**Figure 7. (a) FWM effect in the spectral domain after the propagation of the signal and the two pumps in DSF fiber (b) FWM efficiency as a function of the channel spacing for various dispersion values.**

However, it is exploited in various applications such as frequency conversion, demultiplexing or parametric amplification. Finally, phase conjugation is an inherent property of FWM which is particularly useful [18–20]. It will later be studied in section 3. A pump $A_p$ and a signal $A_s$ respectively at frequencies $\omega_p$ and $\omega_s$ are injected into a DSF fiber whose zero dispersion wavelength matches the pump frequency. In this case, the phase-matching condition

$$k_c = 2k_p - k_s \text{ avec } k_j = \frac{n(\omega_j)\,\omega_j}{c}\,, \tag{22}$$

where $k_j$ is the wave vector of the optical field at frequency $\omega_j$, is approximately verified

and the fiber nonlinearity generates the conjugated signal $A_c$ at frequency $\omega_c = 2\omega_p - \omega_s$ [21] according to

$$\frac{dA_c}{dz} = -\frac{\alpha}{2}A_c + \gamma|A_p|^2 A_s^* \,. \tag{23}$$

The power converted into the phase conjugated signal $A_c$ (Figure 8) is proportional to the signal power and to the square of the pump power.

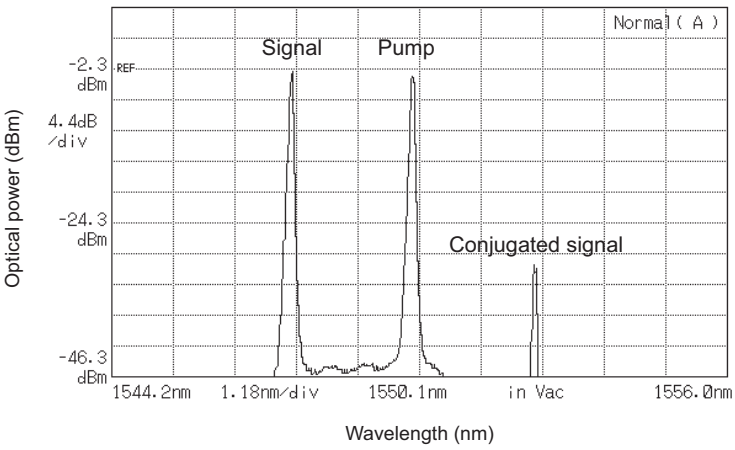


**Figure 8. Optical spectrum measured at the output of a DSF fiber after nonlinear interaction of a signal and a pump (resolution of the spectrum analyser: 0.1 nm).**

*2.1.3.6 Inelastic nonlinearities: interaction of the optical field with the medium*

We will now focus on the nonlinear effects resulting from the interaction of the optical field with the propagation medium. Through inelastic stimulated scattering, an incident photon (pump) is converted to a new photon (Stokes wave) with a lower frequency, hence a lower energy. The difference in energy is transmitted to the medium through an acoustic wave (phonon). According to the acoustic or optical nature of the phonon, one distinguishes two effects occurring when the incident light exceeds a given threshold for each effect:

- Stimulated Brillouin scattering: it occurs when an acoustic phonon is emitted. In this case, the Stokes wave is generated at an 11 GHz lower frequency, mainly in the opposite direction of the pump. This means that the fiber output power no longer

varies linearly with the incident power but reaches a threshold beyond which the excess is entirely reflected[1]. This retro-scattering has a narrow bandwidth (up to 10 MHz around 1.55 $\mu$m) which only concerns intense continuous sources[2]. In our work, as the pulse width is inferior to 1 ns, the required power to get a significant scattering is not confined in this band, therefore we neglect this effect.

- Stimulated Raman scattering (SRS): it occurs when an optical phonon is emitted. In this case, the generated Stokes wave, co- or contra-propagative, is produced a frequency 13 THz lower than the pump one. If the bandwidth of this effect is greater (around 7 THz), it will only impact the propagation if the spectrum of the pulses is greater than 13 THz: for intense pulses shorter than 1 ps – in this case the blue part of the signal acts as a pump for its red part – or if the spectrum contains wawelengths spaced by this interval.

#### *2.1.3.7 Polarization mode dispersion (PMD):*

Amorpheous by nature, silica does not show any birefringence. Nevertheless, the increase in the transmission bit rate made the problem related to polarization mode dispersion appear because in practice, many factors (mechanical or thermal constraints ...) disrupt the symmetry of the fiber which guaranteed the propagation of a fundamental mode degenerated in polarization. The fiber is then assimilated to a birefringent medium which locally has two orthogonal polarization states with different group velocities. A pulse will propagate though those two axes with different group velocities. The differential group delay (DGD) $\Delta\tau$ between the two modes (Figure 9) results in a time broadening at the detection. In opposition to chromatic dispersion, stable and perfectly known, PMD has a random evolution in time. One can show that the average DGD increases with the square root of the fiber length [22]. The specifications of some commercial fibers are given in Table 1.

[1] In actual fibers, the threshold is about 10 mW but can largely be increased if the pump spectrum is spread.

[2] It has been the case for the pump used to perform the phase conjugation shown on Figure 8 to get a higher efficiency.

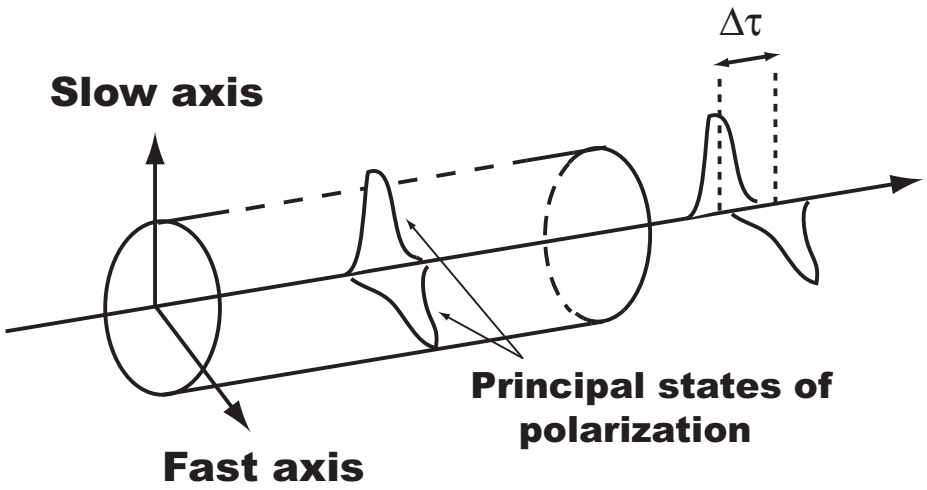


**Figure 9. PMD effect on an optical pulse.**

**Table 1. Parameters of different comercial fibers at 1550 nm according to [1].**

| Fiber | Manufacturer | D $ps/(km.nm)$ | S $ps/(km.nm)^2$ | $\alpha_0$ $dB/km$ | $A_{eff}$ $\mu m^2$ | PMD $ps/\sqrt{km}$ |
|---|---|---|---|---|---|---|
| TrueWave™ RS | Lucent | 4.5 | 0.045 | 0.22 | 55 | $< 0.1$ |
| LEAF™ | Corning | 4.2 | 0.09 | 0.22 | 72 | $< 0.1$ |
| TeraLight™ Ultra | Alcatel | 8 | 0.052 | $< 0.22$ | 63 | $< 0.04$ |
| Standard | Lucent, Corning Furukawa | 16.9 | 0.055 | 0.23 | 87 | $< 0.1$ |
| Under-sea | Lucent | $-3.1$ | 0.05 | 0.215 | 50 | $< 0.1$ |
| Deeplight™ | Pirelli | $-2.2$ | $< 0.12$ | $< 0.23$ | 70 | $< 0.1$ |
| Teralight™ Metro | Alcatel | 8 | 0.058 | $< 0.25$ | 63 | $< 0.08$ |
| DCF | Lucent | $-100$ | $-0.22$ | 0.5 | 20 | $< 0.25$ |
| WB-DCF | Lucent | $-95$ | $-0.33$ | 0.5 | 19 | $< 0.25$ |
| HS-DCF | Lucent | $-100$ | $-0.67$ | 0.68 | 15 | $< 0.25$ |

### 2.1.4 Propagation

After the review of the different phenomena occurring in the fiber, we will derive the equation governing the propagation of the electric field envelope in this medium starting from the dispersion equation

$$k = \frac{n\,\omega}{c} \text{ with } n(\omega) = n_L(\omega) + n_2(\omega)\,.\,|E|^{\,2}\,. \tag{24}$$

For a wave packet which central frequency $\omega_0$ travels at the speed $v_g = \left[\frac{\partial\omega}{\partial k}\right]_{\omega_0}$, we can write the following limited development

$$k(\omega) = k_0 + \left[\frac{\partial k}{\partial\omega}\right]_{\omega_0}\,.\,(\omega-\omega_0) + \frac{1}{2}\left[\frac{\partial^2 k}{\partial\omega^2}\right]_{\omega_0}\,.\,(\omega-\omega_0)^2 + o\left((\omega-\omega_0)^2\right) + \overbrace{\frac{\partial k_0}{\partial|E|^2}\,.\,|E|^2}^{\text{Non Linarit}} \tag{25}$$

which gives

$$K = k - k_0 \simeq k_0^{'}\,.\,(\omega-\omega_0) + \frac{1}{2}\,k_0^{''}\,.\,(\omega-\omega_0)^2 + \frac{\partial k_0}{\partial|E|^2}\,.|E|^2. \tag{26}$$

- $k_0^{'}$, $k_0^{''}$ can be computed using (24).

- $\dfrac{\partial k_0}{\partial|E|^2} = \left[\dfrac{\partial k}{\partial|E|^2}\right]_{\omega=\omega_0} = \left[\dfrac{\omega}{c}\,n_2(\omega)\right]_{\omega=\omega_0} = \dfrac{\omega_0}{c}\,n_2(\omega_0).$

Defining $\Omega$ as $\Omega = \omega - \omega_0$, we get

$$K \simeq k_0^{'}\Omega + \frac{1}{2}k_0^{''}\Omega^2 + \frac{\omega_0}{c}\,n_2(\omega_0)\,.\,|E|^2. \tag{27}$$

With the classical time-frequency equivalence

$$\begin{cases} K \;\sim\; -j\dfrac{\partial}{\partial z} & (28) \\[2ex] \Omega \;\sim\; +j\dfrac{\partial}{\partial t}, & (29) \end{cases}$$

we write the equality between operators

$$-j\frac{\partial}{\partial z} \simeq k_0^{'}j\frac{\partial}{\partial t} - \frac{1}{2}\frac{\partial^2}{\partial t^2} + \frac{\omega_0}{c}\,n_2(\omega_0)\,.\,|E|^2 \tag{30}$$

and apply it to the complex amplitude $E(z,t)$

$$j\left[\frac{\partial}{\partial z} + k_0^{'}\frac{\partial}{\partial t}\right]E - \frac{1}{2}\,k_0^{''}\,\frac{\partial^2 E}{\partial t^2} + \frac{\omega_1}{c}\,n_2(\omega_0)\,.\,|E|^2 E = 0. \tag{31}$$

If we write the last equation in the referential which moves at the average group velocity ($\tau = t - k_0^{'}z$), we get the propagation equation on the form used in [15] and which corresponds to the nonlinear Schrödinger equation

$$\frac{\partial A}{\partial z} + \frac{i}{2}\beta_2\frac{\partial^2 A}{\partial t^2} - i\gamma|A|^2 A = 0 \tag{32}$$

where A is the slowly varying complex envelope of the electric field, $\beta_2$ and $\gamma$ are previously defined.

If this equation takes the dispersion and SPM effects into account, it implicitly supposes a lossless medium and is therefore not valid in many situations. That is why a generalized Schrödinger equation is defined. In the limit of our experimental work, it includes the terms coming from the optical amplification (gain $g$, noise $\hat{F}(z,t)$), the third order dispersion ($\beta_3$) and the optical filtering caracterized by the filtering factor $b(z)$. We will later derive this factor from the characteristics of filter

$$i\frac{\partial A}{\partial z} - \frac{1}{2}\left[\beta_2(z) - ib(z)\right]\,.\,\frac{\partial^2 A}{\partial t^2} + \frac{\beta_3}{6}\,\frac{\partial^3 A}{\partial t^3} + \gamma(z)\,|A|^2 A = i\,g(z)\,u + \hat{F}(z,t)\,. \tag{33}$$

Depending on the the shape of the optical pulse and the operating wavelength, chromatic dispersion and SPM can take different signs. It suggests the existence of a state where the SPM would balance the chromatic dispersion effects. The Kerr effect would maintain in phase the different frequency components broadened by dispersion. This is realized in the abnormal regime where the dispersion tends to lead back to the pulse center the frequencies created by the Kerr effect at its sides (Figure 10). Stable solutions to (32) rise from this equilibrium and are called solitons.

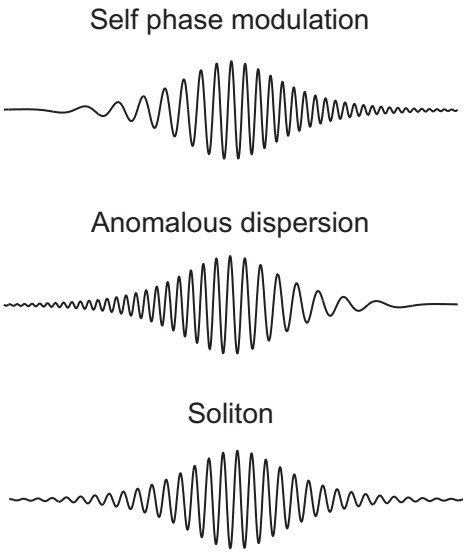


**Figure 10. Soliton, produced by the interaction between the Kerr effect and the chromatic dispersion.**

In the literature, another form for the NLSE is often seen and is obtained by normalizing

$$Z = \frac{z}{z_0}\ ,\ T = \frac{\tau}{\tau_0}\ ,\ q = \sqrt{\frac{n_2\omega_1 z_0}{c}}E \text{ et } z_0 = -\frac{\tau_0^2}{k_0''}\ . \tag{34}$$

This leads to a more condensed form often used in theoretical studies

$$j\frac{\partial q}{\partial Z} + \frac{1}{2}\frac{\partial^2 q}{\partial T^2} + |q|^2 q = 0. \tag{35}$$

### 2.1.5 Numerical simulations: the split-step Fourier algorithm

In simple cases, the inverse scattering theory (IST) provides analytical solutions for the NLSE (32). Nevertheless, its complexity and its restricted applications compared to the realistic models we want to study give the major role to numerical simulations done with the split-step Fourier algorithm. Easily scalable (third order dispersion, higher order nonlinear effects, filtering ...), this algorithm allows the prediction of the system performances and, in our case, the validation of the different analytical approaches used. The idea [15] is to consider the two majors impairments, SPM and dispersion, as independent on an elementary distance *dz*. So one solves Equation (32) only considering the chromatic dispersion

($\frac{\partial A}{\partial z} + \frac{i}{2}\beta_2 \frac{\partial^2 A}{\partial t^2} = 0$), then only the Kerr effect ($\frac{\partial A}{\partial z} - i\gamma|A|^2 A = 0$). These two equations are analytically solved in the Fourier domain, time domain respectively for the dispersive and nonlinear parts. Mathematically, it is equivalent to computing the limited development ($h \to 0$) of the exact solution

$$A(z+h,T) = e^{h(\hat{D}+\hat{N})}\, A(z,T) \tag{36}$$

of the NLSE expressed in the following form

$$\frac{\partial A}{\partial z} = (\hat{D} + \hat{N})\, A \tag{37}$$

where $\hat{D}$ and $\hat{N}$ are the differential operators for dispersion and nonlinearity.

$$\begin{cases} \hat{D} &= -\dfrac{i}{2}\beta_2 \dfrac{\partial^2}{\partial t^2} + \dfrac{1}{6}\beta_3 \dfrac{\partial^3}{\partial t^3} - \dfrac{\alpha}{2} \\ \\ \hat{N} &= i\gamma|A|^2. \end{cases} \tag{38}$$

For two non commutative operators, the Baker-Hausdorff formula is given by

$$e^{\hat{a}}\,.\,e^{\hat{b}} = e^{\hat{a}+\hat{b}+\frac{1}{2}[\hat{a},\hat{b}]+\frac{1}{12}[\hat{a}-\hat{b},[\hat{a},\hat{b}]]+\ldots} \tag{39}$$

with $[\hat{a},\hat{b}] = \hat{a}\hat{b} - \hat{b}\hat{a}$. To the first order, we get $e^{\hat{a}} \cdot e^{\hat{b}} \simeq e^{\hat{a}+\hat{b}}$ and the first neglected term

$$\frac{1}{2}\left[\hat{a},\hat{b}\right] = \frac{1}{2}h^2\left[\hat{D},\hat{N}\right]$$

gives an $h^2$ precision for the algorithm. In practice, the previous development is used to provide a numerical expression for $A(z+h,T)$. The exponential is computed in the Fourier domain according to

$$e^{h\hat{D}}\,.\,B(z,T) = \{\mathcal{F}^{-1} e^{h\hat{D}(i\omega)} \mathcal{F}\}\, B(z,T) \tag{40}$$

The fast techniques available to compute the FFT make the split-step Fourier algorithm faster than other methods such as finite differences. In the Fourier domain, the expression for $\hat{D}$ is reduced to the computation of a complex number following the equivalence

$\frac{\partial}{\partial t} \longleftrightarrow j\omega$. The accuracy can easily be improved. Instead of computing the nonlinear then the dispersion effects on a distance $h$, one can use a symmetric version which consists in first computing the dispersion effect on $\frac{h}{2}$, then applying the nonlinear effects on $h$ before computing the dispersion effects on the second half $\frac{h}{2}$ according to

$$A(z+h,T) \simeq e^{\frac{h}{2}\hat{D}} \,.\, e^{\hat{N}} \,.\, e^{\frac{h}{2}\hat{D}} A(z,T). \tag{41}$$

If the number of FFT to compute is doubled, one can show that the error is now proportional to $h^3$. We will use this modified algorithm in our work.

## 2.2 From the optical fiber to the transmission line

Until now, we have just focused on the description and the modeling of the physical phenomena occurring in the fiber when an intense electric field is propagating. In this paragraph, the idea is to present the different technical solutions that allowed to get rid off some physical constraints and limitations (attenuation, chromatic dispersion) . . . at least partially and to propose the design of real transmission lines.

### 2.2.1 Optical amplification

#### *2.2.1.1 Fiber-doped amplifier*

Rare earth fiber-doped amplifiers appeared in the beginning of the 90's [23]. They amplify the optical signal using the stimulated emission of the "rare earth" ions doping the core of the fiber and that have previously been excited by a pump (Figure 11).

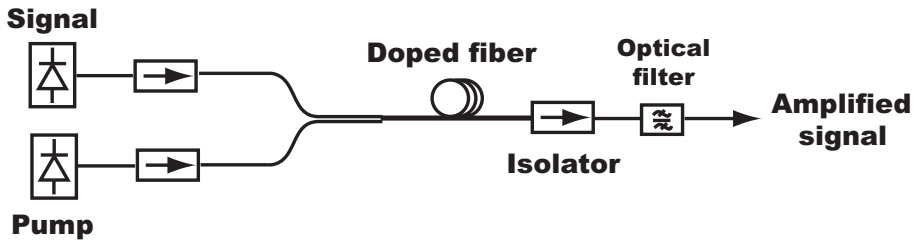


**Figure 11. Scheme of a fiber-doped amplifier.**

In the case of an erbium-doped fiber amplifier (EDFA), the energy from the pump operating at one of the absorption wavelengths of the erbium ion (980 – 1480 nm) is absorbed. The excited erbium ions are stimulated by any signal around 1.5 $\mu$m that is injected in the fiber. The stimulated ion emits one photon which has the same state than the one which returns to the fundamental state. At the same time, a spontaneous emission (SE) is generated in the fiber with or without the presence of any signal. This non desired contribution is amplified by the same mechanism as the signal and gives rise to the amplified spontaneous emission (ASE) noise. The optical power emitted by spontaneous emission in the frequency band $\Delta\nu$ is given by [24]

$$P = 2h\nu\,\Delta\nu\,n_{sp}\,(G-1) \tag{42}$$

where $G$ is the EDFA gain, $h$ the Plank's constant, $\nu$ the optical frequency and $n_{sp}$ the spontaneous emission factor which characterizes the excess noise with respect to the quantum limit. The ASE impact is measured by the optical signal to noise ratio (OSNR) which is defined as the ratio between the signal and the spontaneous emission noise power in a specified frequency band, usually 0.1 nm. Thanks to many advantages among which we can cite

- the low insertion loss,
- the high gain,
- the large amplification bandwidth (more than 30 nm),
- the total independence of the amplification regarding the signal polarization state,
- the relatively low noise level,
- the transmission line transparency to the bit rate since the complex and expensive receivers-regenerators using fast electronic circuits are suppressed,

this type of amplifier has truly revolutionize optical communications. With the use of EDFAs, the transmission lines do not necessitate the conventional receivers which regenerate the signal but whose number must be equal to the number of WDM channels used. Besides the demultiplexing/multiplexing performed just before and after each repeater, the disadvantages in terms of cost and power dissipation made the implementation of WDM impossible for undersea communication systems. Nevertheless, the EDFA gain non-uniformity on the whole possible amplification band (Figure 12) makes its control critical. The imbalance introduced on the channel power levels impairs the OSNR, thus the total possible reach of WDM systems. This is why the design of EDFA includes gain equalization. This can be done by optimized and dynamical filters (GEF, *Gain Equalizing Filter*).

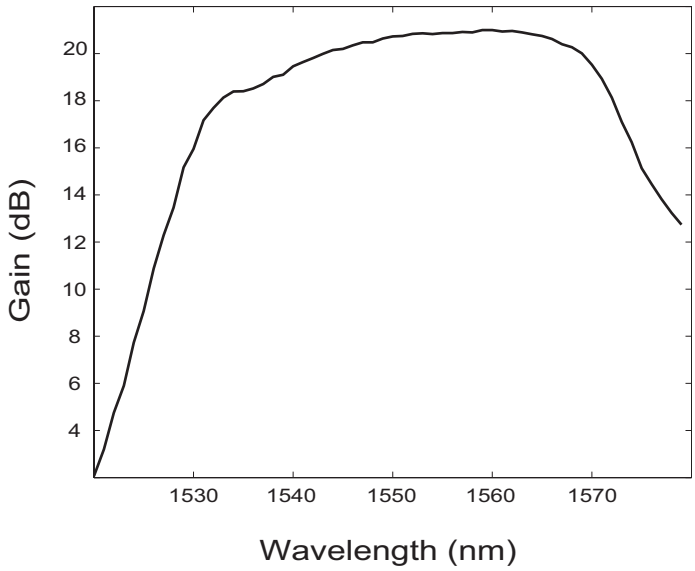


**Figure 12. Experimental gain curves of an erbium-doped fiber amplifier (Kheopsys) used in chapter 4.**

#### *2.2.1.2 Raman amplification*

The previous amplification technique requires the doping of a fiber, used as the gain medium. Another solution exists in which the gain is obtained in the fiber where the signal propagates. The stimulated Raman scattering (SRS), presented paragraph 2.1.3.6, is the physical phenomenon at the origin of the amplification. The optical signal is injected in the fiber

with the pump, typically at a 100 nm shorter wavelength and gradually amplified along the fiber (Figure 13).

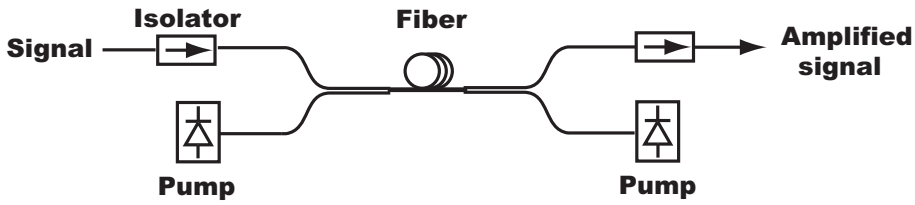


**Figure 13. Scheme of a Raman amplifier.**

Although this effect has been known and studied for more than 30 years, the high pump power needed to get a 10-15 dB gain (on the order of few hundreds of mW) and the interaction length demanded delayed its practical use. Another reason was the arrival of EDFAs. Nevertheless, Raman amplification is successfully used with ultra-long haul undersea systems [25]. More powerful laser diodes are now available and the ability to amplify the signal in low noise conditions is extremely important for those systems. Distributed along the fiber, the Raman gain considerably improves the OSNR since at the end of a cell, the attenuation of the optical power is less important (Figure 14). This improvement is typically represented by an equivalent noise factor $NF_{eq}$ which would be the same as the amplifier located at the end of the cell, producing the same gain and the same contribution of spontaneous emission. So Raman amplifiers have a lower equivalent noise factor than EDFAs ($NF_{eq} \sim -1.5$ dB for a 15 dB gain) which are in principle limited to values higher than 3 dB. The margin gained on the OSNR could go up to 6 dB and could potentially be used to increase the total transmission length.

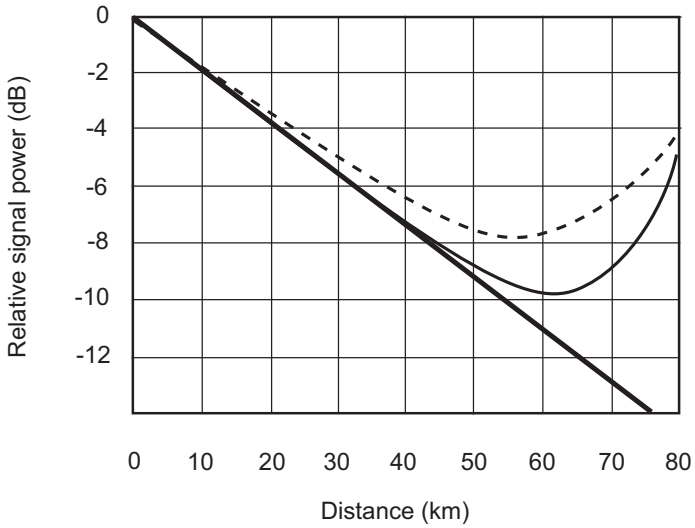


**Figure 14. Attenuation of an optical signal $\lambda_s$ with Raman amplification (contra-propagative pump, $\lambda_s$ = 1531.1 nm (solid line), $\lambda_s$ = 1608.3 nm (dashed line)). The natural attenuation of the fiber is represented in bold.**

#### *2.2.1.3 Hybrid amplification*

For gain higher than 20 dB, the equivalent noise factor improvement of Raman amplification is limited by the double Rayleigh retro-scattering. It imposes a limit on the usable Raman gain which is no more sufficient to compensate for the fiber losses. This is the case for terrestrial transmissions when the losses due to the dispersion compensation and the add-drop multiplexing are taken into account. A low gain EDFA is usually added to the Raman amplifier to overcome these limitations. The noise factor resulting from this hybrid amplification is entirely determined by the Raman amplifier placed first. Optical amplification is not only limited to the techniques previously presented. Parametric amplification is an important example regarding the interest it provokes. Nevertheless, we made the choice to not go into the details of an exhaustive list which is not relevant to our study and Figure 15 gives an idea of the bands covered by different technologies.

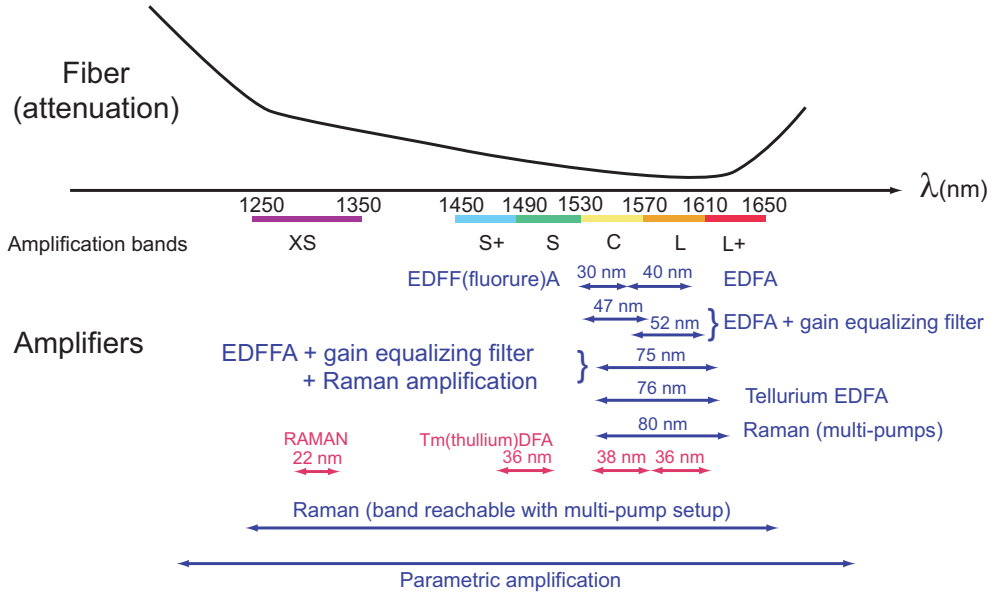


**Figure 15. Amplification bands covered by various amplification technologies (according to [2, 3]).**

### 2.2.2 Dispersion compensation

We have already underlined the limitations coming from the pulse broadening inherent to the dispersive characteristic of the medium and proportional to the bit rate-distance product $B \times L$. This effect is certainly minimized around the zero dispersion wavelength ($\lambda_{ZD} \sim 1.31\ \mu$m) but, historically, the minimum for the fiber attenuation has fixed the use of the 1.55 $\mu$m window. The maximum distance $L$ that can be reached is limited by [15]

$$L < [16|\beta_2|B^2]^{-1}. \tag{43}$$

Table 2 shows the dramatic impact of the dispersion on high bit rate transmissions if nothing

**Table 2. Maximum transmission distance as a function of the line bit rate. The chromatic dispersion is D=16 ps/(nm.km).**

| B (Gb/s) | L (km) |
|---|---|
| 2.5 | 500 |
| 10 | 30 |
| 40 | 2 |

is done to counteract the impairments. If we only take the dispersion effect in account in the NLSE, we have

$$\frac{\partial A}{\partial z} + \frac{i\beta_2}{2}\frac{\partial^2 A}{\partial t^2} = 0\,. \tag{44}$$

In the Fourier domain, the solution is

$$A(L,t) = \frac{1}{2\pi}\int_{-\infty}^{+\infty} \tilde{A}(0,\omega)\,.\,e^{\frac{i}{2}\beta_2 L\omega^2 - i\omega t}\,d\omega \tag{45}$$

where $\tilde{A}(0,\omega)$ is the Fourier transform of $A(0,T)$ and $L$ the length on which $\beta_2$ is uniform. During the propagation, each spectral component of the signal experiences the following phase-shift $\phi_s = \beta_2 L\frac{\omega^2}{2}$. The idea is to introduce some DCF spans in or at the end of the line to compensate for this phase shift $\phi_s$

$$\beta_2^{(1)}L_1 + \beta_2^{(2)}L_2 = 0 \tag{46}$$

where $L_1 + L_2 = L$ and $\beta_2^i$ is the $i^{\text{th}}$ span parameter. With this condition, we can easily check that $A(L,t) = A(0,t)$, which is equivalent to say that the shape of the initial pulse is reestablished. This compensation allows to operate globally around the average zero-dispersion for the whole line but keep a relatively high local dispersion, which reduces the timing jitter at the receiver [26] (Gordon-Haus jitter [27]) caused by the nonlinear interaction between the signal and the ASE noise from the optical amplifiers. Moreover, a high local dispersion prevents the FWM from reaching a high efficiency [28, 29], which is very interesting for WDM systems. Actual systems simultaneously include both dispersion (DM) and losses managements [30] using dispersion maps (Figure 16).

Nevertheless, chromatic dispersion cannot be exactly compensated for all the channels because of the wavelength dependence of $\beta_2$. The central channel is the only one to exhibit a zero average dispersion as represented on the dispersion map. The total accumulated dispersion can exceed 1000 ps/nm for the extreme channels of a ultra-long haul (ULH) WDM system. That is why pre and post-compensation techniques are used at the transmitter/receiver and DCF is added according to the need of each channel. The performance

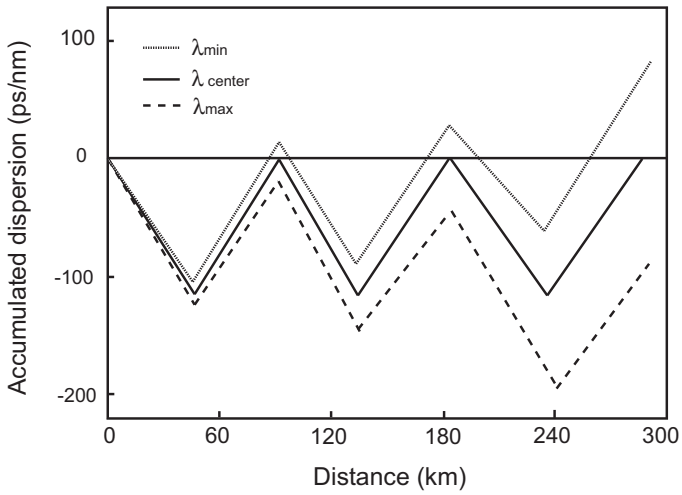


**Figure 16. Dispersion management for the smallest, the highest and the central wavelengths of a WDM system.**

optimization as a function of the compensation parameters is represented on Figure 17. The superposition of all possible trajectories for the signal during one bit period defines the eye diagram. The eye opening is characterized by the height $P_0$ of the greatest rectangle inscribed in it and is a fairly good indicator of the distortion experienced by the signal. The eye opening penalty (EOP) expressed in dB is given by

$$EOP = -10\log\left(\frac{P_0}{2\,P_{moy}}\right), \tag{47}$$

where $P_{moy}$ is the signal average power.

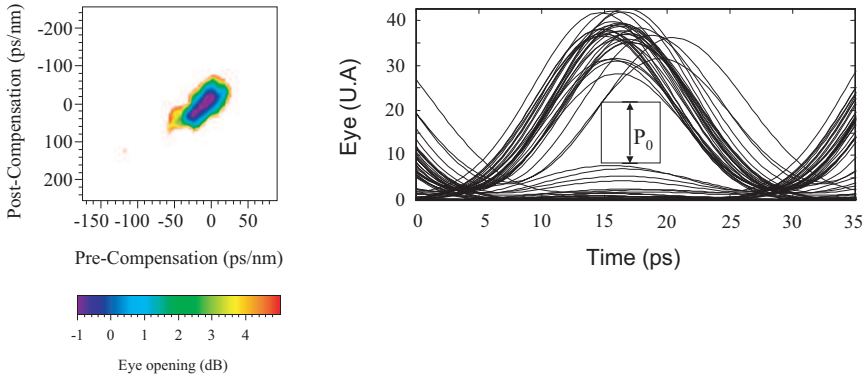


**Figure 17. Pre/post compensation influence on the eye opening of a RZ signal (50%, 12 dBm) after propagation ($8 \times 80$ km, D=2 ps/(nm-km)). The residual dispersion per span is 16 ps/nm [1].**

### 2.2.3 Different types of transmission line

All the techniques previously presented allowed the design of various systems in response to well defined problems. There is therefore no unique solution valid for all of them but general trends emerge and their use is always particular to a given application. This is what is presented in this paragraph which is arbitrarily divided in terrestrial and undersea systems. The performance of an optical communication system can be estimated with the Q factor which represents the signal to noise ration (SNR) at the input of the receiver decision circuits. Figure 18 shows the relation between the eye diagram –RZ eye diagram in this case– and the Q factor defined by

$$Q = \frac{|\mu_1 - \mu_0|}{\sigma_1 + \sigma_0} \tag{48}$$

where $\mu_0$ et $\mu_1$ are the means of logical '0' and '1' and $\sigma_i$ their corresponding standard deviation.

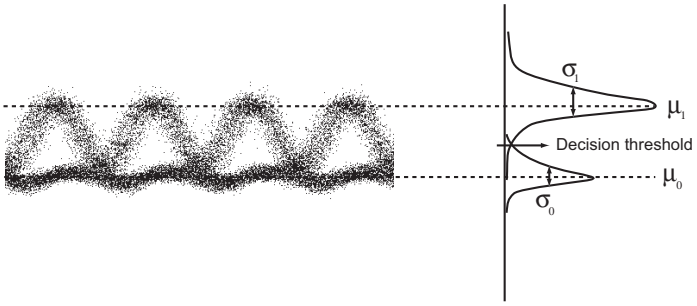


**Figure 18. Q factor is defined from the eye diagram (example of an RZ signal).**

The knowledge of the ideal Q factor is very useful as a starting point to estimate the design margins. Marcuse expressed it as a function of the OSNR [31] estimated with (49). Zyskind shows in [32] that the OSNR of a system consisting of $N_{amp}$ amplifiers with $P_{out}$ output power per channel (so $N_{amp}$ fiber spans having each $L_{Loss}$ dB loss) is given by

$$OSNR(dB) = 58 + P_{out} - L_{Loss} - NF - 10\log(N_{amp}) \tag{49}$$

where $NF$ is the noise figure of the amplifiers. For high gains, one can show that $NF \sim 2\,n_{sp}$ [24]. The formalism introduced by Marcuse can be modified to take several factors

into account such as the pulse shape or the finite transmitter extinction ratio $r$. For non-return to zero (NRZ) data, the Q factor is given by

$$Q = \frac{\gamma\, SNR \sqrt{\frac{B_0}{B_E}}}{\sqrt{1 + 2\gamma\, SNR\,(1 + \frac{r}{1-r})} + \sqrt{1 + 2\gamma\, SNR\, \frac{r}{1-r}}}\,, \tag{50}$$

where

$$\gamma = \frac{2(1-r)}{1+r}, \tag{51}$$

with $B_E$ and $B_0$ the electrical and optical bandwidth of the receiver.

#### *2.2.3.1 ULH Terrestrial transmissions*

From the first tests performed in 1977, optical communication systems have constantly evolved. The transmission window has progressively moved from 0.85 $\mu$m to 1.30 $\mu$m, zone where the chromatic dispersion of standard fibers is almost zero, then to 1.55 $\mu$m where their attenuation is minimum. This third generation has been commercialized since 1991. From then, technical improvements (DFB sources (*Distributed FeedBack DFB*) with narrow linewidth, the development of fibers with inversed dispersion, the use of dispersion management, the improvement of the optical amplification technology, the compensation of PMD, and the implementation of error correcting codes) pushed the limits further in terms of bit rate, distance between amplifiers and/or total distance. Figure 19 represents the structure of a modern terrestrial line.

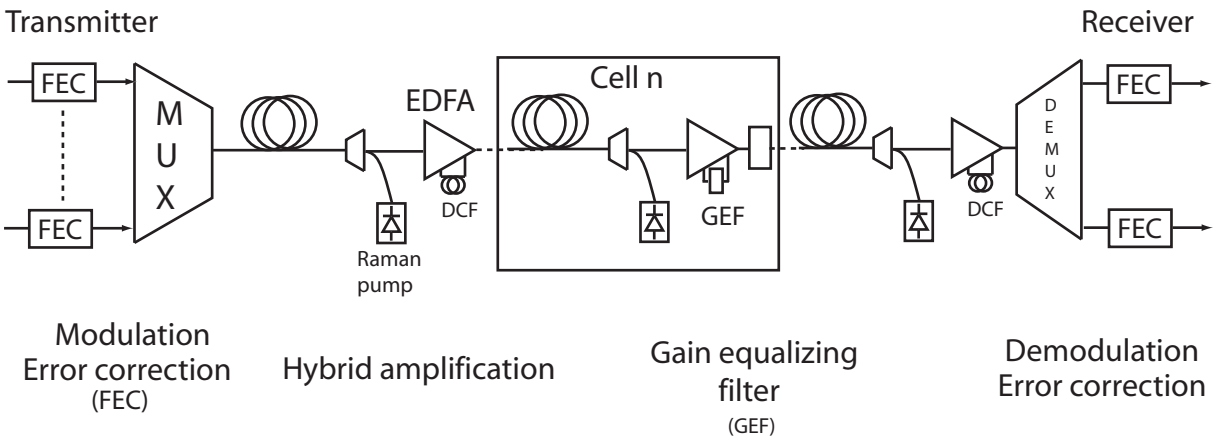


**Figure 19. ULH terrestrial transmission lines.**

*2.2.3.2 Undersea transmissions*

Undersea transmissions are used for intercontinental communications. Their design is a great technical challenge to reach a 25 year lifetime with a great reliability (at most 3 breakdowns in operation). For example, Table 4 gives the required margins for a 6000 km transatlantic line consisting of 32 channels at 10 Gb/s. The key parameters are the amplifier spacing, the total input power in the fiber and the dispersion management of the line (Table 3).

**Table 3. Parameters used in the design of a transatlantic line.**

| | |
|---|---|
| Total distance | 6000 km |
| Amplifiers spacing | 50 km |
| Number of amplifiers | 60 |
| Amplifiers gain | 10 dB |
| Total input power | 11 dBm |
| Amplifiers noise factor | 4.5 dB |
| Channel spacing | 75 GHz |
| Amplifiers bandwidth | 19 nm |
| Dispersion management cell | 500 km |
| Dispersion slope | 0.075 ps/km-nm$^2$ |
| Bit rate (23% FEC overhead) | 12.3 Gb/s |

To take all the impairments experienced by the line along its life into account, different margins are computed from

- the ideal value of the Q factor computed with the transmission parameters thanks to Equations (49) and (50),
- the minimum value required by the error correction (FEC, *Forward Error Correction*) to get a $10^{-9}$ bit error rate.

Each improvement is built on to relax the constraints on the system at constant performance. The use of a modulation format resistant to nonlinearities allows for example a higher amplifier spacing or a lower channel spacing which reduces the costs or increases the capacity of the line.

**Table 4. Example of a margin budget allocated for a transatlantic line.**

| Parameter | value (dB) |
|---|---|
| Ideal average Q factor | 17.8 |
| Estimated margins to face the different constraints: | |
| Propagation losses [1] | 4.3 |
| Variations in the fabrication [2] | 2 |
| Time fluctuations of Q | 1 |
| Aging | 1 |
| Q end of life [3] | 9.5 |
| Required Q (imposed by the FEC threshold) | 8.5 |
| End of life margin[4] | 1 |

[1] Fibers nonlinearities, additional noise caused by the optical reflections and the imperfect dispersion management ...

[2] It includes the fact that real components are made from imperfect industrial processes

[3] Average Q value after subtracting the estimated margins from the ideal average Q value

[4] End of life Q value after subtracting the required Q value

## 2.3 Emission, detection and data processing

As the need for higher capacity systems is urging, the bit rate and the number of channels still increase underlining the deleterious effects of chromatic dispersion and both intra and inter-channel nonlinearities. In this context, the use of efficient modulation formats, more robust to these limitations and allowing a higher channel spacing, and correcting codes becomes decisive to find an optimal setup.

### 2.3.1 Modulation formats

Besides the technical simplicity desired in the transmitter design, another important parameter determines the optimal choice for the modulation format used in a given line: the spectral efficiency $\eta$.

$$\eta = \frac{B}{\nu_c} \text{ (Bit/s/Hz)} \tag{52}$$

where B is the bit rate and $\nu_c$ the channel spacing (Table 5). According to the modulation format, the optical spectra have different shape and bandwidth. Moreover, the symbol interference introduced by optical or electrical filtering is varying from one format to another. The ability to reach a high spectral efficiency by multiplexing many channels is therefore dependent on the modulation format used.

**Table 5. Spectral efficiency for various systems.**

| B (Gb/s) | Channel spacing (GHz) | Spectral efficiency $\eta$ (%) |
|---|---|---|
| 2.5 | 100/50/25 | 2.5/5/10 |
| 10 | 200/100/50 | 5/10/20 |
| 40 | 200/100 | 20/40 |

#### *2.3.1.1 NRZ, RZ*

The basic modulation formats in use in commercial systems (NRZ and RZ) rely on an intensity modulation coupled to a direct detection (IMDD, *Intensity Modulated Direct Detection*). They are defined by their pulse shape and their duty cycle

$$d = \frac{T_I}{T_B} \tag{53}$$

where $T_I$ is the pulse width and $T_B$ the bit slot.

NRZ is easy to generate and its spectral width allows a $2.5 \times B$ channel spacing. RZ is more difficult to generate because it requires an additional modulator to perform the pulse carving. Its spectrum is larger than NRZ (Figure 20) and only allows a 3 to $4 \times B$ channel spacing depending on the duty cycle. Nevertheless, RZ shows outstanding resistance to nonlinear effects which makes it a good candidate for submarine systems. Each symbol '1' is virtually independent of its neighbors and thus experiences the same nonlinearity. On the contrary a sequence of '1' in NRZ creates a continuous power which is unstable at its edges. Long distances have been reached for a single channel in lab experiments. However,

- its larger spectral width does not allow a dense multiplexing: 10 Gb/s with 25 GHz channel spacing leads to better performances with NRZ [33].
- It also suffers from a low dispersion tolerance.

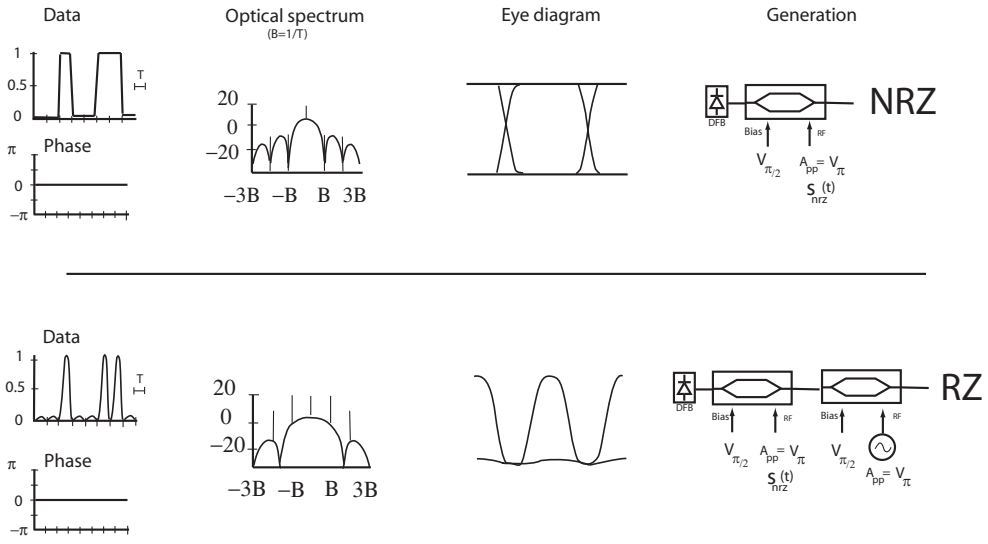


**Figure 20. NRZ and RZ modulation formats.**

**Remark:** For each format cited, we give a scheme leading to its experimental implementation. The Mach-Zehnder modulator (MZM) output is determined by the bias tension (Bias) and by the nature and amplitude of the driving RF signal. For NRZ, as the signal $s_{NRZ}(t)$ has a $V_\pi$ amplitude ($A_{pp}$) and the bias is $V_{\frac{\pi}{2}}$, the operating point is at the center of the MZM Power-bias characteristic and the optical output is either a '0' or a '1'.

### *2.3.1.2 Modified RZ formats*

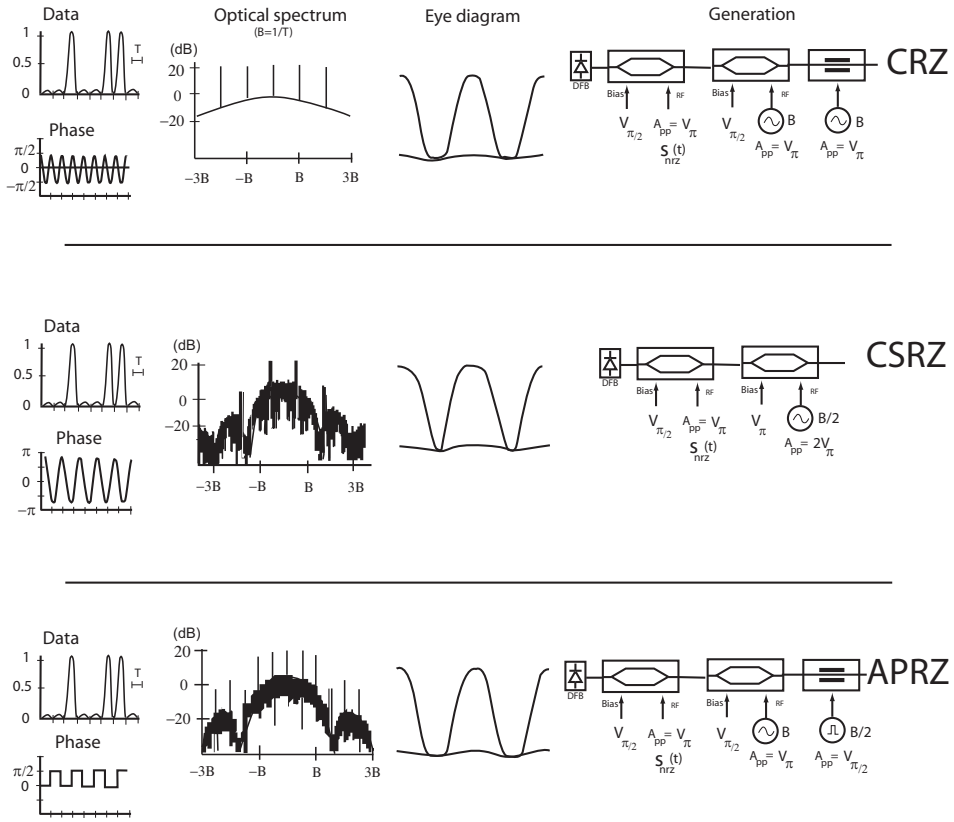


**Figure 21. CRZ, CSRZ and APRZ modulation format.**

Several formats have been proposed as an alternative for the conventional RZ (Figure 21).

- CRZ, *Chirped RZ*: one of the most used, it consists of an additional phase modulation driven by a *B* GHz clock [34]. CRZ spectrum is even wider than the RZ one, which limits its capacity. Nevertheless, its higher resistance to nonlinear effects guaranteed

its use in 10 Gb/s submarine systems [35].

- CS-RZ, *Carrier Suppressed RZ*: it is initially used in 40 Gb/s terrestrial systems [36]. The data is encoded on the pulse intensity whereas the phase systematically alternates between 0 and $\pi$. The average electric field is therefore null and the spectrum does not have any carrier. The detection is performed with a usual photo-detector. With a reduced spectrum compared to RZ and comparable to NRZ, CS-RZ shows a better tolerance to nonlinear effects and chromatic dispersion [37]. 40 Gb/s transmissions with 100 GHz spacing are possible [38] as well as transmitting over transpacific distances [39]. However, CS-RZ is not very effective against intra-channel effects. A systematic phase-shift of $\pi/2$ (no longer $\pi$) is applied to fight them. It gives birth to $\pi/2$-APRZ, *Alternate Phase RZ* [40].

#### *2.3.1.3 High spectral efficiency*

In order to achieve a 50 GHz channel spacing at 40 Gb/s (or 12.5 GHz at 10 Gb/s), the focus shifted to formats with reduced spectral occupation:

- **Duobinary modulation and phase shaped binary transmission (PSBT)**

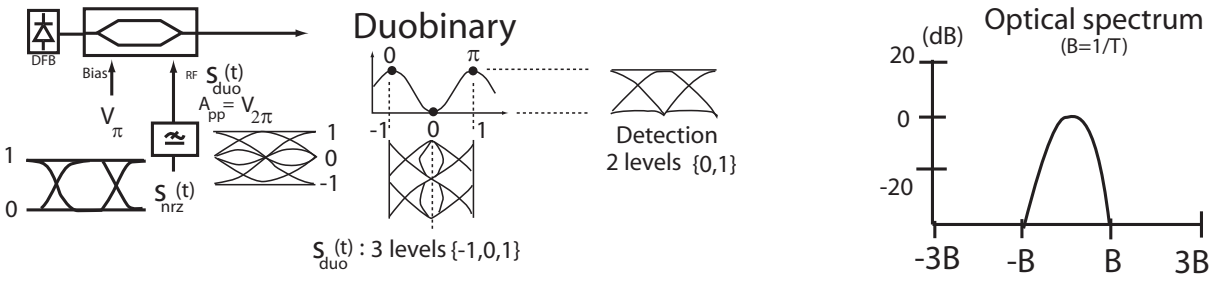


**Figure 22. Duobinary modulation scheme.**

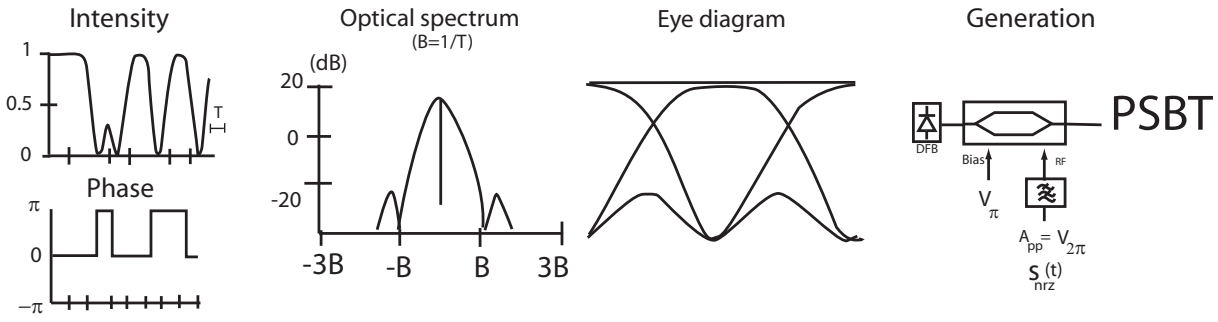


**Figure 23. PSBT modulation format.**

Those formats rely on a 3-level modulation – generally 0, +1 and −1 – so that the quadratic detection only sees 0 and 1 (Figures 22 and 23). They divide by a factor 2 the occupied bandwidth but require data precoding. The 4 dB sensitivity degradation can be compensated by an additional NRZ modulation [41, 42]. Dense transmissions (40 Gb/s, 50 GHz channel spacing) have been performed [43] and show a good tolerance to the chromatic dispersion.

- **Vestigial side band modulation (VSB)**: in RZ or NRZ spectra, the information contained by both sides of the optical carrier is redundant. In VSB modulation, only half of the spectrum is conserved after optical filtering or Hilbert transform in the RF domain (Figure 24). NRZ-VSB reaches a 0.8 bit/s/Hz spectral efficiency [44] whereas its RZ counterpart reaches 0.53 bit/s/Hz [45]. In all cases, the characteristics of the optical filter is of vital importance for the quality of the generated signal.

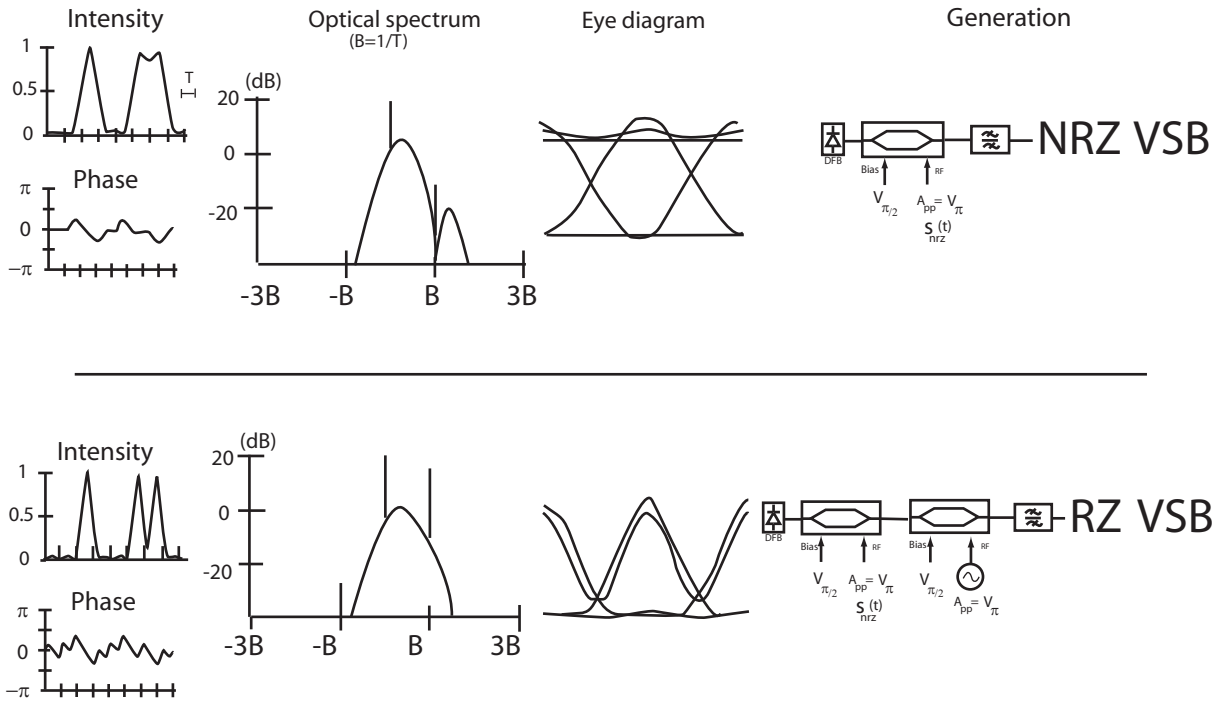


**Figure 24. NRZ-VSB, RZ-VSB modulation formats.**

- **Phase modulation** (PSK, *Phase Shift Keying*): Pure phase modulation, for which the intensity remains constant, has been proposed to increase the nonlinearity tolerance. Since the Kerr effect is depending on the signal intensity, the nonlinear phase-shifts experienced by ’0’ and ’1’ are identical. Differential phase shift keying (DPSK) is performed either with a phase modulator or a MZM properly biased (Figure 25) so that data is encoded on the phase difference of two successive bits. A precoding step is required to avoid error propagation. As quadratic detection is not sensitive to phase, the demodulation is done by an unbalanced Mach-Zehnder interferometer (MZDI, *Mach-Zehnder delay interferometer*) (Figure 26). The delay introduced corresponds to one bit period T and the MZDI performs an interference between two successive bits [46].

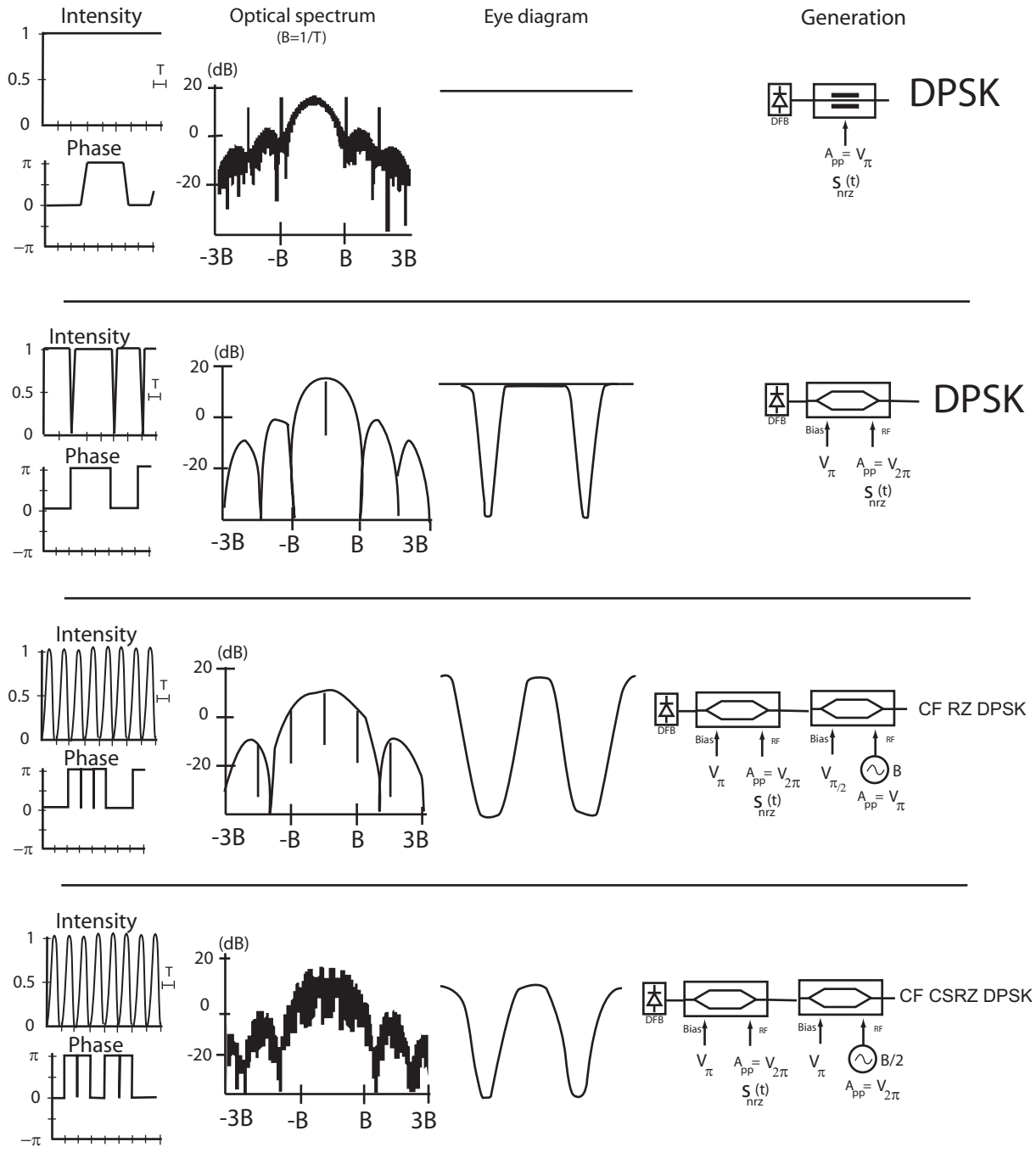


**Figure 25. DPSK, CF-RZ DPSK, CF-CSRZ DPSK modulation formats.**

The natural evolution of NRZ-DPSK towards RZ formats such as RZ-DPSK or CSRZ-DPSK allows the demonstration of impressive performances in terms of capacity and transmission distance [47–49]. Compared to RZ, they show a good resistance to nonlinear effects [50], to optical filtering and a 3 dB gain in sensitivity using a balanced detection. However, they are fundamentally limited by the phase noise accumulated at the various optical amplification stages.

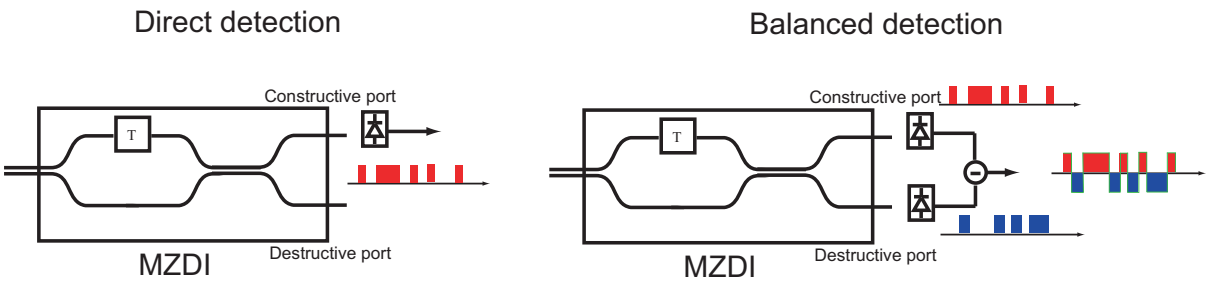


**Figure 26. Demodulation and detection of DPSK formats.**

- **Multi-levels**: we can regroup the bits and code them on several levels [51]. For the same transmitted information, the spectral occupation is divided by $log_2(M)$ if $M$ levels are used but the sensitivity degradation is high: estimated around 3.3 dB for $M = 4$ and experimentally measured around 8 dB.

  The receiver complexity is increased since $M$ intensity levels have to be discriminated [52]. Recently, QPSK modulation (*Quadrature Phase Shift Keying*) showed good results [53–56]. After precoding, the even and odd sequence I and Q extracted from the initial bitstream are encoded on 4 phase levels (Figure 27). The demodulation performs the conversion in two intensity-modulated signals — one discriminating 0 and $\pi$ phase shift, the other between $-\pi/2$ and $\pi/2$ — detected by standard photodetectors.

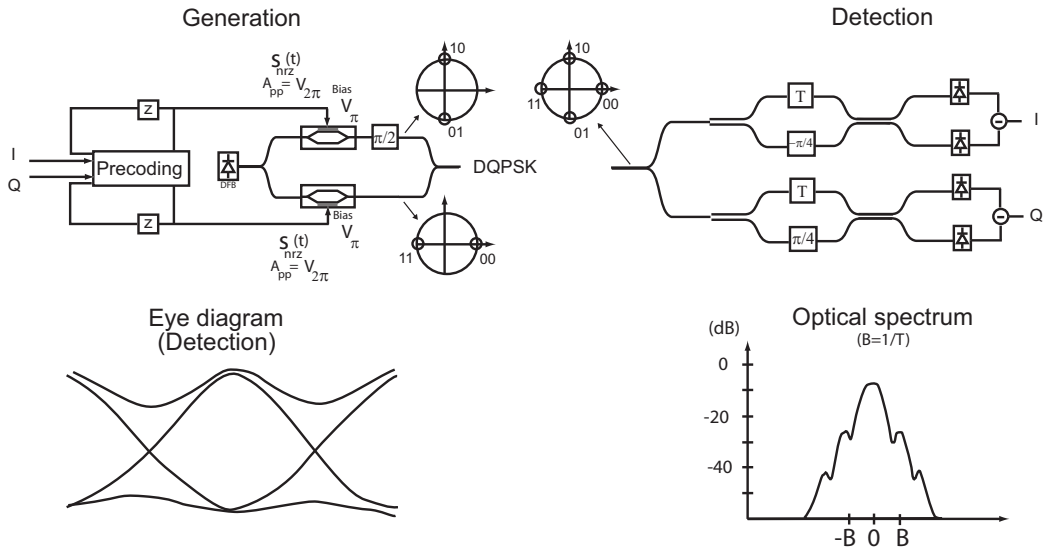


**Figure 27. DQPSK modulation scheme.**

### 2.3.2 Error correction

The FEC implementation gives a relatively large margin to increase the total transmission distance, the amplifier spacing and/or the total capacity of the system to decrease the costs [57]. Almost all modern communication systems have integrated the RS(255,239) Reed-Solomon code [58]. Since its first use in submarine systems at the beginning of the 90's [59] and its development [60, 61], even more powerful codes have been implemented:

- concatenated RS codes: RS(255,239)+RS(255,239), RS(255,239)+RS(255,223) [62] or RS(239,223)+RS(255,239) [63],
- turbo-codes, based on the concatenation of several block codes associated to an iterative decoding [64, 65].

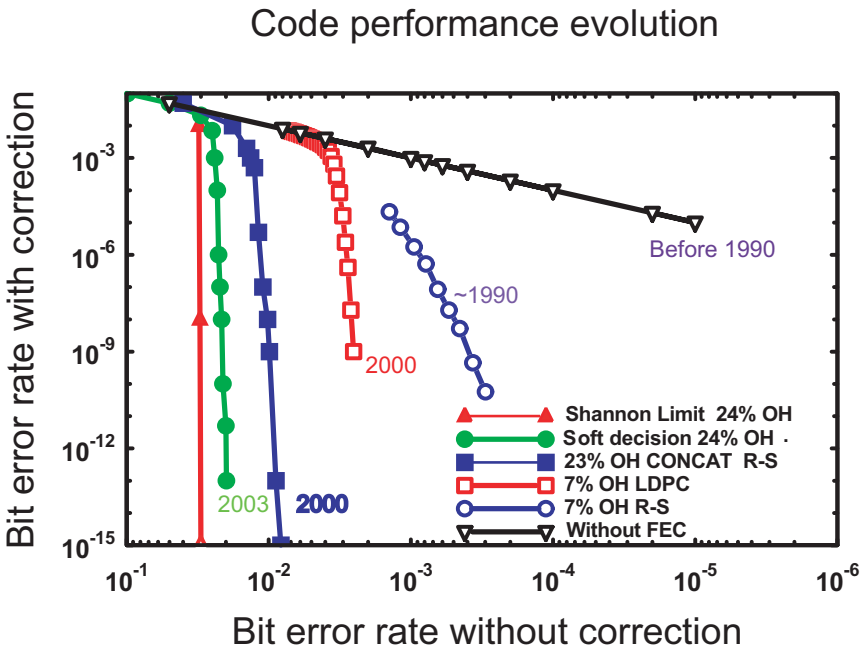


**Figure 28. Usage of FEC (according to H. Kogelnik, ECOC 2004). The number in front OH (OverHead) characterizes the redundancy level used by the code.**

### 2.3.3 Performances

This paragraph is absolutely not an exhaustive list of all the experiments led in the field of optical communications. Here, the goal is to give the reader an overview of the performances presented by companies during the last OFC and ECOC conferences. Most of the WDM experiments have a 40 Gb/s bit rate per channel. Those systems reached capacities superior to 10 Tb/s even if the record in terms of bit rate-distance product is held by [66,67]. They use 10 Gb/s bit rate per channel and respectively reach 28 and 41 Pb/s km. More than just pure performance, a recent trend focuses on the system optimization to make it more simple and cost effective (Table 6).

- If RZ-DPSK seems to be the good candidate for future systems, no field experiment has been conducted before [68] in order to confirm its 3 dB advantage over conventional RZ-OOK.

- On a given transmission line, the search for the most efficient modulation formats led a Lucent team [69] to propose polarization-alternating RZ-DPSK to improve 42.7 Gb/s WDM systems.

- A first team of Alcatel [70] showed that under certain conditions DPSK can give as good results as RZ-DPSK. The implementation is less complex and therefore less expensive.

- A second team [71] shows that DPSK formats can be used in 10 and 40 Gb/s deployed submarine lines.

- Increasing the capacity of existing transmission lines is a possible cost effective method. In this context, KDD proposes an experiment based on CSRZ-DQPSK [72]. It holds the record in term of spectral efficiency without polarization multiplexing with 1.14 bit/s/Hz.

We have so far studied various developments of optical communication systems and we will focus on what is considered to be the main limitation of coherent format: the phase jitter.

**Table 6. Performances presented at OFC and ECOC 2004.**

| Company | Capacity (Tbit/s) | Channel spacing (GHz) | Spectral efficiency (Bit/s/Hz) | Distance (km) |
|---|---|---|---|---|
| Tyco [68] | 0.96 (96 x 10 Gbit/s) | 33 | 0.30 | 13100 |
| Lucent JGKB Photonics [69] | 0.24 | 100 | 0.4 | 2000 |
| Alcatel [70] | 6 149x 42.7 Gbit/s | 50 | 0.8 | 6120 |
| Alcatel [71] | 1.68 (42x42.7 Gbit/s) | | | 4820 |
| KDD [72] | 4 (50x85.4 Gbit/s) | 70 | 1.14 | 300 (4x75) |
| KDD [73] | 3.2 (10x320 Gbit/s) | 400 | 0.8 | 40 |
| KDD/Mitsubishi [57] | 0.4 (32x12.4 Gbit/s) | 37.5 | | 9000 (60x150) |

# CHAPTER 3

# OPTICAL PHASE JITTER

Variations of the differential phase-shift-keyed (DPSK) modulation format have recently allowed for the demonstration of impressive transmission capacities in the context of long-haul fiber-optic communication systems [74] and represent a promising technique to further increase optical communication system performance [75]. In these formats, data is encoded in an optical phase difference between adjacent bits. It has been shown that this type of modulation offers several advantages, namely, the reduction of the penalty resulting from nonlinear effects, a good tolerance to narrowband filtering, a high spectral efficiency in the quadrature DPSK implementation, and the possibility of using balanced detection to enhance the sensitivity of the receiver. In these systems, the error-free transmission distance is limited by random fluctuations of the phase. Physically, phase jitter arises from amplified spontaneous emission (ASE) noise that is added to the signal at each amplification stage along the link. In this section, we introduce the background of the proposed research. We therefore give a brief overview of the physical origin of phase jitter before reviewing some classical techniques used to control it.

## 3.1 Origin

### 3.1.1 Linear contribution

The optical field at the output of an erbium doped fiber amplifier (EDFA) without spontaneous emission is given by

$$E_s^{out} = \sqrt{G}\, E_s^{in}\, e^{-ik_0 nL}\,, \tag{54}$$

where $n$ is the erbium doped fiber index, $L$ and $G$ are, respectively, the length and the gain of the amplifier and $k_0$ the wavevector in vacuum. By taking the spontaneous emission phenomenon into account, the noise term

$$E_{ASE} = E_N(t)\, e^{i\phi(t)} \tag{55}$$

adds to $E_s^{out}$, amplitude $E_N(t)$ and phase $\phi(t)$ being random. In the following study, the in-phase and quadrature components of the noise are considered independent Gaussian random variables. The different fields are represented in the complex plane of Figure 29. The angle $\delta\phi(t)$ between the amplifier input and output optical fields $E_s^{out}$ and $E_T$ defines the linear part of the phase jitter. The linear term recalls the fact that the contribution of ASE to the total phase jitter is direct. The linear fluctuations around the average field are described by a two-dimensional Gaussian distribution.

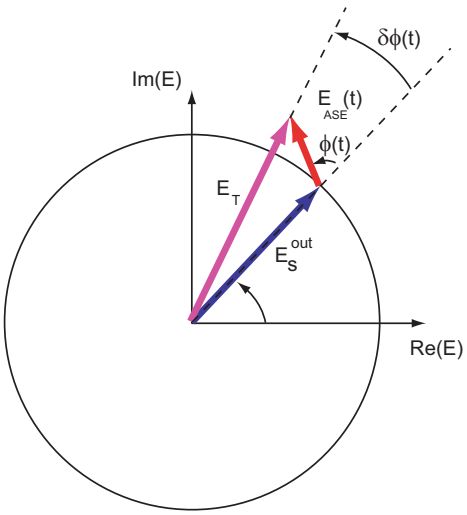


**Figure 29. Linear phase jitter.**

### 3.1.2 Nonlinear contribution

During the propagation in the fiber, a nonlinear phase $\phi_{NL}$ is accumulated through SPM

$$\phi_{NL}(L,t) = \int_0^L \gamma(z)\,|\,u(z,t)\,|^2\,dz\,. \tag{56}$$

It clearly appears that the power fluctuations resulting from ASE noise will translate into phase jitter via the Kerr effect. This mechanism, also known as the Gordon-Mollenauer effect, not only adds a nonlinear contribution to the total phase (Figure 30), but also induces a correlation between amplitude and phase noise. This correlation is visible when nonlinearity plays an important role in the propagation.

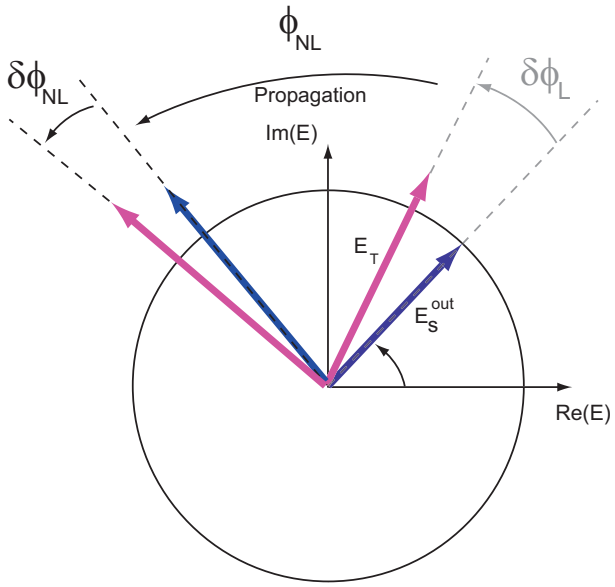


**Figure 30. Nonlinear phase jitter.**

Figure 31 represents the evolution of a soliton optical field in a dispersion-managed link whose parameters are recalled in Table 7. The same initial condition is launched 1024 times in the transmission line to obtain 1024 simulations with different ASE noise to infer the phase variance. Figure 31 shows that in the case where total phase jitter is dominated by its linear component — at the beginning of the propagation — the samples follow a Gaussian statistic; hence the circular form is observed. The nonlinear component progressively dominates and the disk takes the form of a crescent moon whose extent increases with the covered distance. The Gordon-Mollenauer-induced correlation can be seen in the particular shape of the crescent. One can notice that it is not centered. In the case of 2040 and 3000 km propagation, the most powerful pulses are also the ones that experience the greatest phase shifts. This fundamental characteristic of nonlinear phase jitter is used in some techniques to provide its control.

Considering a standard DPSK transmission where the phase takes only two values, and seeing how the crescent spreads, we can understand why phase jitter becomes the main

limiting factor and how it is important to control it as much as we can. The next section reviews experimental techniques performing jitter control/reduction.

**Table 7. Transmission line parameters.**

| | |
|---|---|
| Pulse shape | $sech^2$ |
| FWHM Pulsewidth (ps) | 20 |
| Pulse peak power (mW) | 7.2 |
| Fiber 1 dispersion (ps/nm.km) | 11 |
| Fiber 1 length (km) | 30 |
| Fiber 1 effective area ($\mu m^2$) | 50 |
| Fiber 2 dispersion (ps/nm.km) | -10 |
| Fiber 2 length (km) | 30 |
| Fiber 2 effective area ($\mu m^2$) | 50 |
| Distance between amplifiers (km) | 60 |
| Spontaneous emission factor | 1.5 |

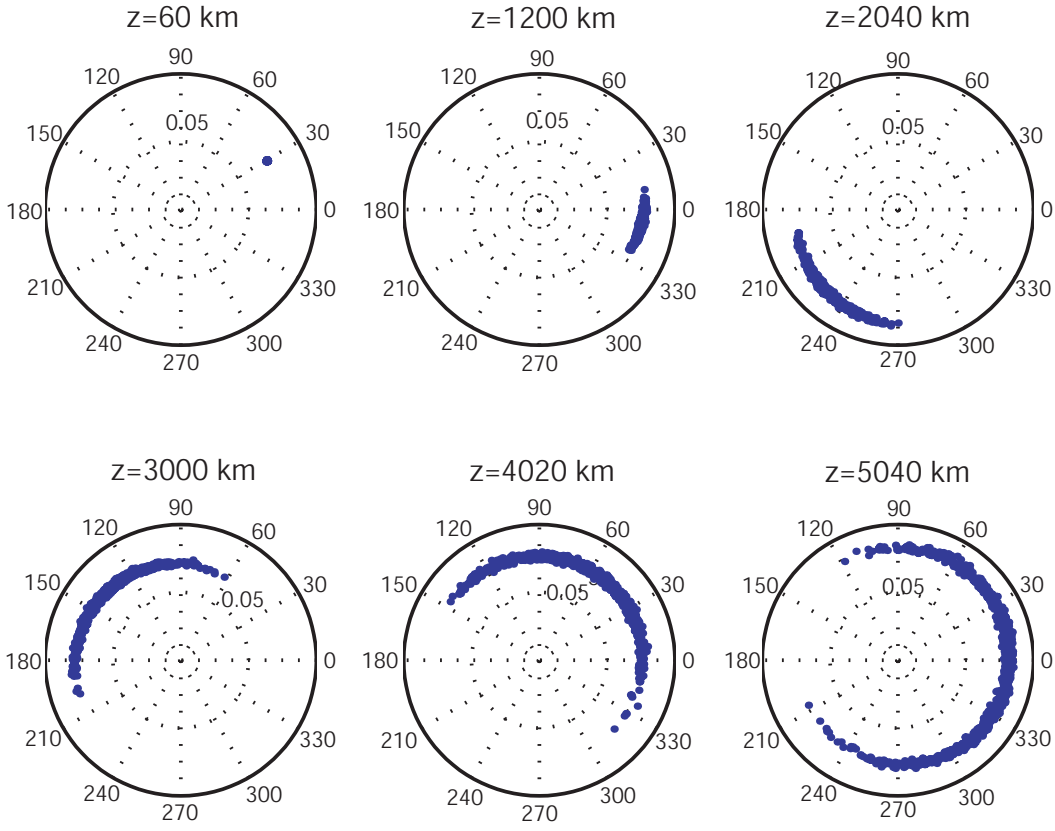


**Figure 31. Phasor diagrams as a function of distance.**

### 3.1.3 Experimental techniques providing phase jitter control

Filtering has been studied in depth in the preliminary research so it is not considered and detailed in the present section.

#### *3.1.3.1 Nonlinear compensation*

A technique based on nonlinear distributed compensation (NPSC, *Nonlinear Phase-Shift Compensation*) has been proposed in [76, 77] to reduce phase fluctuations. The compensation can also be performed at the receiver [4]. The underlying idea behind these techniques is to take advantage of the Gordon-Mollenauer-induced correlation between amplitude and phase noises. As the most powerful pulses experience the greatest phase shifts, applying a negative correction proportional to their power is enough to return them close to their initial states and thus reduce the amplitude of the fluctuations. The former techniques only differ in the component used to perform the correction. The end of this paragraph is devoted to the presentation of two experimental implementations. Their results are expressed in different ways. The phase distribution represented on a complex plane (Figure 32) is obtained by numerical simulations, which show its evolution. On the other hand, the eye diagram gives a direct view of the distortions experienced by the optical signal throughout its propagation.

The first technique performs a compensation based on a periodically poled LiNbO3 waveguide [4]. It has been previously shown [78] that the cascading of second-order nonlinear effects that occur in such a device is equivalent to a nonlinear index $n_2$ whose sign and amplitude can be controlled by varying the phase-matching conditions between the fundamental and the second harmonic generated in the waveguide. The phase-matching condition is easily modified by controlling the temperature of the device. This is also used to adapt the nonlinear compensation to any particular transmission lines. Each pulse is subjected to a negative phase shift that is proportional to its power. Negative phase shifts in excess of 1 rad can be produced with realistic pump powers. The phasor diagrams in Figure 32 show the efficiency of this method with a 5.2 dB reduction in total phase jitter

after a 6000 km propagation. The second technique [5, 79] uses a phase modulator (Figure 33). The amplitude of the modulation is proportional to the intensity of the detected pulse and its sign is opposite the nonlinear phase $\phi_{NL}$ accumulated via SPM. The eye diagrams shown in Figure 34 are obtained with different experimental conditions in order to clearly see the SPM impairments. Cases (a) and (b) differ in the ASE level, which is intentionally added or not at the transmitter side to create (or not) an important phase jitter.

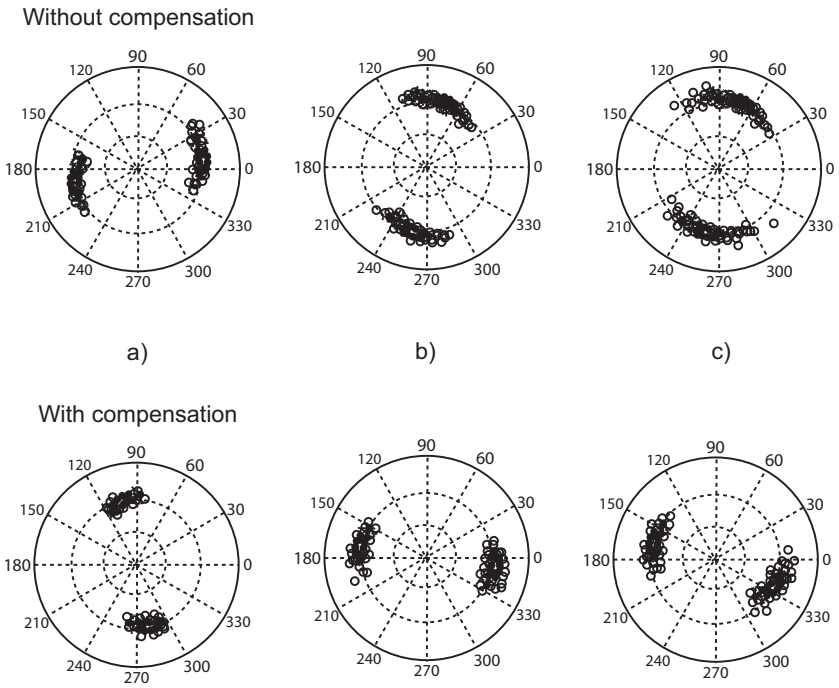


**Figure 32. Experimental results involving NPSC obtained by [4] after a 6000 km transmission with and without NPSC, (a) single channel (b) and (c) DMS-DPSK WDM with 100 and 50 GHz channel spacing.**

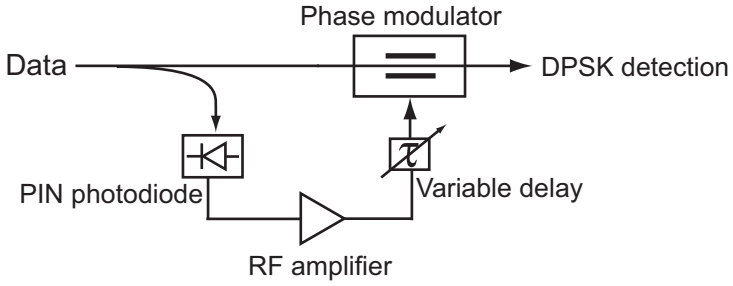


**Figure 33. Nonlinear phase jitter compensation by data phase modulation.**

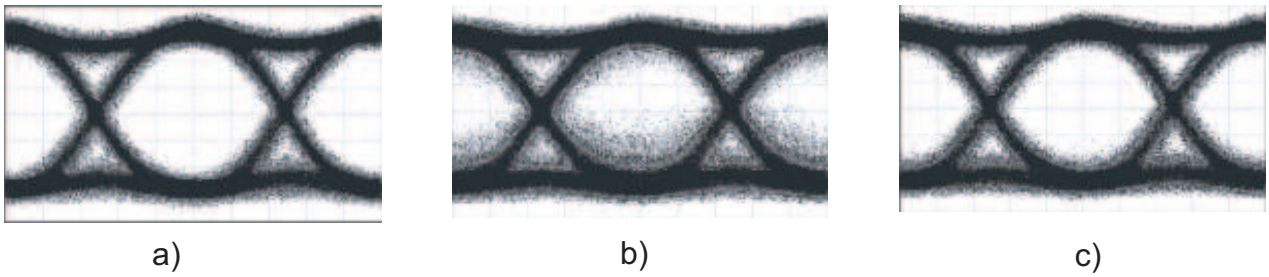


**Figure 34. Eye diagrams obtained in different cases: a) without nonlinear phase jitter b) with nonlinear phase jitter c) with nonlinear phase jitter and compensation technique.**

The compensation has a direct impact on the eye opening. Measurements lead to an increased OSNR margin of 2.5 dB and a 3 dB improvement for the Q factor over the measured OSNR range.

*3.1.3.2 Optical phase conjugation*

Optical phase conjugation (OPC) has been demonstrated as an efficient technique to compensate for

- linear effects such as chromatic dispersion [80] or timing jitter [81] in soliton systems. In the last case, the small random changes in the average carrier frequency of the soliton are transformed in corresponding group velocity fluctuations that finally cause the jitter in arrival times at the receiver.
- nonlinear effects such as SPM [82] or FWM [83].

An intuitive way to understand how OPC can compensate for chromatic dispersion is to take the complex conjugate of the Nonlinear Schrodinger Equation (NLSE):

$$\frac{\partial A}{\partial z} + \frac{i}{2}\beta_2 \frac{\partial^2 A}{\partial t^2} = 0. \tag{57}$$

We get

$$\frac{\partial A^*}{\partial z} - \frac{i}{2}\beta_2 \frac{\partial^2 A^*}{\partial t^2} = 0. \tag{58}$$

Equation (58) means that the propagation of phase-conjugate field $A^*$ is equivalent to changing the sign of the group velocity dispersion (GVD) parameter $\beta_2$. The consequence

of this observation is important for optical communication systems. If the optical field is phase conjugated in the middle of the link, the dispersion accumulated in the first half part will be fully compensated in the second part. The same argument applied to equation (59) explains the possible compensation for both chromatic dispersion and nonlinearity.

$$\frac{\partial A}{\partial z} + \frac{i}{2}\beta_2 \frac{\partial^2 A}{\partial t^2} - i\gamma |A|^2 A = 0 \tag{59}$$

Nevertheless, if nonuniform distributed amplification and dispersion management (DM) break the power symmetry required for exact compensation, nonlinearity control is still observed in conventional transmission lines [84] and reaches its maximum when the optical phase conjugator (PC) is placed in the middle of the link [85]. Simulations for constant-dispersion soliton systems with distributed amplification show the impact of the PC [86]. The parameters of the line are recalled in Table 8. Phase variance as a function of distance is represented in Figure 35 for a compound system that consists of three fiber sections, of lengths $z_1$, $z_2$ and $z_3$, respectively, separated by two PCs. Several positions are considered:

- Symmetrically placed PCs separated by equal distances (SE, $z_1 = z_2 = z_3 = z/3$),
- Symmetrically placed PCs separated by unequal distances (SU, $z_1 = z_3 = z/4$ and $z_2 = z/2$),
- Optimal case for asymmetrically placed PCs (A, $z_1 = z_2 = 2z/5$ et $z_3 = z/5$).

Compared to a reference system without OPC, the distances that can be reached with the same level of phase jitter are respectively multiplied by 2.08 (SE), 2.52 (SU), and 2.92 (A).

**Table 8. Parameters used in simulations (Figure 35).**

| | |
|---|---|
| Pulse shape | $\text{sech}^2$ |
| FWHM Pulsewidth (ps) | 30 |
| Pulse peak power (mW) | 0.60 |
| Dispersion ($ps^2$/km) | -0.3 |
| Attenuation (dB/km) | 0.21 |
| Nonlinear coefficient $\gamma$ ($km^{-1}.W^{-1}$) | 1.7 |
| Total length (km) | 9000 |
| Spontaneous emission factor | 1.1 |

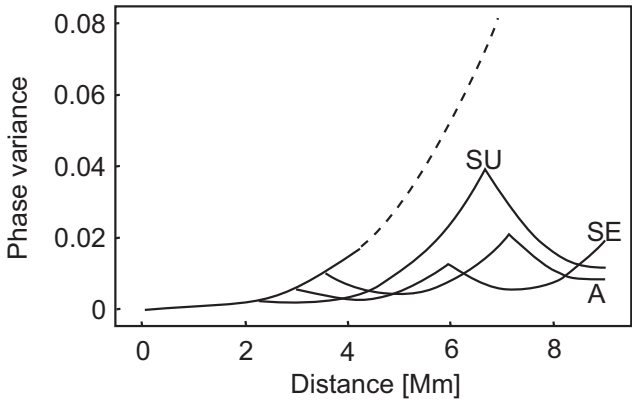


**Figure 35. Simulated phase variances plotted as a function of distance. The dashed curve represents a reference system without a PC, whereas the solid curves represent systems with two PCs at different locations.**

One can reduce the phase variance further by using post-transmission NPSC. The performances are expressed in Table 9 as the jitter reduction compared to the reference system without OPC and as the extension in the transmission reach.

**Table 9. Predicted performance improvements.**

| | | SE+NPSC | SU | SU+NPSC | A | A+NPSC |
|---|---|---|---|---|---|---|
| Jitter reduction | 9 | 36 | 16 | 16 | 25 | 25.8 |
| Range extension | 2.08 | 3.3 | 2.52 | 2.52 | 2.92 | 2.95 |

## 3.2 Phase jitter estimation in dispersion-managed systems by use of the moment method

In the last section, we presented the physical phenomenon and the different mechanisms that generate phase jitter. These random fluctuations have been studied by Ho, who computed the probability density functions of nonlinear phase noise [87, 88] and differential phase [89]. His work shows the inadequacy of the Gaussian approximation when one tries to give an accurate evaluation of a DPSK system performances. Nevertheless, his model is far from taking into account standard techniques used in real systems design such as dispersion management, filtering, and modulation format. The complexity of such transmission lines requires the computation of average quantities over a statistically significant number of noise sample functions. The computation time and power necessary to simulate the behavior of a transoceanic line with this brute force technique (Monte Carlo method) are significant. In this section, we describe some preliminary contributions we have made toward reducing the computational time in phase stability estimation.

### 3.2.1 Moment method

Developed since 1971, the moment method is successfully used in the computation of timing jitter occuring in dispersion-managed systems [14]. The idea consists of considering the optical pulse $u(z,t)$ as a particle with energy E, rms power P, and phase $\Phi$ defined by

$$E(z) = \int_{-\infty}^{+\infty} |u(z,t)|^2 \, dt \tag{60}$$

$$P(z) = \frac{1}{E} \int_{-\infty}^{+\infty} |u(z,t)|^4 \, dt \tag{61}$$

$$\Phi(z) = \frac{1}{E} \int_{-\infty}^{+\infty} |u(z,t)|^2 \arg(u(z,t)) \, dt \, . \tag{62}$$

These time-averaged quantities, called moments, respectively represent the energy, power, and phase of the optical field at a given distance z. Their evolutions are ruled by the optical pulse propagating in the fiber. Optical pulse propagation in the picosecond regime

is described by the scalar nonlinear Schrödinger equation:

$$i\frac{\partial u}{\partial z} - \frac{\beta_2(z)}{2}\frac{\partial^2 u}{\partial t^2} + \gamma(z)|u|^2 u = ig(z)u + \hat{F}(z,t)\,, \tag{63}$$

where $u(z,t)$ is the pulse envelope in a co-moving frame, $g(z)$ is the local net gain, and $\beta_2(z)$ is the local group-velocity dispersion. The coefficient $\gamma = n_2\omega_0/cA_{eff}$ is the local nonlinearity, where $n_2$ is the Kerr nonlinear index, $\omega_0$ is the signal central angular frequency, $c$ is the speed of light, and $A_{eff}$ is the fiber effective cross section. The noise source term is described by its autocorrelation function:

$$\langle \hat{F}(z,t)\hat{F}^*(z',t')\rangle = 2g_0\hbar\omega_0 n_{sp}(z)\delta(z-z')\delta(t-t')\,, \tag{64}$$

where $n_{sp}$ is the spontaneous emission factor, $g_0$ is the amplification coefficient inside the amplifier, and $\hbar\omega_0$ is the photon energy at the signal frequency.

### 3.2.2 Phase jitter Computation

Analytic derivations of the phase uncertainty for soliton systems were carried out using perturbation theory and the variational method. These studies assume an analytically determined pulse shape and a constant-dispersion optical link [12,13]. A semi-analytic model of the phase jitter was recently proposed for dispersion-managed soliton transmission [90], based on a Gaussian ansatz for the optical field. Here, we propose a semi-analytic approach that is valid for arbitrary pulses in dispersion-managed (DM) optical links. The following results were published in [91,92]. The principle of this derivation is to split the propagation problem into its deterministic and random parts. The probabilistic aspect of the problem is solved analytically, thereby avoiding the computation of average quantities over a statistically significant number of noise sample functions. The deterministic part of the problem is carried out numerically by use of the split-step Fourier algorithm. The obtained unperturbed optical field is used together with the moment method [93] and statistical properties of the noise to evaluate phase jitter to first order. This approach is validated by comparison with direct Monte Carlo simulations in a DM soliton system and a quasilinear channel,

which both show excellent agreement. The computation time necessary to evaluate the impact of phase jitter on a communication system is thereby reduced from hours to seconds on current desktop computers. This method also provides some physical insight about the mechanisms that create phase jitter in the context of arbitrary optical pulses. In addition to the moments defined by equations (60)–(62),

$$\Omega^2 \;=\; -\frac{1}{2E}\int_{-\infty}^{+\infty} \frac{(uu_t^*)^2 + (u^*u_t)^2}{|u|^2}\,dt \tag{65}$$

represents the square of the angular frequency of the optical field at a given distance. The subscript $t$ denotes the partial time derivative. Differentiating $\Phi$ and $P$ with respect to $z$, and using the propagation equation (1), we obtain these dynamic equations:

$$\begin{cases} \dfrac{\mathrm{d}\Phi}{\mathrm{d}z} &= \gamma P - \dfrac{\beta_2}{2}\Omega^2 + \dfrac{i}{E}\displaystyle\int_{-\infty}^{+\infty} (\arg(u) - \Phi)\left(u\hat{F}^* - u^*\hat{F}\right)\,dt \\ & \quad -\dfrac{1}{2E}\displaystyle\int_{-\infty}^{+\infty} u^*\hat{F} + u\hat{F}^*\,dt \end{cases} \tag{66}$$

$$\begin{cases} \dfrac{\mathrm{d}P}{\mathrm{d}z} &= 2gP + \dfrac{\beta_2}{E}\displaystyle\int_{-\infty}^{+\infty} |u|^4\,(\arg(u))_{tt}\;dt + \dfrac{i}{E}\displaystyle\int_{-\infty}^{+\infty} \left(2|u|^2 - P\right)\left(u\hat{F}^* - u^*\hat{F}\right)\,dt\,. \end{cases} \tag{67}$$

If we assume that the pulse exhibits mostly linear chirp, then

$$\arg(u)(z,t) \approx \phi_0(z) + \phi_2(z)(t - t_0)^2\,, \tag{68}$$

where $t_0$ is the temporal position of the pulse, and these dynamic equations can be rewritten as [94]

$$\begin{cases} \dfrac{\mathrm{d}\Phi}{\mathrm{d}z} &= -\beta_2\phi_2\Phi + \gamma P + \dfrac{i}{E}\displaystyle\int_{-\infty}^{+\infty} (\arg(u) - \Phi)\left(u\hat{F}^* - u^*\hat{F}\right)dt \\ & \quad -\dfrac{1}{2E}\displaystyle\int_{-\infty}^{+\infty} \left(u^*\hat{F} + u\hat{F}^*\right)\,dt \end{cases} \tag{69}$$

$$\begin{cases} \dfrac{\mathrm{d}P}{\mathrm{d}z} &= 2(g + \beta_2\phi_2)P + \dfrac{i}{E}\displaystyle\int_{-\infty}^{+\infty} \left(2|u|^2 - P\right)\left(u\hat{F}^* - u^*\hat{F}\right)dt \end{cases} \tag{70}$$

These equations have simple physical interpretations. The mean phase accumulates proportionnaly to power through self-phase modulation (SPM). Phase variations also arise from chirp fluctuations through group-velocity dispersion. The last two terms in equation (69) represent the direct contribution of noise to phase evolution. The power varies as a function of gain and dispersion. Noise also contributes directly to power variations through the last term on the right-hand side of equation (70).

**Method of variation of parameters 1** *Let y be a continuous and differentiable function on an interval I with* $\frac{dy}{dx} + a(x)y = f(x)$ *and f continuous on I; then, the general solution of this differential equation is*

$$y(x) = e^{-A(x)} \int_0^x f(u)e^{A(u)}\,du \quad \textit{where } A(x) = \int_0^x a(u)\,du.$$

Using the method of variation of parameters, we can implicitly integrate the dynamic equation that governs the evolution of power.

$$P = \left\{ P_0 + i \int_0^z \left[ \frac{1}{EA_1} \int_{-\infty}^{+\infty} \left( (2|u|^2 - P) \right) \left( u\hat{F}^* - u^*\hat{F} \right) dt \right] dz_1 \right\} A_1 \,, \tag{71}$$

where

$$A_1(z) = \exp\left( \int_0^z 2(g + \beta_2\phi_2)\, dz_1 \right) . \tag{72}$$

Similarly, an implicit solution for the mean phase equation is given by

$$\Phi = \Phi_1 + \Phi_2 + \Phi_3 \,, \tag{73}$$

where

$$\Phi_1 = A_2 \int_0^z \frac{\gamma P}{A_2}\, dz_1 \tag{74}$$

$$\Phi_2 = iA_2 \int_0^z \left[ \frac{1}{EA_2} \int_{-\infty}^{+\infty} (\arg(u) - \Phi) \left( u\hat{F}^* - u^*\hat{F} \right) dt \right] dz_1 \tag{75}$$

$$\Phi_3 = -\frac{A_2}{2} \int_0^z \left[ \frac{1}{EA_2} \int_{-\infty}^{+\infty} u^*\hat{F} + u\hat{F}^*\, dt \right] dz_1 \tag{76}$$

$$A_2 = \exp\left( - \int_0^z \beta_2\phi_2\, dz_1 \right) . \tag{77}$$

Under these assumptions, the noise-free field can be used in the right-hand sides of equations (71) and (73) since the perturbed field only adds second- and higher-order corrections to the phase. The phase variance can be calculated using equations (64), (71), and (73):

$$\sigma_\Phi^2 = \langle \Phi^2 \rangle - \langle \Phi \rangle^2 = \langle \Phi_1^2 \rangle + \langle \Phi_2^2 \rangle + \langle \Phi_3^2 \rangle + 2\langle \Phi_1 \Phi_2 \rangle \,, \tag{78}$$

where defining the scalar product

$$(\delta q_i, \delta q_j) = \int_{-\infty}^{+\infty} \delta q_i \delta q_j^* + \delta q_i^* \delta q_j \, dt \,, \tag{79}$$

and the functions

$$\delta q_1 = 2i \sqrt{g n_{sp} \hbar \omega_0} \frac{2|u|^2 - P}{E A_1} u \tag{80}$$

$$\delta q_2 = 2i \sqrt{g n_{sp} \hbar \omega_0} \frac{\arg(u) - \Phi}{E A_2} u \tag{81}$$

$$\delta q_3 = 2 \sqrt{g n_{sp} \hbar \omega_0} \frac{u}{E A_2} \,. \tag{82}$$

We find

$$\langle \Phi_1^2 \rangle = A_2^2 \int_0^z \frac{\gamma A_1}{A_2} \int_0^{z_1} \frac{\gamma A_1}{A_2} \int_0^{z_2} (\delta q_1, \delta q_1) \, dz_3 \, dz_2 \, dz_1 \tag{83}$$

$$\langle \Phi_2^2 \rangle = \frac{A_2^2}{2} \int_0^z (\delta q_2, \delta q_2) \, dz_1 \tag{84}$$

$$\langle \Phi_3^2 \rangle = \frac{A_2^2}{8} \int_0^z (\delta q_3, \delta q_3) \, dz_1 \tag{85}$$

$$2\langle \Phi_1 \Phi_2 \rangle = A_2^2 \int_0^z \gamma A_1 \int_0^{z_1} (\delta q_1, \delta q_2) \, dz_2 \, dz_1 \,. \tag{86}$$

The cross products $\langle \Phi_1 \Phi_3 \rangle$ and $\langle \Phi_2 \Phi_3 \rangle$ are reduced to zero owing to orthogonality properties of the noise components. Equations (78)–(86) represent the main result of this section, and are valid for arbitrary pulse shapes and communication systems, provided that the chirp remains essentially linear throughout the propagation. Once the deterministic optical field is known, one can use it in the right-hand sides of equations (83)–(86) to evaluate the phase jitter. The quantity $\langle \Phi_1^2 \rangle$ can be identified as the phase jitter induced by power fluctuations through SPM, $\langle \Phi_2^2 \rangle$ and $\langle \Phi_3^2 \rangle$ are direct contributions from the noise to phase jitter, and $\langle \Phi_1 \Phi_2 \rangle$ is the interference term between these two effects.

#### *3.2.2.1 Phase jitter control by in-line filtering*

In-line filtering was first proposed to reduce the timing jitter [95] and was experimentally demonstrated in a dispersion-managed (DM) system [96]. It was later shown to stabilize the phase as well in the frame of constant dispersion soliton links [12]. The physical mechanism for phase control is as follows: optical filters stabilize the pulse spectral width and hence peak power since these variables are coupled by nonlinear soliton propagation. The control of the peak power then acts on the stability of the phase accumulated by self-phase modulation. In DM systems, the periodic chirping of the pulse complicates the analysis [93], and the effect of filtering on the phase jitter must be reconsidered.

A periodic filtering whose spatial period is $z_f$ can modeled by a distributed filtering that has the same effect on the soliton [97]. Considering only the effect of the filter, we have

$$\tilde{u}(\omega, z_f) = \tilde{u}(\omega, 0)\, T(\omega)\,, \tag{87}$$

where $\tilde{u}$ denotes the Fourier transform of $u$ and $T(\omega)$ is the filter transfer function. Equation (87) is the solution at $z = z_f$ of

$$\frac{\partial \tilde{u}}{\partial z} = \frac{\ln T(\omega)}{z_f}\, \tilde{u}. \tag{88}$$

In the case of Gaussian-shaped filters with FWHM bandwidth B, $T(\omega)$ has the following form:

$$T(\omega) = e^{-[\frac{\omega}{\pi B}\sqrt{\frac{\ln(2)}{2}}]^2} \tag{89}$$

and equation (88) becomes

$$\frac{\partial u}{\partial z} - \frac{\ln(2)}{2}\frac{1}{\pi^2 B^2 z_f}\frac{\partial^2 u}{\partial t^2} = 0\,. \tag{90}$$

If $b = \dfrac{\ln(2)}{\pi^2 B^2 z_f}$, we can write the NLSE perturbed by the distributed filtering

$$i\frac{\partial u}{\partial z} - \frac{1}{2}[\beta_2(z) - ib(z)]\frac{\partial^2 u}{\partial t^2} + \gamma(z)\,|u|^2 u = i\,g(z)\,u + \hat{F}(z,t). \tag{91}$$

$b$ characterizes the filter strength. The dynamic equations (69)–(70) can be rewritten as

$$\begin{cases} \dfrac{d\Phi}{dz} &= -\beta_2\phi_2\Phi + \gamma P + \dfrac{i}{E}\displaystyle\int_{-\infty}^{+\infty} (\arg(u) - \Phi)\left(u\hat{F}^* - u^*\hat{F}\right)\, dt \\ & \quad -\dfrac{1}{2E}\displaystyle\int_{-\infty}^{+\infty}\left(u^*\hat{F} + u\hat{F}^*\right)\, dt \qquad (92) \\ \dfrac{dP}{dz} &= 2\left[g + \beta_2\phi_2 - \dfrac{\mathbf{b(z)}}{\mathbf{2E}}\displaystyle\int_{-\infty}^{+\infty} |\mathbf{u_t}|^2\mathbf{dt}\right]P + \dfrac{i}{E}\displaystyle\int_{-\infty}^{+\infty}\left(2|u|^2 - P\right)\left(u\hat{F}^* - u^*\hat{F}\right)\, dt\,, \qquad (93) \end{cases}$$

where only first-order terms in b were kept. The power is given by

$$P = \left\{P_0 + i\int_0^z \left[\frac{1}{EA_1}\int_{-\infty}^{+\infty}\left((2|u|^2 - P)\right)\left(u\hat{F}^* - u^*\hat{F}\right)\, dt\right] dz_1\right\}A_1\,, \qquad (94)$$

where

$$A_1(z) = \exp\left[\int_0^z 2\left(g + \beta_2\phi_2 - \frac{b(z)}{2E}\int_{-\infty}^{+\infty}|u_t|^2 dt\right) dz_1\right]\,. \qquad (95)$$

The filtering term changes the overall behavior of the solution. The correction acts on the multiplicative term $A_1(z)$, dampening the fluctuations of P. It results in a smaller power noise and hence nonlinear phase noise since it is induced by power fluctuations through self-phase modulation. The derivation formally gives the same results, equations (78)–(86), with the exception of the modified $A_1(z)$ term.

### 3.2.3 Validation of the moment method

To demonstrate the versatility of the moment method, we apply it to two filtered DM systems with different levels of nonlinearity and filter strength, and check our model by comparing it to direct Monte Carlo simulations. Using the split-step Fourier algorithm, the propagation of a single pulse in a noisy channel was simulated 512 times to compute the phase variance. As only single pulses at a single wavelength were considered, patterning effects that may arise in real WDM communication systems are not studied here. The time, frequency, and distance resolutions were 500 fs, 2 GHz, and 1 km, respectively. The optical links are formed by alternating spans of anomalous dispersion fiber 1 and normal dispersion fiber 2. The DM soliton link operates at a high peak power and average dispersion

$D_a$ = 0.5 ps/nm.km, while the quasilinear system operates at low power, with zero average dispersion. Unchirped pulses are launched at midpoint of the normal dispersion span. The systems' parameters are summarized in Table 10. For both systems, optical amplifiers followed by Gaussian filters are placed every $z_a$ = 60 km along the link, with $n_{sp}$ = 1.5. Because filters remove some signal power in the wings of the pulse spectra, the gain of the amplifiers must be slightly increased to conserve energy.

**Table 10. Numerical values of the systems' parameters.**

| | DM soliton | DM quasilinear |
|---|---|---|
| Pulse shape | $\text{sech}^2$ | Gaussian |
| FWHM Pulsewidth (ps) | 20 | 20 |
| Pulse peak power (mW) | 7.2 | 0.5 |
| Fiber 1 dispersion (ps/nm.km) | 11 | 16 |
| Fiber 1 length (km) | 30 | 50 |
| Fiber 1 effective area ($\mu$m$^2$) | 50 | 80 |
| Fiber 2 dispersion (ps/nm.km) | -10 | -80 |
| Fiber 2 length (km) | 30 | 10 |
| Fiber 2 effective area ($\mu$m$^2$) | 50 | 45 |

The phase standard deviation is plotted in Figure 36 for propagation distances less than 1 Mm. For the quasilinear system, we observe a global linear dependence of the phase variance to propagation distance, because terms $\langle\Phi_2^2\rangle$ and $\langle\Phi_3^2\rangle$ dominate because of the low peak power. The phase uncertainty exhibits rapid oscillations that are imparted by the dynamics of the pulse inside a DM cell. As the variation of group-velocity dispersion is large in the case of the quasilinear system, these oscillations are particularly strong. Our method reproduces these oscillations' locations and amplitudes accurately. For the DM soliton system, the cubic dependence of the phase variance obtained in the case of constant-dispersion soliton channels [12] is still observed. This is due to the predominance of the $\langle\Phi_1^2\rangle$ term since the large optical peak power gives rise to significant SPM, thus transferring amplitude noise to the phase. Variations at the scale of the DM cell are small because of the low value of the dispersion map strength considered.

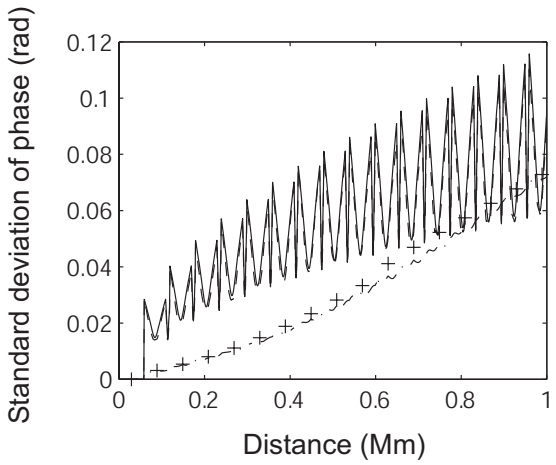


**Figure 36. Standard deviation of the phase as a function of distance over 1 Mm. Quasi-linear system, Monte Carlo (solid) and moment method (dash). DM soliton system, Monte Carlo (dash dot) and moment method (crosses).**

For distances over 1 Mm, we only plotted the phase standard deviation at the locations of optical amplifiers for clarity (Figure 37). For the quasilinear case, the moment method results are in good agreement with Monte Carlo simulations for all distances. For the DM soliton case, we note that the oscillations of the phase uncertainty on a long-distance scale are reproduced with good accuracy. The moment method slightly overestimates the locations of these oscillations, probably because of second-order effects. We note that the phase jitter curves for the two systems cross at approximately 1 Mm. This observation can be physically interpreted as follows. Equations (80)–(82) show that the impact of noise on phase jitter is inversely proportional to the energy per pulse. In the short distance case, the direct contribution from ASE to phase noise predominates. The quasilinear system, operating at low energy per pulse, is more affected by noise. As the propagation distance grows, the contribution from nonlinear phase noise grows rapidly when the operating power is high. Therefore, the phase jitter in the DM soliton case grows faster than in the quasilinear case, resulting in a higher phase jitter for distances greater than 1 Mm. This shows the need for phase control techniques, particularly in the case of highly nonlinear transmission systems.

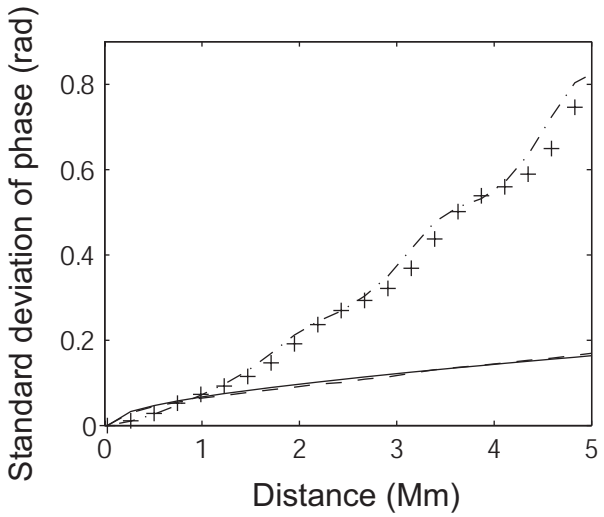


**Figure 37. Standard deviation of the phase as a function of distance over 5 Mm. Quasi-linear system, Monte Carlo (solid) and moment method (dash). DM soliton system, Monte Carlo (dash dot) and moment method (crosses).**

Therefore, we included filtering in the numerical simulations. Its influence is particularly important for the DM soliton system operating at high peak power. In this case, the standard deviation of the phase is plotted in Figure 38 for different filter bandwidths.

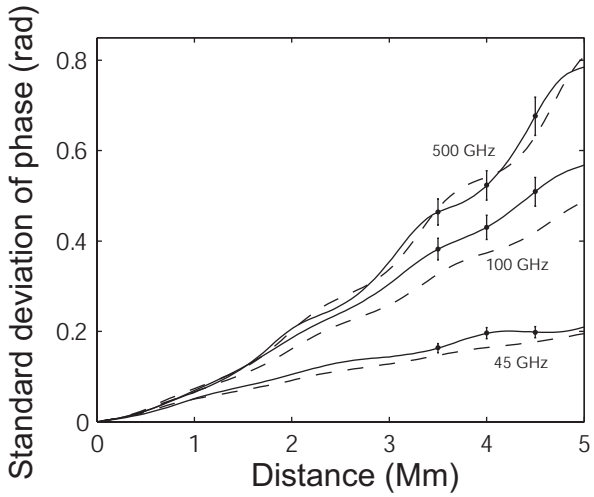


**Figure 38. Standard deviation of the phase as a function of distance for the DM soliton system with optical filters bandwidths of 500 GHz, 100 GHz, and 45 GHz. The solid line represents Monte Carlo simulation results while the dashed line represents the moment method results.**

The 500 GHz filter case corresponds to an almost unfiltered system since the signal bandwidth is about 15 GHz. We observe that the phase standard deviation is greatly reduced by narrowband filtering. It exhibits a $\sqrt{z}$ dependence in the case of 45 GHz filters, which is similar to the constant dispersion soliton case [12]. Although the moment method does not predict accurately the locations of the slight oscillations, there is satisfactory agreement with Monte Carlo simulations. The mismatch in oscillation locations might be due to a small amount of nonlinear chirping in the pulses and to higher-order terms in the filtering factor *b*. The filtering is not as efficient at suppressing phase jitter in the case of the quasilinear system, as shown in Figure 39. This can be explained by noting that it is operating at low power, with a weak nonlinear phase noise contribution. Since the filters essentially act by stabilizing the power of the pulses and therefore reduce the nonlinear part of phase noise mediated by SPM, they do not have an important effect on the quasilinear system.

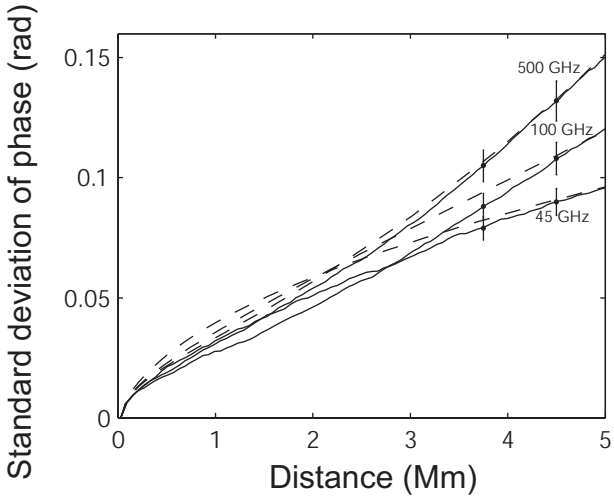


**Figure 39. Standard deviation of the phase as a function of distance for the DM quasillinear system with optical filters bandwidth of 500 GHz, 100 GHz, and 45 GHz. The solid line represents Monte Carlo simulation results while the dashed line represents the moment method results.**

To further clarify this stabilizing mechanism, we have plotted in Figure 40 the linear and nonlinear contributions to phase jitter in the cases of the weakly and strongly filtered DM soliton systems, as given by the moment method. The linear contribution corresponds to

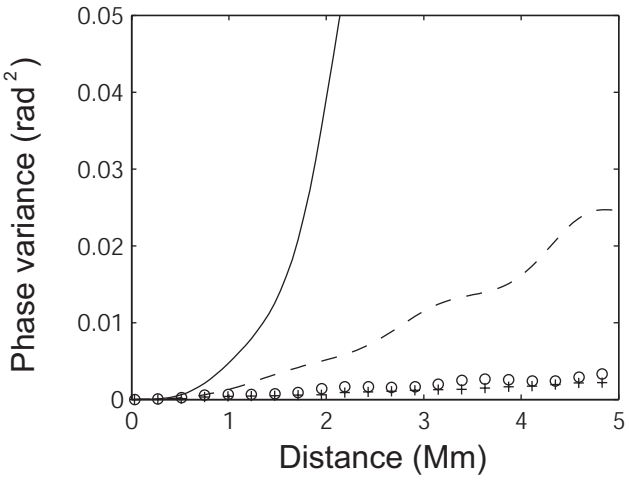


**Figure 40. Contribution of the nonlinear phase noise to the overall phase jitter for the DM soliton system. Solid line: nonlinear phase variance with 500 GHz filters. Dashed line: nonlinear phase variance with 45 GHz filters. Circles: linear phase variance for 500 GHz filters. Crosses: linear phase variance for 45 GHz filters.**

setting $\gamma = 0$ in equation (63). For 500 GHz filters, the nonlinear contribution to the phase variance reaches 0.6 rad$^2$ at 5 Mm and grows as $z^3$. When 45 GHz filters are used, the nonlinear phase variance is reduced to 0.025 rad$^2$ at 5 Mm, growing approximately linearly with distance. The linear contribution to phase variance is almost unchanged under strong filtering.

Assuming a perfect phase receiver (Figure 41) and a Gaussian probability density function, the probabilities $P(0/\pi)$ of detecting 0 when $\pi$ was sent and inversely are

$$\begin{cases} P(0/\pi) = \dfrac{1}{\sigma\sqrt{2\pi}} \displaystyle\int_{-\infty}^{\pi/2} e^{-\frac{t^2}{2\sigma^2}}\, dt & (96) \\ P(\pi/0) = \dfrac{1}{\sigma\sqrt{2\pi}} \displaystyle\int_{\pi/2}^{+\infty} e^{-\frac{t^2}{2\sigma^2}}\, dt\,. & (97) \end{cases}$$

As the phases 0 and $\pi$ are equiprobable, the bit error rate is given by

$$BER = \frac{1}{2}[\, P(0/\pi) + P(\pi/0)\,], \tag{98}$$

which finally takes the final form

$$BER = \frac{1}{2}\,\mathrm{erfc}\left(\frac{\pi}{2\sqrt{2}\sigma}\right). \tag{99}$$

The standard deviation that yields a symbol error rate of $10^{-9}$ is 0.26 rad for binary DPSK and 0.13 rad for quadrature DPSK. For the DM soliton system, narrowband filtering allows error-free transmission over 5 Mm for binary DPSK and over 2.5 Mm for quadrature DPSK. For the quasilinear system no filtering is required for binary DPSK, while 45 GHz filters allow the error-free transmission of quadrature DPSK over 5 Mm.

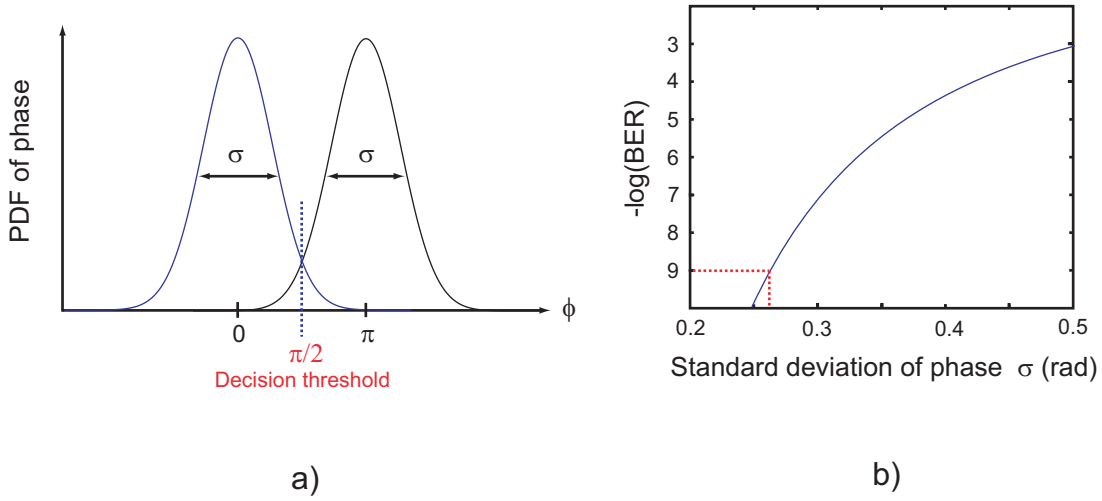


**Figure 41. a) Probability density function of phase (DPSK), b) Bit error rate as a function of standard deviation of phase (DPSK).**

**Comment for WDM systems:**

Note that our method only takes into account the interaction of a single pulse with ASE noise, neglecting other contributions to phase jitter that might arise in WDM systems, such as pulse-to-pulse intra- and inter-channel interactions. Both FWM and XPM result in interactions between pulses within a channel and from different channels. In dispersion-managed systems, interchannel FWM is not phase matched, so that its overall influence on the propagation in small. The contribution from interchannel XPM to phase jitter was shown to grow as the distance square in a constant-dispersion soliton system [98]. However, it has a small impact on the performance of such systems because the random phase shifts experienced by successive pulses are highly correlated, so that they cancel when a differential modulation format is used.

The impact of intrachannel effects on phase jitter is not yet clearly assessed. To make a first evaluation of their eventual contribution, we made simulations of the propagation of seven pulses, each carrying a random phase chosen in the set $[0, \pi]$, in both the aforementioned systems. The phase jitter for the central pulse was evaluated using Monte Carlo simulations, which take pulse-to-pulse interactions into account, and we also used the moment method approach, which only takes into account the interaction with ASE noise. The isolation of the central pulse was performed by evaluating all time integrals over the central bit slot only. The pulse repetition period was $T = 100$ ps, which yielded a moderate overlap in the DM soliton system (maximum FWHM pulse width to time slot ratio $\tau_{max}/T = 0.34$), and strong overlap for the quasilinear system ($\tau_{max}/T = 0.70$).

The phase standard deviation as a function of distance at chirp-free points obtained in the multipulse simulation is plotted in Figure 42. For the DM soliton system, the result is very similar to the single-pulse case, which indicates that intrachannel pulse-to-pulse interactions play a minor role in the generation of phase jitter for this link. For the quasilinear case, the overlap is strong, so that the computation of the average phase of a pulse given by equation (62) is meaningful only at chirp-free points, when pulses are confined to their time slot. At other points, the contribution of neighboring pulses to the integral makes impossible the numerical evaluation of the average phase for a given pulse. This comment applies to both the Monte Carlo and the moment method. We observe that the Monte Carlo curve does not deviate significantly from the single-pulse case, indicating that intrachannel effects bring only a weak contribution to phase jitter. However, the moment method is less accurate than in the single-pulse case because the scalar products of equations (83)–(86) are nonzero only at amplifier locations, where the overlap is maximum. Despite this effect, the moment method performs reasonably well. Thus, for the systems considered here, ASE noise and SPM appear to be the dominant mechanisms at the origin of phase jitter. However, the effects of intrachannel interactions in the general context of phase-encoded signals remain to be studied in depth.

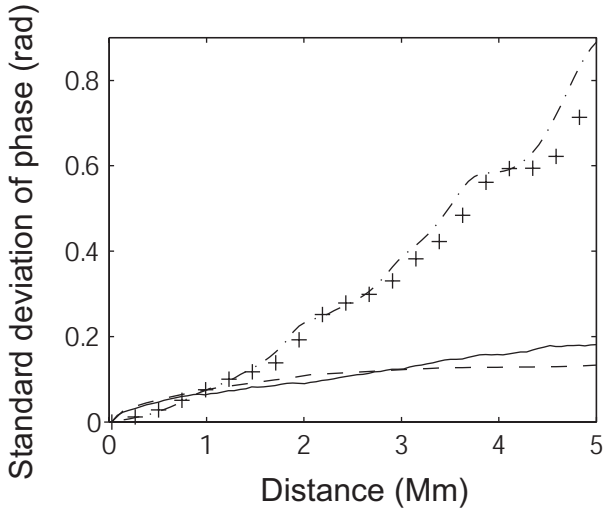


**Figure 42. Standard deviation of the phase as a function of distance over 5 Mm for the multipulse simulation. Quasi-linear system, Monte Carlo (solid) and moment method (dash). DM soliton system, Monte Carlo (dash dot) and moment method (crosses).**

### 3.2.4 Phase jitter control by phase conjugation

Among the techniques that have been proposed [4, 5], and later developed [79, 99] to limit this nonlinear amplitude-to-phase noise conversion also known as the Gordon-Mollenauer effect, spectral inversion (SI) or optical phase conjugation promised to be effective [86]. As previously seen in section 3.1.3.2, midspan spectrum inversion makes the phase-conjugate signal experience opposite dispersion and nonlinearity in the second half of the link providing a partial compensation [9]. In this paragraph, we present the evaluation of phase jitter in single-channel DM soliton (DMS) links using spectral inversion.

Given that the propagation of the phase-conjugated field $u^*$ in the second half of the link is equivalent to changing the sign of the local group-velocity dispersion $\beta_2$ and nonlinearity $\gamma$ [9], the NLSE can be generalized to take spectral inversion (SI) into account:

$$i\frac{\partial u}{\partial z} - \frac{1}{2}\left[\epsilon\beta_2(z) - ib(z)\right]\frac{\partial^2 u}{\partial t^2} + \epsilon\,\gamma(z)|u|^2 u = i\,g(z)\,u + F(z,t)\,, \tag{100}$$

When $\epsilon$ evaluates to 1, Eq. (1) describes the standard propagation of the optical field before SI. When $\epsilon$ evaluates to $-1$, Eq. (1) describes the propagation of the phase-conjugated field after SI. Following the same method, we get a generalized dynamic system we derived a

further generalized dynamic system

$$\begin{cases} \dfrac{\mathrm{d}\Phi}{\mathrm{dz}} &= -\epsilon\beta_2\phi_2\Phi + \epsilon\gamma P + \dfrac{i}{E}\displaystyle\int_{-\infty}^{+\infty} (\arg(u) - \Phi) \times \left(u\hat{F}^* - u^*\hat{F}\right) dt \\ & \quad -\dfrac{1}{2E}\displaystyle\int_{-\infty}^{+\infty} \left(u^*\hat{F} + u\hat{F}^*\right) dt \qquad (101) \\ \dfrac{\mathrm{d}P}{\mathrm{dz}} &= 2\left[g + \epsilon\beta_2\phi_2 - \dfrac{b(z)}{2E}\displaystyle\int_{-\infty}^{+\infty} |u_t|^2 dt\right] P + \dfrac{i}{E}\displaystyle\int_{-\infty}^{+\infty} \left(2|u|^2 - P\right)\left(u\hat{F}^* - u^*\hat{F}\right) dt \qquad (102) \end{cases}$$

The result presented in this paragraph concerns the propagation **after** SI where now $\epsilon = -1$. This sign change does not affect the direct contribution of noise to the phase variance, since linear phase kicks introduced at each amplifier are independant of one another. On the other hand the nonlinear phase kicks are related to the peak power at the location of the amplifier, which is correlated to the previous values of peak powers. This in turn leads to correlation between nonlinear phase kicks. As a result, changing the sign of $\gamma$ introduces somme anticorrelation between nonlinear phase kicks before and after SI, reducing the overall phase noise. From this observation, the only contribution to phase jitter that needs to be fully reevaluated when operating in the phase-conjugated section of the link is the nonlinear part of the phase.

The formal form of any parameter $X(z)$ expressed before SI can also be used after SI if one shifts the origin to the spectral inverter location ($z = L_1$) and reverses the sign of $\beta_2$ and $\gamma$. $\hat{X}(z)$ will then refer to the evolution of the parameter $X$ after SI in the new coordinate system. Applying this to the nonlinear phase $\Phi_1$ gives its expression $\hat{\Phi}_1$ after SI:

$$\hat{\Phi}_1(z) = \Phi_1(L_1) - \hat{A}_2 \int_0^z \frac{\gamma\hat{P}(z_1)}{\hat{A}_2}\, dz_1 \qquad (103)$$

with power fluctuations given by

$$\hat{P}(z) = \hat{A}_1 \left\{ P(L_1) + i\int_0^z \left[ \frac{1}{\hat{E}\hat{A}_1} \int_{-\infty}^{+\infty} \left( (2|u|^2 - \hat{P}) \right) \times (uF^* - u^*F)\, dt \right] dz_1 \right\} \qquad (104)$$

with

$$\hat{A}_1(z) = \exp\left[ \int_0^z 2\left( g - \beta_2\phi_2 - \frac{b(z)}{2E} \int_{-\infty}^{+\infty} |u_t|^2 dt \right) dz_1 \right], \qquad (105)$$

$$\hat{A}_2(z) \;=\; \exp\left[\int_0^z \beta_2\phi_2\, dz_1\right]. \tag{106}$$

The total phase variance due to the Gordon-Mollenauer effect is then given by

$$\langle\hat{\Phi}_1^2\rangle = \langle\Phi_1(L_1)^2\rangle + \sigma^2_{\Phi_{PC_1}}(z) - \sigma^2_{\Phi_{PC_2}}(z)\,. \tag{107}$$

The first term, computed from (83), accounts for the phase jitter accumulated before the spectral inversion which effect is further analyzed. The nonlinearity control provided in the second half of the link is materialized by the negative term in (107) which forces the total phase variance to increase at a slower rate. The natural tendency observed before conjugation is still observed in $\sigma^2_{\Phi_{PC_1}}$, but its impact is limited by $\sigma^2_{\Phi_{PC_2}}$. These contributions are given by

$$\sigma^2_{\Phi_{PC_1}}(z) \;=\; G(z)\Big(\int_0^z (\delta\hat{q}_1,\delta\hat{q}_1)\,dz_3 + A_1^2(L_1)\int_0^{L_1}(\delta q_1,\delta q_1)\,dz_3 + 2\,A_1(L_1)\times\int_0^{\min(z,L_1)}(\delta q_1',\delta q_1')\,dz_3\Big) \tag{108}$$

$$\sigma^2_{\Phi_{PC_2}}(z) \;=\; -\frac{3}{8}H(z)\Big(A_1(L_1)A_2(L_1)\times\int_0^{L_1}(\delta q_1,\delta q_1)\,dz_3 + A_2(L_1)\int_0^{\min(z,L_1)}(\delta\hat{q_1}',\delta\hat{q_1}')\,dz_2\Big) \tag{109}$$

The functions G, H, $\delta q_1$, $\delta\hat{q}_1$ and $\delta q_1'$ are given by

$$G(z) \;= \hat{A}_2^2(z)\int_0^z \frac{\gamma\hat{A}_1}{\hat{A}_2}(z_1)\int_0^{z_1}\frac{\gamma\hat{A}_1}{\hat{A}_2}(z_2)\,dz_2\,dz_1\,, \tag{110}$$

$$H(z) \;= \hat{A}_2(z)\int_0^{L_1}\frac{\gamma A_1}{A_2}(z_2)\,dz_2\int_0^z\frac{\gamma\hat{A}_1}{\hat{A}_2}(z_3)\,dz_3\,, \tag{111}$$

$$\delta q_1 \;=\; 2i\sqrt{gn_{sp}\hbar\omega_0}\,\frac{2|u|^2-P}{EA_1}u\,, \tag{112}$$

$$\delta\hat{q}_1 \;=\; 2i\sqrt{gn_{sp}\hbar\omega_0}\,\frac{2|u|^2-\hat{P}}{\hat{E}\hat{A}_1}u\,, \tag{113}$$

$$\delta q_1' \;=\; 2i\sqrt{gn_{sp}\hbar\omega_0}\,\frac{2|u|^2-\hat{P}}{E\sqrt{A_1\hat{A}_1}}u\,. \tag{114}$$

G(z) and H(z) are the dominant functions that determine the evolution of the phase variance after the conjugation. Their relative variations explain the existence of a distance for which phase jitter is minimum.

The standard deviation of the soliton phase is plotted in Figure 43 for different filter bandwidths with and without midlink spectral inversion. As the signal bandwidth is about 15 GHz, the 500 GHz filter case corresponds to an almost unfiltered system. We observe that the phase standard deviation is greatly reduced by spectral inversion. This reduction is less effective when tight filtering is used. This can be explained by noting that the amount of nonlinear phase noise accumulated in the first half of the link is less important in that case. Nevertheless, midlink spectral inversion enables unfiltered systems to show the same performance after 6000 km as standard 100 GHz systems. We also note a satisfactory agreement between the results of the moment method and those of the Monte-Carlo simulations.

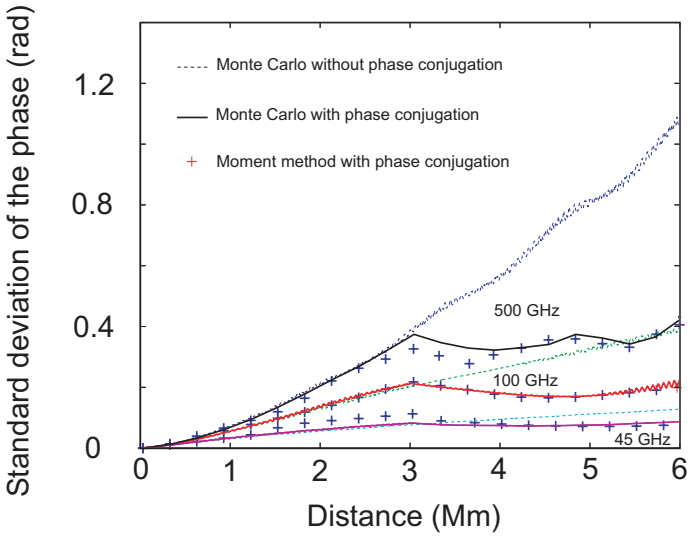


**Figure 43. Standard deviation of the phase as a function of distance for the DM soliton system with and without spectral inversion.**

The phase variance $\langle \Phi_1^2 \rangle$ resulting from the nonlinear phase noise mediated by SPM is plotted in Figure 44 for the case of 100 GHz filters. Its different contributions (shown

in dashed lines) after spectral inversion directly reflect the dominant behavior of the functions G(z) and H(z) defined in Equations (110)-(111). Their relative variations modify the overall evolution in a way similar to the constant dispersion soliton case [86] where nonlinearity control is achieved and results in the existence of a minimum value for the phase jitter. Since this minimum is reached somewhere in the second half part of the propagation, midlink spectral inversion is certainly not optimal. This leads us to study the impact of the SI location.

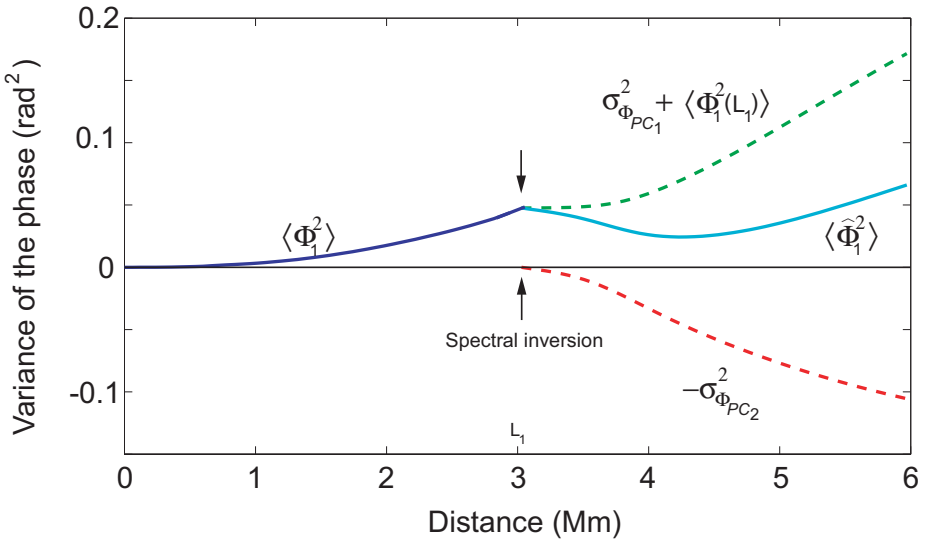


**Figure 44. Variance of the nonlinear phase as a function of distance for the 100 GHz DMS system.**

Figure 45 depicts the evolution of the standard deviation of the phase as a function of distance when the location of the spectral inverter is changed from its symmetrical position ($L_1$ = 3000 km), respectively to 2500, 4000 and 4500 km. The latter two cases correspond to a [2/3]- and [3/4]-link SI.

First, we can see that if SI is performed before midlink, we rapidly lose the benefit of nonlinear compensation, since we observe a growth similar to the one observed without SI for the same system in Figure 43. This can be explained by the fact that after $L_1$ km propagation in the second half of the link, Equation (109) has a different behavior. In that

case, $min(z, L_1) = L_1$, which means that the multiplicative term modulating $H(z)$ is now constant. If the same conclusion can be drawn for the analog term in Equation(108), the overall multiplicative coefficient in front of $G(z)$ is still dependent on z, which leads to a nonlinear phase jitter evolution very similar to the one before spectral inversion.

The similarity is also reflected in the notations, since the driving term of $\sigma^2_{\Phi_{PC_1}} - \sigma^2_{\Phi_{PC_2}}$ is $G(z) \times \int_0^z (\delta\hat{q}_1, \delta\hat{q}_1)\, dz_3$ and can be compared to its counterpart before SI expressed by Equation (83). Intuitively, the potential correlations between phase kicks before and after SI can not extend beyond a propagation distance of $2\,L1$.

Finally, when SI is performed after the midlink point, the results show that the best location is very close to [2/3]-link. In this quasi-optimal case, the maximum nonlinear phase jitter control is achieved just before 6000 km and results in a 2.11 range extension.

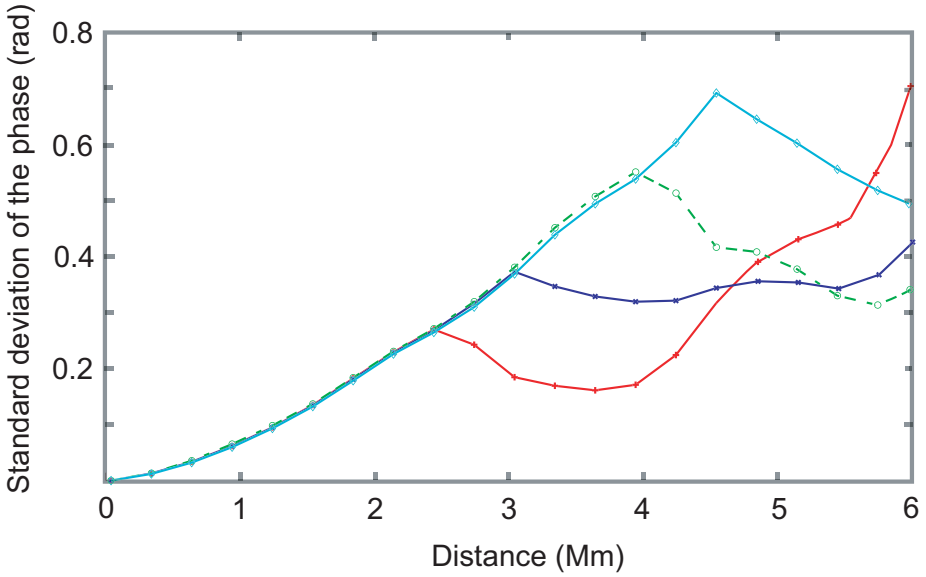


**Figure 45. Phase variance evolution as a function of the spectral inverter location for the 100 GHz DMS system.**

## 3.3 Effect of sliding filters on the soliton optical phase jitter in constant-dispersion systems

We just showed that in-line filtering reduces phase jitter efficiently through the damping of amplitude noise, which results in a linear increase of the phase jitter with distance. The main drawback of this technique is that the ASE noise that has exactly the soliton center frequency is less attenuated than the soliton itself and grows exponentially with distance, creating a strong continuum wave that deteriorates the transmission. To overcome this limitation, the idea of sliding-frequency guiding filters was proposed [100] and demonstrated [101–103] in the context of timing jitter. The principle is to slightly shift the central frequency of the filters along the transmission line. Because of the nonlinear nature of the soliton, its central frequency can follow the shift imposed by the filters so that the soliton is moved toward a region where the noise has been previously attenuated. It finally allows the creation of an optical line that is opaque to noise but transparent for solitons.

In the next section, we present an analysis of the effect of sliding filters on the optical phase jitter of soliton pulses in single-channel constant-dispersion links. An analytical expression for the phase standard deviation is derived by use of the soliton perturbation theory. This result is validated by comparison with Monte Carlo simulations.

### 3.3.1 Perturbation theory applied to sliding-frequency guiding filters

The propagation of optical pulses in a sliding-filtered constant-dispersion amplified link is described by the perturbed nonlinear Schrödinger equation:

$$i\partial_z u + \frac{1}{2}\partial_{tt}^2 u + |u|^2 u = \epsilon P(u)\,, \tag{115}$$

where $P$ represents the perturbation and includes both the sliding filters and ASE noise, $\epsilon$ is a small parameter, and a standard normalization of the NLSE has been used. Properly chosen transformation and a uniformly accelerated frame [97] allow us to write the perturbation resulting from sliding-frequency filters as

$$\epsilon P = i[\delta u + (3/4)k_f \partial_{tt}^2 u] - \omega_f' t u\,, \tag{116}$$

where $\delta$ is the excess gain required to overcome the loss imposed on the solitons by the filters, $k_f$ is the filter strength, and $\omega'_f$ is the sliding rate. Unless otherwise indicated, notations of reference [97] are used throughout the derivation. The soliton solution of the non-perturbed NLSE is given by

$$u_s(t) = A\text{sech}[A(t-\alpha)]\exp(i\phi - i\omega t)\,, \tag{117}$$

where $A$ is the amplitude, $\alpha$ the temporal position, $\omega$ the angular frequency, and $\phi$ the phase of the soliton. Each amplifier imparts a zero-mean random shift to the soliton parameters, with variances given by [97]

$$\langle \delta A^2 \rangle = A\,\epsilon_n\, n_{sp}\, F(G) \tag{118}$$

$$\langle \delta \omega^2 \rangle = \frac{A}{3}\,\epsilon_n\, n_{sp}\, F(G) \tag{119}$$

$$\langle \delta \alpha^2 \rangle = \frac{\pi^2}{12A}\,\epsilon_n\, n_{sp}\, F(G) \tag{120}$$

$$\langle \delta \phi^2 \rangle = \frac{1}{3A}\left(\frac{\pi^2}{12}+1\right)\epsilon_n\, n_{sp}\, F(G)\,, \tag{121}$$

where $\epsilon_n$ is the ratio of the photon energy to the unit energy (in soliton units), $n_{sp}$ is the spontaneous emission factor, $G$ is the gain of the amplifier, and $F(G) = (G-1)^2/[G\ln(G)]$ is the ratio of the soliton peak power at the amplifier output to the peak power of the average soliton. The perturbation theory can be used to calculate the evolution of the soliton parameters as a function of distance [97]. The filters guide the amplitude and frequency to a fixed point given by $A = 1$ and $\omega = -\omega'_f/k_f = \Delta$. The evolution of small variations around this fixed point $A = 1 + a$ and $\omega = \Delta + d$ are given by

$$\begin{bmatrix} a(z) \\ d(z) \end{bmatrix} = \begin{bmatrix} t_1 + t_2 & \sqrt{3/2}(t_1 - t_2) \\ \sqrt{2/3}(t_1 - t_2) & t_1 + t_2 \end{bmatrix} \begin{bmatrix} a_0 \\ d_0 \end{bmatrix}, \tag{122}$$

where $\gamma_i = k_f(1 \pm |\Delta|\sqrt{6})$, $t_i(z) = \exp(-\gamma_i z)$, and $a_0$ and $d_0$ are initial values of the amplitude and frequency. The magnitude of the parameter $\Delta$ must be less than $1/\sqrt{6}$ to ensure stable

propagation of the pulses. For a given filter strength, this condition fixes an upper limit for the sliding rate.

To calculate the phase jitter, we change the referential and shift the fixed-point frequency to zero. The evolution of the temporal position and phase is given by

$$\begin{cases} \alpha'_z &= -d & (123) \\ \\ \phi'_z &= a + \omega'_f \alpha & (124) \end{cases}$$

All parameters have an influence on the evolution of the phase. Since the amplitude and frequency are coupled by the sliding filters, they both intervene in the first term on the right-hand side of equation (123). The temporal position modifies the phase jitter through the second term of this equation. At a given distance $z$, we can calculate the contribution of each amplifier to the phase by using the initial values given by equations (118)–(121) and the parameter evolution equations (123)–(124). Adding up all these contributions, taking the variance, approximating the discrete sum over the amplifiers by a continuous integral, and for distances such that $\gamma_2 z \gg 1$, we obtain the following expression for the phase variance:

$$\langle \delta\phi^2(z) \rangle = \frac{\epsilon_n n_{sp} F(G) z}{3 z_A} \left[ A_1 z + A_2 z^2 + A_3 z^3 \right] , \tag{125}$$

with

$$\begin{aligned} A_1 &= 3a_1^2 + 3a_2^2 + 6a_1 a_2 + b_1^2 + b_2^2 + 2b_1 b_2 + 1 + \pi^2/12 \\ A_2 &= 3a_1 a_3 + 3a_2 a_3 + b_1 b_3 + b_2 b_3 \\ A_3 &= a_3^2 + b_3^2/3 + \pi^2 w_f'^2/12 , \end{aligned} \tag{126}$$

and

$$\begin{aligned} a_1 &= \frac{1}{\gamma_1}\left(\frac{1}{2} + \sqrt{\frac{1}{6}}\frac{\omega'_f}{\gamma_1}\right) \quad b_1 = \frac{1}{\gamma_1}\left(\sqrt{\frac{3}{8}} + \frac{\omega'_f}{2\gamma_1}\right) \\ a_2 &= \frac{1}{\gamma_2}\left(\frac{1}{2} - \sqrt{\frac{1}{6}}\frac{\omega'_f}{\gamma_2}\right) \quad b_2 = \frac{1}{\gamma_2}\left(-\sqrt{\frac{3}{8}} + \frac{\omega'_f}{2\gamma_2}\right) \\ a_3 &= \sqrt{\frac{1}{6}}\omega'_f\left(\frac{1}{\gamma_2} - \frac{1}{\gamma_1}\right) \quad b_3 = -\frac{\omega'_f}{2}\left(\frac{1}{\gamma_2} + \frac{1}{\gamma_1}\right) . \end{aligned} \tag{127}$$

The coupling between the frequency and the amplitude of the pulse resulting from the sliding filters reintroduces a $z^3$ dependence of the phase variance. When $\omega'_f = 0$, the terms

$A_2$ and $A_3$ are reduced to zero, and $A_1 = 3/k_f^2 + 1 + \pi^2/12$, so that we recover the result derived in reference [12] for fixed-frequency filters. Equations (125)–(127) are the main result of this section. As for timing jitter, sliding the central frequency of the in-line filters induces a penalty on the phase fluctuations. Therefore, for a given filter strength $k_f$, there is a trade-off between the reduction of the continuum and the growth of the phase jitter, which both occur when the sliding rate is increased. It should be noted that equation (125) does not apply when the continuum is strong because the perturbation theory does not take into account interactions between the soliton and the radiative background. To investigate the suppression of continuum, we now confront the analytical result with simulations.

Statistical simulations based on the split-step Fourier method were performed to calculate the phase jitter as a function of distance in a soliton channel. The numerical parameters of the system are given by Table 11. Gaussian filters were placed after each amplifier.

**Table 11. Numerical values of the system parameters.**

| | |
|---|---|
| Pulse shape | $\text{sech}^2$ |
| FWHM Pulsewidth (ps) | 10 |
| DSF Fiber dispersion (ps/nm.km) | 0.25 |
| Fiber length (km) | 45 |
| Fiber effective area ($\mu$m$^2$) | 50 |
| Spontaneous emission factor | 1.5 |

Figure 46 is a plot of the theoretical and numerically obtained phase standard deviation as a function of distance in two systems with no sliding and filter bandwidths of 140 GHz ($k_f = 0.16$) and 100 GHz ($k_f = 0.33$). We observe that the growth of the continuum causes a large deviation of the numerical curve around 7 Mm for the 140 GHz system and 4.5 Mm for the 100 GHz, and the phase jitter grows very rapidly beyond this point. As expected, the continuum grows more rapidly when the filter bandwidth is smaller because the excess gain is higher.

The standard deviation of the phase is plotted in Figure 47 for the 140 GHz system with sliding rates of 6 GHz/Mm ($\omega_f' = 0.022$, $\Delta = -0.13$) and 12 GHz/Mm ($\omega_f' = 0.043$,

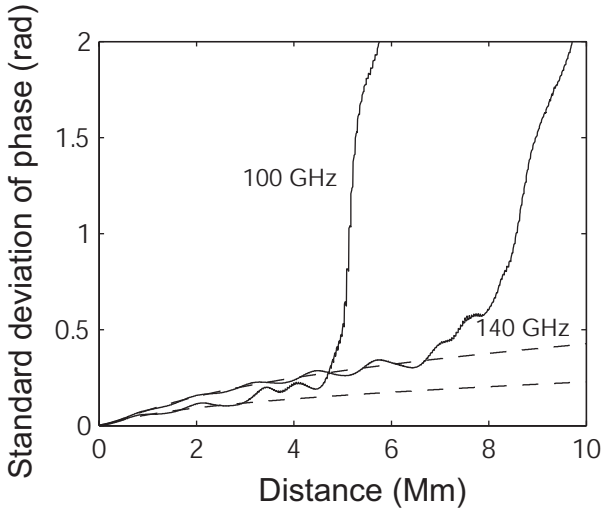


**Figure 46. Standard deviation of the phase as a function of distance for filter bandwidths of 100 GHz and 140 GHz, and no sliding. Solid line: numerical simulation, dashed line: perturbation theory.**

$\Delta = -0.26$). In both systems, the sliding filters efficiently suppress the continuum, and the perturbation theory succeeds in predicting the phase jitter. For the 6 GHz/Mm sliding rate, the term in $z^2$ in equation (125) is predominant for a distances in the Mm range, so that the phase standard deviation operates to grow linearly. When the sliding rate is further increased to 12 GHz/Mm, the term in $z^3$ becomes predominant for the same range of distances, so that the phase jitter is considerably increased by the sliding filters. The 100 GHz system requires a higher sliding rate to suppress the radiative background exponential growth.

Figure 48 is a plot of the phase jitter as a function of distance in this system, with a sliding rate of 9 GHz/Mm ($\omega'_f = 0.032$, $\Delta = -0.10$). This sliding rate allows sufficient suppression of the radiative background noise over 10 Mm. This confirms the fact that narrower filters can be used to further suppress phase jitter.

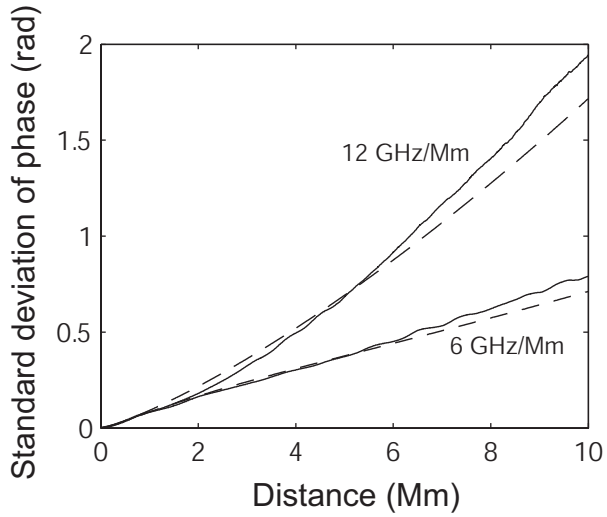


**Figure 47. Standard deviation of the phase as a function of distance for a filter bandwidth of 140 GHz and sliding rates of 6 and 12 GHz/Mm. Solid line: numerical simulation, dashed line: perturbation theory.**

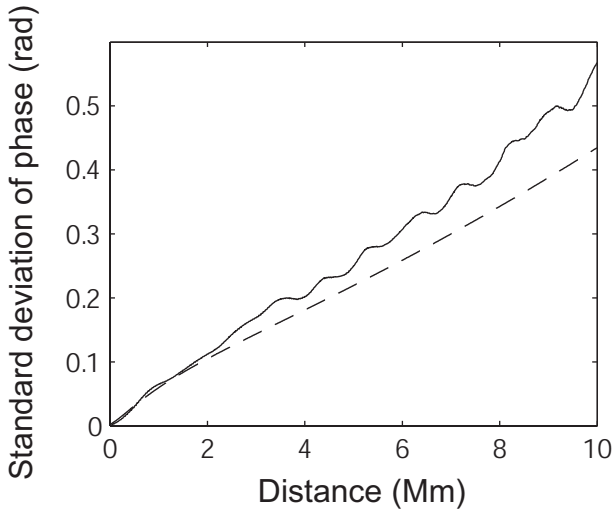


**Figure 48. Standard deviation of the phase as a function of distance for a filter bandwidth of 100 GHz and a sliding rate of 9 GHz/Mm. Solid line: numerical simulation, dashed line: perturbation theory.**

## 3.4 Experimental investigation on phase jitter

### 3.4.1 impact of ASE noise and nonlinearities on a WDM DPSK-based transmission

The theoretical evaluation of phase jitter represents an important step toward a complete analysis of system performances. In this context, we distinguished different phenomena contributing to the total phase jitter. Among them, chromatic dispersion creates a coupling between phase and frequency, which is underlined by the following experimental setup. The cumulative effects of ASE and dispersion deteriorate the transmission performances of a 10 Gbit/s WDM transmission line using a phase modulation. The following measurements were done on a straight line (Figure 49) during an internship in the Lightwave Communication Division (Mitsubishi).

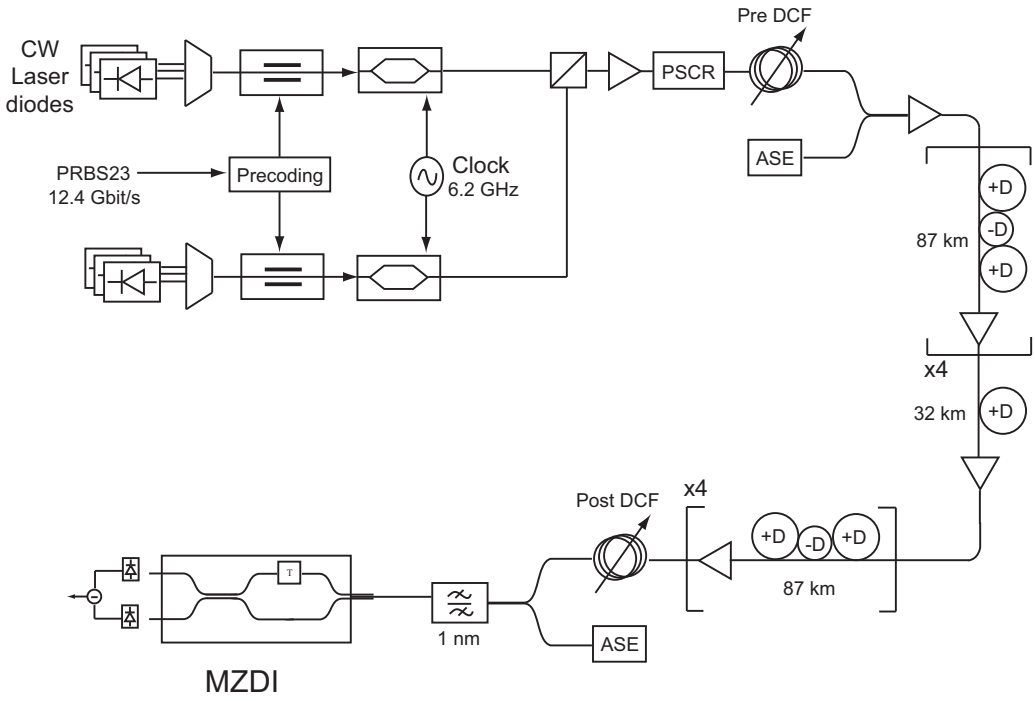


**Figure 49. Experimental setup in CSRZ DPSK configuration.**

The 11 CW laser-diodes were arranged from 1542.94 to 1550.92 nm with a channel spacing of 100 GHz. The even and the odd channels were multiplexed separately, modulated independently, and combined with orthogonal polarization by a polarization beam

combiner to reduce linear and nonlinear crosstalk [104]. The DPSK signals were generated with phase modulators driven by a 12.4 Gb/s precoded data stream (PRBS23). The Mach-Zehnder modulators driven by a 6.2 GHz clock with amplitude $2V_\pi$ performed the pulse carving for CSRZ-DPSK modulation. In the case of NRZ-DPSK, they were replaced by optical attenuators. The polarization scrambler (PSCR) was intentionally inserted to mitigate the BER fluctuations resulting from the polarization-dependent loss/gain and polarization mode dispersion in the loop. An additional source of ASE noise was inserted to adjust OSNR at the transmitter.

The parameters of the transmission line are given in Table 12. After the 728 km propagation, the signal was filtered using 1.0 nm bandwidth filters, decoded by a fiber based 1-bit delay interferometer, and detected by the balanced detector.

Figure 50 shows the Q-factor variations evaluated after BER measurements as a function of the OSNR at the transmitter. For both modulation formats, we changed the number of channels to control the output power. Average powers of 6.1 and 9.5 dBm per channel were respectively obtained with 11 and 5 channels. In this first experiment, the optimal pre-compensation was chosen for both formats ($-160$ ps/nm) and the received OSNRs were set to 15.4 dB for NRZ DPSK and 13.1 dB for RZ DPSK, respectively. In any case, the transmission is corrupted by the increasing level of ASE noise. For 6.1 dBm/ch, there is no obvious difference between NRZ-DPSK and CSRZ-DPSK. Nevertheless, the increase to 9.5 dBm/ch leads to a significant drop in the Q values. This is consistent with our previous simulation results. Since the level of SPM is increased, nonlinear phase jitter becomes dominant.

**Table 12. Transmission line parameters.**

| | |
|---|---|
| FWHM Pulsewidth (ps) | 54 ps |
| Number of WDM channels | 11 (5) |
| Power per channel (dBm/ch) | 6.1 (9.5) |
| Bit rate (Gbit/s) | 12.4 |
| Channel spacing (GHz) | 100 |
| Transmission line (Fibre UltraWave™ Ocean Fiber IDF/SLA) | |
| Fiber 1 and 3 (SLA) | |
| Dispersion (ps/nm.km) | 20 |
| Length (km) | 29 |
| Attenuation (dB/km) | 0.2 |
| Effective area ($\mu m^2$) | 106 |
| Fiber 2 (IDF) | |
| Dispersion (ps/nm.km) | -44.5 |
| Length (km) | 28 |
| Attenuation (dB/km) | 0.23 |
| Effective area ($\mu m^2$) | 29 |
| Amplifier | |
| Gain (dB) | 20 |
| Output power (dBm) | 16.5 |
| Noise figure (dB) | 4 |
| Fibre (SLA) | |
| Dispersion (ps/nm.km) | 20 |
| Length (km) | 32 |
| Attenuation (dB/km) | 0.2 |
| Effective area ($\mu m^2$) | 106 |
| Amplifier | |
| Gain (dB) | 8 |
| Output power (dBm) | 16.5 |
| Noise figure (dB) | 4 |

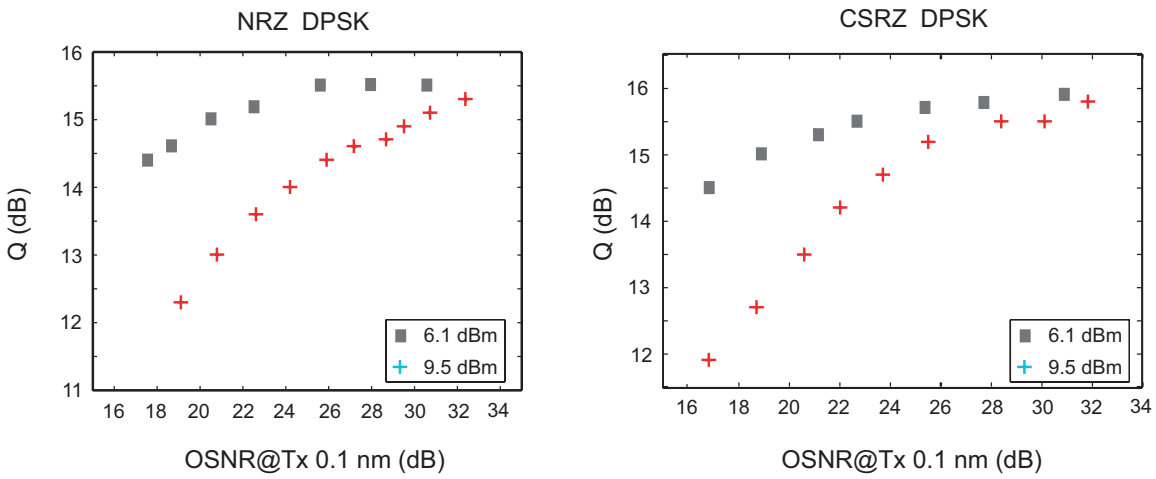


**Figure 50. Q factor as a function of the OSNR at the transmitter for NRZ DPSK and CSRZ DPSK.**

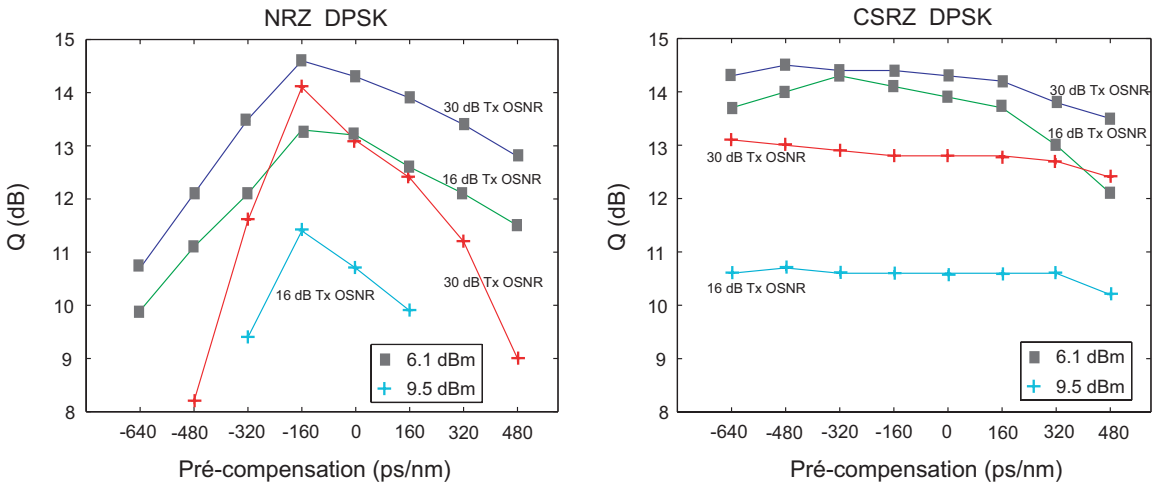


**Figure 51. Q factor as a function of pre-compensation parameter for NRZ DPSK and CSRZ DPSK.**

Another factor acting on the phase jitter evolution is the interaction chirp–chromatic dispersion. It is represented by the term $\beta_2\phi_2$ in equation (69). The combined impairments resulting from SPM and the distortions arising from residual dispersion, also known as the SPM-GVD effect (*Self Phase Modulation-Group Velocity Dispersion*), affect the temporal form of the optical signal. In a second experiment, we underlined this phenomenon by varying the amount of pre-compensation. The post-compensation value was set to fully compensate for the accumulated dispersion. The results (Figure 51) show the influence of Gordon-Mollenauer and SPM-GVD effects on the overall transmission performance. In the case of NRZ DPSK, Q-factor degradation is very fast as soon as the pre-compensation is no longer optimal. The tolerance is even less strong when the average power per channel is increased. NRZ DPSK is therefore very sensitive to distortions resulting from pre-compensation regardless of the OSNR level. In the same conditions, CSRZ DPSK shows a better tolerance on a greater scale of pre-compensation values. All these conclusions can be seen on the different eye diagrams of Figure 52. Each diagram was captured at the fixed OSNR of 28 dB. The timing distortions are due to the SPM-GVD, whereas the power fluctuations are due to the Gordon-Mollenauer effect.

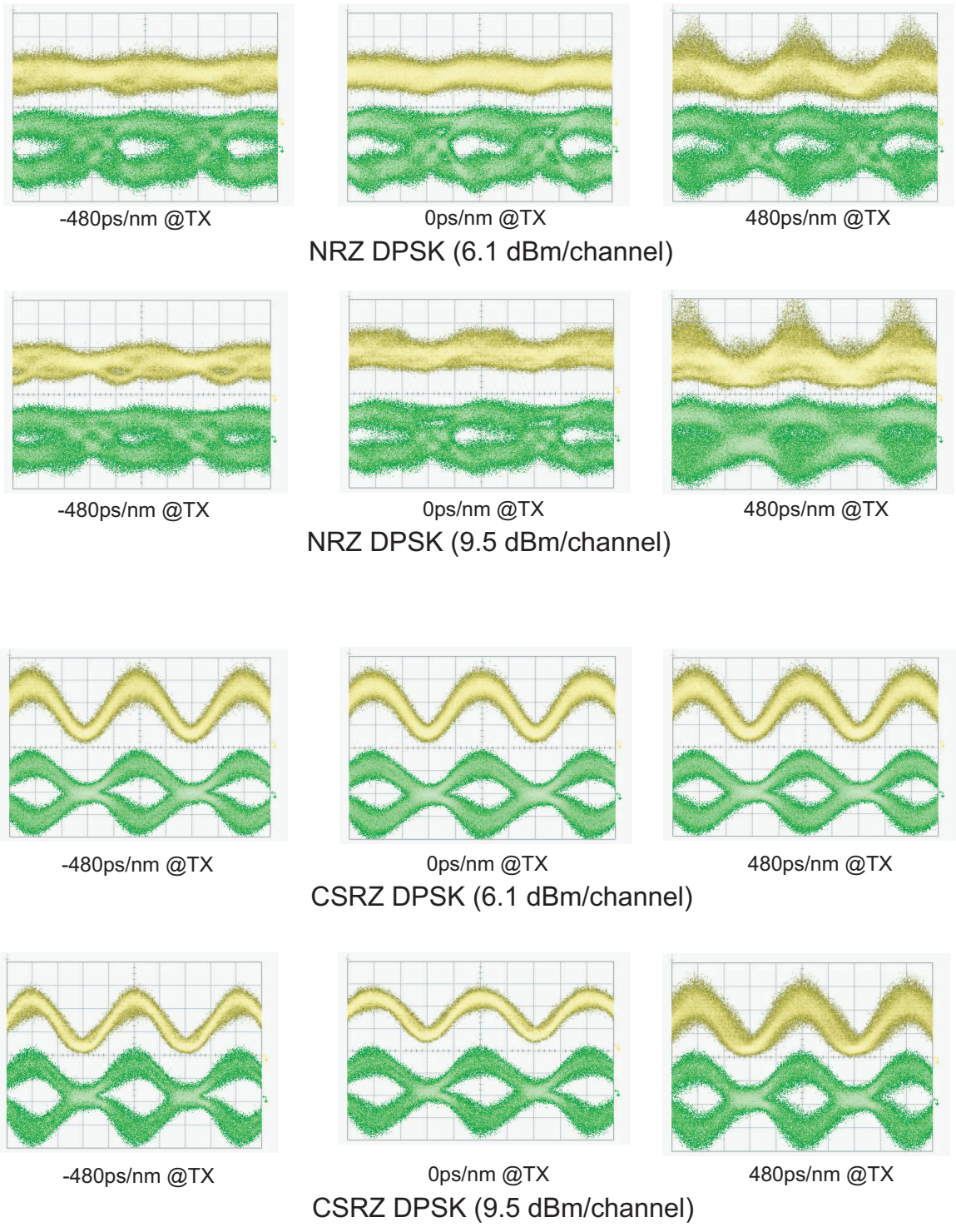


**Figure 52. NRZ and CSRZ DPSK eye diagrams when pre-compensation value is varying for a given average power per channel (**6.1 **and** 9.5 **dBm). The upper traces correspond to an eye taken before demodulation whereas the bottom traces are taken after the balanced detection.**

### 3.4.2 Experimental measurement of optical phase jitter in RZ-DPSK systems

Theoretical [87, 105] as well as experimental [11] studies have investigated the probability density of nonlinear phase noise and its impact on the degradation of phase-modulated systems. Although it is now known that the Gaussian noise assumption fails in predicting balanced receiver performance, its use is still reasonably accurate for single-ended detection [106]. Based on this assumption, a differential phase Q factor has been defined [107]

$$Q_{\Delta\phi} = \frac{\pi}{\sigma_{\Delta\phi,0} + \sigma_{\Delta\phi,\pi}}, \tag{128}$$

where $\sigma_{\Delta\phi,0}$ and $\sigma_{\Delta\phi,\pi}$ represent the standard deviations of the differential phase on the 0 and $\pi$ rails, respectively. The differential phase is the phase difference between two sampling points separated by one bit period mapped to the range $-\frac{\pi}{2}$ to $\frac{3\pi}{2}$. In Figure 53, the center of the bit slot is located at 50 ps (or 150 ps) and the divergence of the differential phase at 100 ps is due to the fact that the intensity of the light signal is nearly zero.

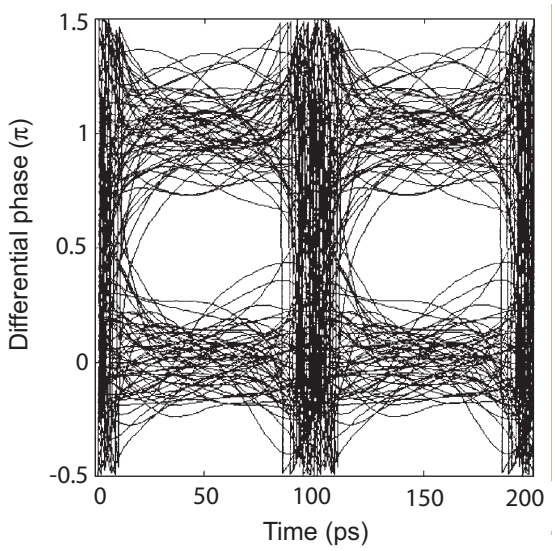


**Figure 53. Differential phase eye diagram.**

The phase Q factor was later adapted [108] to predict the BER more accurately. This

method essentially addresses the impossibility of error counting in simulations and proposes a useful BER estimate by evaluating the statistical fluctuations of the received signal. If the key parameters, i.e. the standard deviations of the differential phase on 0 and $\pi$ rails, are easily evaluated in simulations, their experimental evaluation is far from being straightforward. [109] is the only experimental investigation that proposes an evaluation of the soliton phase stability through its standard deviation measurement. Nevertheless, the proposed scheme is too specific to the modulation format used and cannot be adapted to evaluate the performances of standard DPSK-based communications.

In this paragraph, we propose and investigate a novel experimental method which provides an estimate of the optical phase variance of RZ-DPSK systems. The means and variances of the power detected before and after DPSK demodulation are the only physical parameters needed to determine the optical phase variance. This can be easily measured with the histogram function of a fast oscilloscope.

#### *3.4.2.1 Principle*

The basic principle of the phase jitter measurement is as follows.

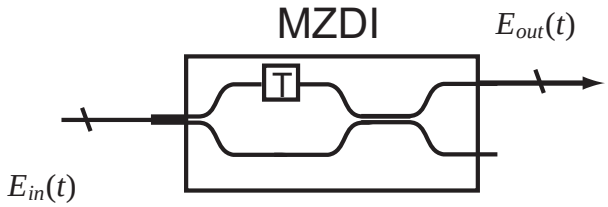


**Figure 54. DPSK demodulator.**

After propagation in the transmission line, the electric field can be written as

$$E_{in}(t) = (a(t) + n(t)).\, e^{j(\phi(t)+\delta\phi(t))}\,, \tag{129}$$

where $a(t).e^{j\phi(t)}$ is the pulse waveform with peak power $P_0$ and corrupted by independent amplitude noise $n(t)$ and phase noise $\delta\phi$.

In our model, $n(t)$ is considered a zero-mean Gaussian random variable with variance $\sigma_N^2$. The phase noise $\delta\phi(t)$ results from the direct contribution of ASE accumulated during the propagation and the nonlinear phase noise mediated by the self-phase modulation (SPM) effect. Our model assumes that the successive phase shifts $\delta\phi(t)$ and $\delta\phi(t-T)$ are independent Gaussian zero-mean random variables with variances $\sigma_\phi^2$.

In general, $\delta\phi(t)$ and $n(t)$ are correlated, however for simplicity, we will assume they are independent. This simplified model is justified *a posteriori* by our simulation results. The data bits encoded on the differential phase $\Delta\phi(t) = \phi(t) - \phi(t-T)$ are retrieved by using a Mach-Zehnder delay interferometer (MZDI). The MZDI shown in Figure 54 performs the interference between two successive bits so that the electrical field at one of the two output ports is

$$E_{out}(t) = \frac{1}{2}\left(E_{in}(t) + E_{in}(t-T)\right) \ . \tag{130}$$

The expected value of the detected power is

$$E[|E_{out}(t)|^2] = \frac{1}{2}\sigma_N^2 + \frac{1}{4}\left(a(t)^2 + a(t-T)^2\right) + \frac{1}{2}\,a(t)\,a(t-T).E\left[\cos\left(\Delta\phi(t) + \Delta\delta\phi(t)\right)\right] \ , \tag{131}$$

where $E[.]$ stands for the expectation value. When the interference is constructive, i.e. $\Delta\phi(t) = 0$, the mean and variance of the detected power at peak intensity are given by

$$\begin{cases} E[|E_{out}^{max}(t)|^2|\Delta\phi(t)=0] &= \dfrac{1}{2}[\sigma_N^2 + P_0.(1+e^{-\sigma_\phi^2})] & (132) \\ \sigma^2_{|E_{out}^{max}(t)|^2|\Delta\phi(t)=0} &= \dfrac{1}{16}[6\sigma_N^4 + 12\sigma_N^2 P_0 + 2P_0^2] + \dfrac{1}{8}(P_0^2 + \sigma_N^4 + 2\sigma_N^2 P_0).\,e^{-4\sigma_\phi^2} \\ & \quad -\dfrac{1}{4}P_0^2.\,e^{-2\sigma_\phi^2} + \sigma_N^2 P_0.\,e^{-\sigma_\phi^2}. & (133) \end{cases}$$

Likewise before demodulation:

$$\begin{cases} E[|E_{in}^{max}|^2] &= P_0 + \sigma_N^2 = m \ , & (134) \\ \sigma^2_{|E_{in}^{max}|^2} &= 4P_0\sigma_N^2 + 2\sigma_N^4 = v \ . & (135) \end{cases}$$

Solving this system of equations yields:

$$P_0 = \sqrt{m^2 - \frac{v}{2}}\,, \tag{136}$$

$$\sigma_N^2 = m - \sqrt{m^2 - \frac{v}{2}}\,. \tag{137}$$

Finally, one obtains

$$\boldsymbol{\sigma^2_{|E_{out}^{max}(t)|^2|\Delta\phi(t)=0} = f(m,v) + 2m^2\, e^{-4\sigma_\phi^2} + g(m,v)\, e^{-2\sigma_\phi^2} + h(m,v)\, e^{-\sigma_\phi^2}}\,, \tag{138}$$

where

$$f(m,v) = \frac{1}{8}(v + m^2) \tag{139}$$

$$g(m,v) = -\frac{1}{8}(2m^2 - v) \tag{140}$$

$$h(m,v) = m\sqrt{(m^2 - \frac{v}{2})} - m^2 + \frac{v}{2}\,. \tag{141}$$

Equation (138) relates the variance of the power measured at the peak of a constructive interference ($\sigma^2_{|E_{out}^{max}(t)|^2|\Delta\phi(t)=0}$) to the mean $m$ and variance $v$ of the peak power before demodulation, and the phase variance $\sigma_\phi^2$. The estimation only relies on a measurement of these physical parameters through the histogram function of an oscilloscope and the numerical resolution of (138).

#### *3.4.2.2 Experimental results*

The experimental setup used to investigate the proposed phase jitter estimation method is shown in Figure 55. The output of a 1550 nm CW laser source feeds a phase modulator driven at 10 Gb/s by a pseudo random bit stream (PRBS $2^7 - 1$). The Mach-Zehnder modulator driven by a 10 GHz clock with an amplitude $V_\pi$ performs the pulse carving for RZ-DPSK modulation.

In order to observe nonlinear effects, we intentionally add ASE noise to the RZ-DPSK signal at the transmitter. The noise generation scheme consists of a variable attenuator followed by an optical amplifier and an optical bandpass filter. This allows for the adjustment

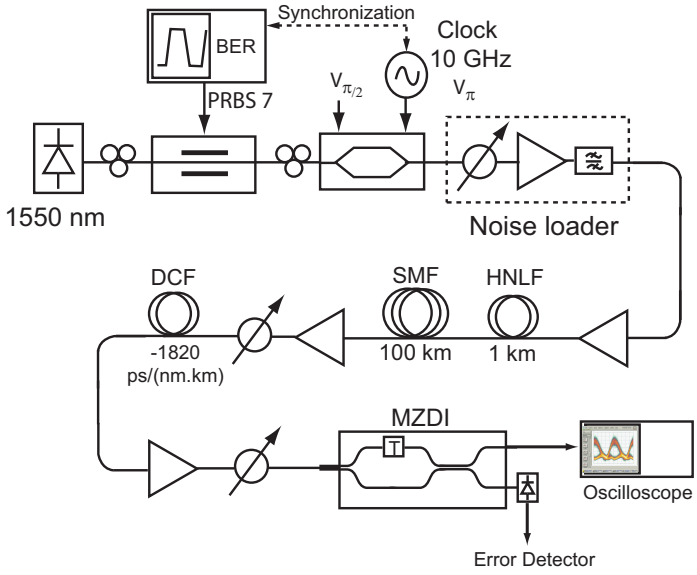


**Figure 55. Experimental setup.**

of the OSNR before transmission. The transmission line consists of a 100 km span of SMF preceded by a 1 km span of highly nonlinear fiber (HNLF) with a nonlinear coefficient $\gamma = 10\ W^{-1}.km^{-1}$ to enhance the SPM effect.

Dispersion is compensated by a dispersion compensating fiber (DCF) module with 1820 $ps/(nm)$. The signal is preamplified before being demodulated. One output port of the MZDI is connected to the oscilloscope to perform the histogram measurements while the other one is used for BER measurement. In order to enhance the Gordon-Mollenauer effect, high input powers were used. The input powers into the HNLF and DCF were 16.5 and 2.45 dBm respectively. The optical bandwidth of the oscilloscope for the histogram measurement was 50 GHz.

Figure 56 shows the eye diagrams observed before and after demodulation for various noise loader attenuations. The process used to estimate the phase jitter is represented in the case of a 28 dB attenuation. As indicated, all the histograms are measured in a 20 $ps$ timing window at the peak power of the eye diagram before and after demodulation. The received peak power prior demodulation is appropriately attenuated to the value of 8 mW so that the detection noise remains negligible compared to the amplitude and phase noise

we want to characterize.

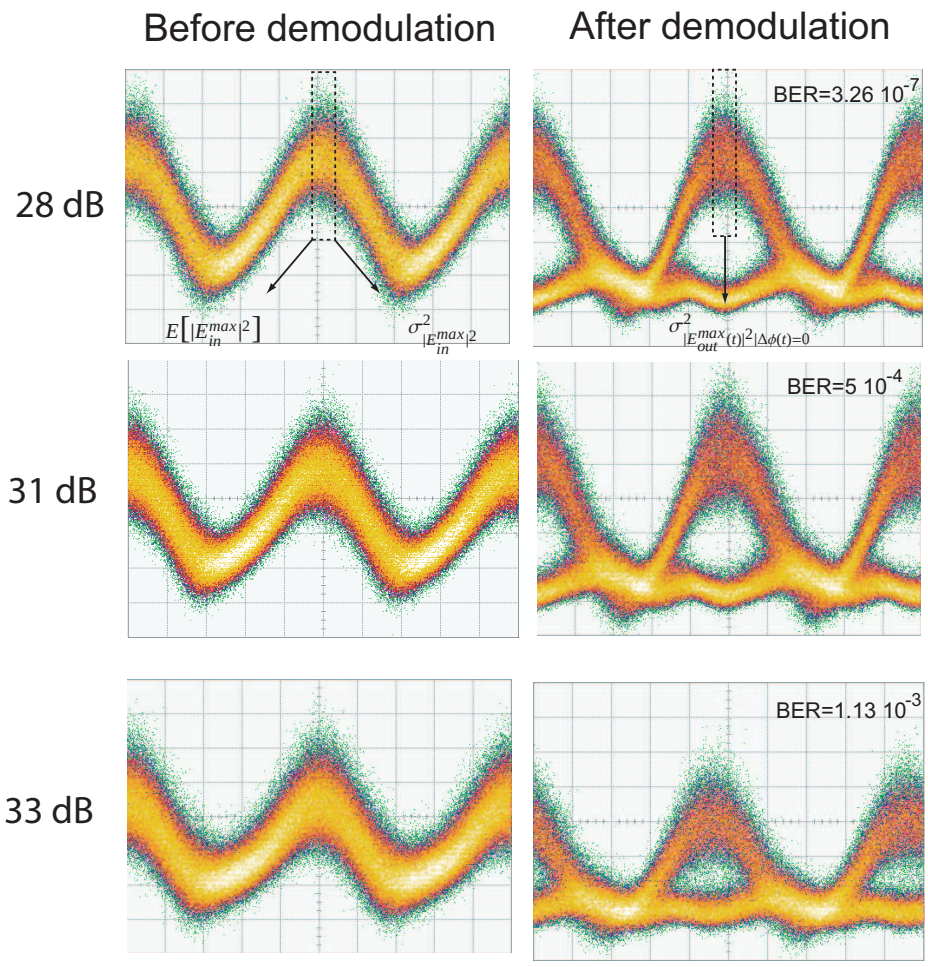


**Figure 56. Eye diagrams observed before and after demodulation for various attenuations.**

The histogram measurements provide the numerical values for the physical parameters $(m, v)$ and $\sigma^2_{|E_{out}^{max}(t)|^2|\Delta\phi(t)=0}$, respectively before and after demodulation. The estimation accuracy for $\sigma^2_\phi$ therefore relies on the model presented in section I. The key device, i.e. the MZDI, was so far considered as perfect, however in practice, the non negligible insertion loss ($X_{\text{Loss}} \simeq 3.14$ dB) introduces a deterministic multiplicative factor in the relation between the input/output optical fields. Equation (138) is modified to take the losses into

account and solved numerically

$$10^{\frac{X_{Loss}}{5}}\,\sigma^2_{|E^{max}_{out}(t)|^2|\Delta\phi(t)=0} = f(m,v) + 2m^2\,e^{-4\sigma^2_\phi} + g(m,v)\,e^{-2\sigma^2_\phi} + h(m,v)\,e^{-\sigma^2_\phi}\,. \quad (142)$$

Figure 57 shows the experimental phase variance as a function of the noise loader attenuation. These measurements are compared with numerical simulations where the phase variances are directly computed from the optical phase evolution of a PRBS $2^7 - 1$ sequence propagating in the setup described in Figure 55. The estimated variance $S^2$ is computed using the best unbiased estimator with 1480 samples. The standard error is then given by $\sigma_{S^2} = S^2\sqrt{2/(N-1)}$, where $N$ is the number of samples used to estimate the variance [110].

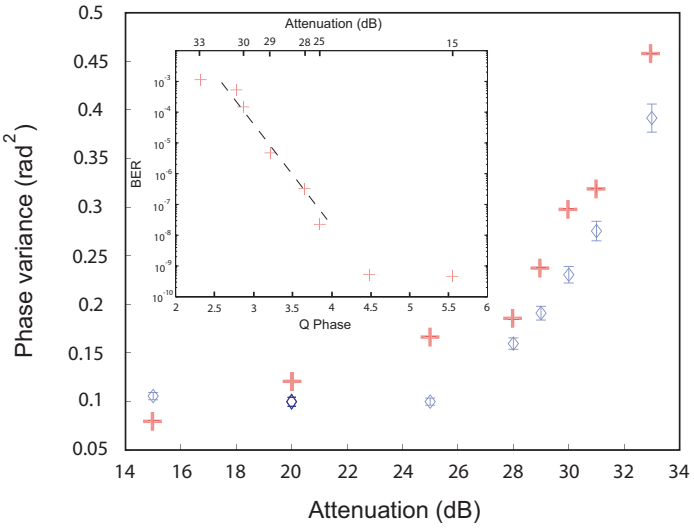


**Figure 57. Phase variance as a function of the noise loader attenuation.**

Figure 57 shows a satisfactory agreement between experimental and simulations results. When the attenuation ranges from 14 to 20 dB, the standard deviation measurements do not change significantly. In fact, as shown in the inset of Figure 57 where the measured BER is plotted as a function of both attenuation and Q phase ($Q_{\text{Phase}} = \pi/2\sigma_\phi$), the measured BER in this range is inferior to $10^{-9}$. The amount of phase noise is then gradually increased and measured for BER ranging from $2.41\,10^{-8}$ to $1.13\,10^{-3}$.

In this chapter, we essentially focused on one of the main limitations of phase-modulated systems: the optical phase jitter. Theoretical as well as experimental results show how the phase noise affects the performances of any transmission. On that occasion, we noticed that modulation formats do not have the same tolerance to both chromatic dispersion and nonlinearities. That is why we propose and further characterize an original format based on duobinary phase modulation.

# CHAPTER 4

# DUOBINARY DPSK MODULATION

The design of new optical communication systems integrates the latest technical innovations. Although the slightest available margin is used to improve the quality of the transmission, one can note that the performances are reaching a certain floor. Regarding the maturity of the RF communications, it seems that optical communications are at an early stage of development which can benefit from the ideas and know-how accumulated in RF. How not to be stuck by the complexity and the efficiency of the codes (40 bit/s/Hz) when commercially available optical systems only use intensity modulation in its simplest forms? That is why researchers have intensely worked on modulation formats able to be future updates for optical communication systems. This last chapter will be put in this context since we present the first implementation of a partial response optical continuous phase-modulated (CPM) system based on a duobinary phase response. The principle of the resulting format called duobinary-DPSK will be investigated both theoretically and experimentally.

## 4.1 Duobinary signal

The purpose of this first paragraph is to present duobinary signals in a digital communication context to better understand the benefits of their use.

### 4.1.1 Origin

#### *4.1.1.1 Symbols interference*

A general model for baseband communication systems is represented on Figure 58.

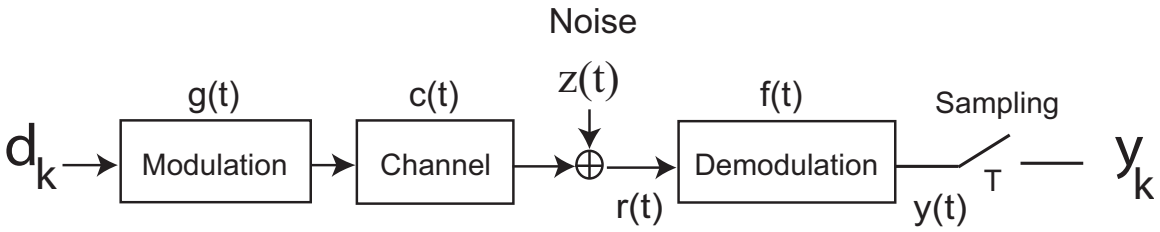


**Figure 58. General scheme of a digital communication system.** $g(t)$**,** $f(t)$**, and** $c(t)$ **are the impulse responses of the modulation/demodulation filters and the channel.**

The digital data sequence is modulated before its propagation in the channel, demodulated and finally detected. After sampling, the sequence is subject to a threshold which produces a result that has to be as close as the original data as possible. During the propagation, the signal experiences deterministic distortions as well as stochastic ones (noise generated by amplifiers and other electrical components). Using the classical theory of digital communications [111], modulation and transmission channel are modeled by filters with impulse responses $g(t)$ and $c(t)$. Noise $z(t)$ is the realization of a random process on which we have to make some assumptions. It will be considered as stationary additive white Gaussian noise (AWGN) with power spectral density $\sigma_0^2$. At the channel output, we have

$$r(t) = \sum_{k=0}^{+\infty} d_k\, h(t - kT) + z(t) \text{ with } h(t) = g * c(t), \tag{143}$$

where $*$ is the convolution operator. The receiver is composed by a demodulation filter with impulse response $f(t)$ to be determined, a sampler with period $T$, and a decision threshold device which gives the value $d_k$ of the transmitted bit at time $kT$. The demodulated signal is given by

$$y(t) = \sum_{k=0}^{+\infty} d_k\, h * f(t - kT) + z * f(t) = \sum_{k=0}^{+\infty} d_k\, x(t - kT) + \nu(t)\ . \tag{144}$$

So at time $kT$, we can write

$$y_k = y(kT) = \sum_{n=0}^{+\infty} d_n\, x_{k-n} + \nu_k = x_0 \left( d_k + \frac{1}{x_0} \sum_{n \geq 0,\ n \neq k} d_n\, x_{k-n} \right) + \nu_k\ . \tag{145}$$

Normalizing the former expression, we obtain the following form which leads to a major problem for the decision device

$$y_k = d_k + \sum_{n\geq 0,\ n\neq k} (d_n\, x_{k-n}) + \nu_k\ . \tag{146}$$

If the second term of the sum called intersymbol interference (ISI) is large — and this is independent of the noise level which is another impairment —, it dramatically disturbs the decision to retrieve $d_k$. The Nyquist criterion gives a condition on $x(t)$ or its spectrum $X(f)$ to cancel this interference:

Time criterion

$$ISI = 0 \Leftrightarrow \sum_{n\geq 0,\ n\neq k} d_n\, x_{k-n} = 0 \Leftrightarrow x(kT) = \begin{cases} 1 & \text{if } k = 0 \\ 0 & \text{if } k \neq 0 \end{cases} \tag{147}$$

Frequency criterion

$$ISI = 0 \Leftrightarrow \sum_{m=-\infty}^{+\infty} X\left(f + \frac{m}{T}\right) = T \tag{148}$$

If the channel has a bandwidth $W$, 3 cases can be distinguished:

- $\frac{1}{T} > 2W$: as $\sum_{m=-\infty}^{+\infty} X\left(f + \frac{m}{T}\right)$ is the periodic spectrum of $X(f)$ without overlapping, The Nyquist criterion cannot be verified and there is no way to avoid ISI.

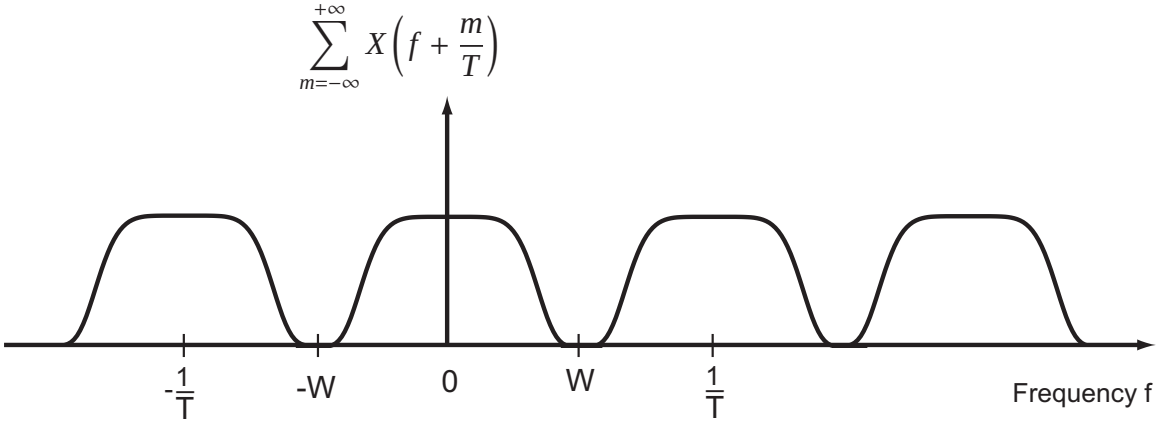


**Figure 59. Representation of B(f) in the case where $f > 2W$.**

- $\frac{1}{T} < 2W$: the periodic spectra overlap and solutions verifying the Nyquist criterion exist such as

$$X(f) = \begin{cases} T & \text{si } 0 \leq |f| \leq \frac{1-\beta}{2T} \\ \frac{T}{2}\{1 + \cos\left[\frac{\pi T}{\beta}\left(|f| - \frac{1-\beta}{2T}\right)\right]\} & \text{si } \frac{1-\beta}{2T} \leq |f| \leq \frac{1+\beta}{2T} \\ 0 & \text{si } |f| > \frac{1+\beta}{2T} \end{cases} \quad (149)$$

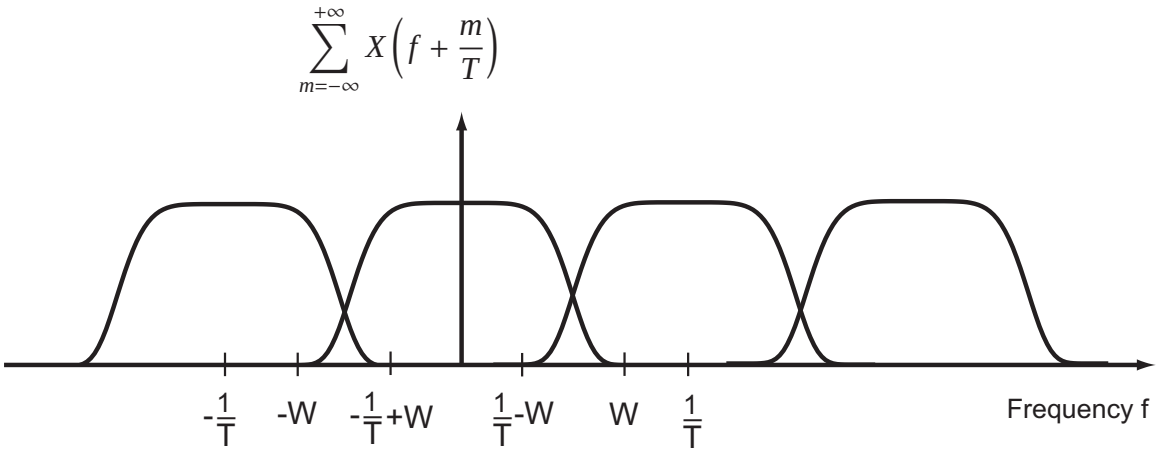


**Figure 60. Representation of B(f) in the case where $f < 2W$.**

- $\frac{1}{T} = 2W$: in this case, there is only one filter verifying the criterion, the one corresponding to a $sinc\left(\frac{\pi t}{T}\right)$ pulse.

All this means that the greatest possible value for $\frac{1}{T}$ to have a transmission without ISI is $2W$. The natural tradeoff that comes in mind for high bit rate transmissions is to allow a controlled amount of ISI. In the time domain, the Nyquist criterion is

$$x(kT) = \begin{cases} 1 & \text{if } k = 0 \\ 0 & \text{if } k \neq 0 \end{cases} \quad (150)$$

Controlling ISI is done by allowing another non zero value for $x(kT)$. We then obtain a class of filters easy to design: duobinary filters. The most used in optical communication systems is

$$x(kT) = \begin{cases} 1 & \text{if } k = 0; 1 \\ 0 & \text{else} \end{cases} \tag{151}$$

The periodic spectrum is not verifying $B(f) = \sum_{m=-\infty}^{+\infty} X\left(f + \frac{m}{T}\right) = T$ anymore but

$$B(f) = \sum_{m=-\infty}^{+\infty} X\left(f + \frac{m}{T}\right) = T \,.\, \left(1 + e^{-j\,2\pi fT}\right) \tag{152}$$

Solving this equation at the Nyquist frequency leads to

$$X(f) = \begin{cases} \frac{1}{W} e^{-j\frac{\pi f}{2W}} \cos\left(\frac{\pi f}{2W}\right) & \text{if } |f| < W \\ \\ 0 & \text{else.} \end{cases} \tag{153}$$

Taking the inverse Fourier transform, we get the shape of the corresponding duobinary pulse (Figure 61)

$$x(t) = sinc\,(2\pi Wt) + sinc\left(2\pi(Wt - \frac{1}{2})\right) \tag{154}$$

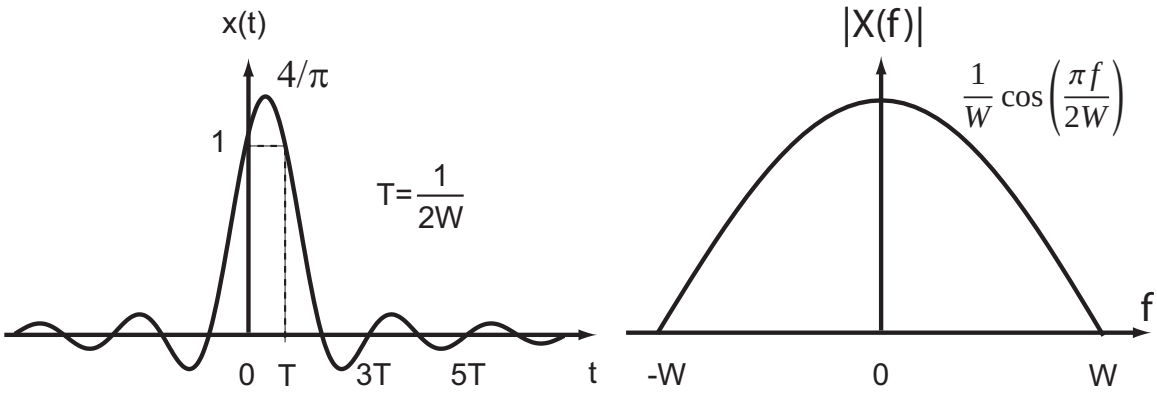


**Figure 61. Duobinary pulse [1,1] and its spectrum.**

If we now suppose that two symbols ’1’ are emitted at time 0 and $T$. Because of the controlled ISI, we will get the superposition of the pulses at the receiver and the resulting main lobe will have an amplitude of ’2’ (Figure 62).

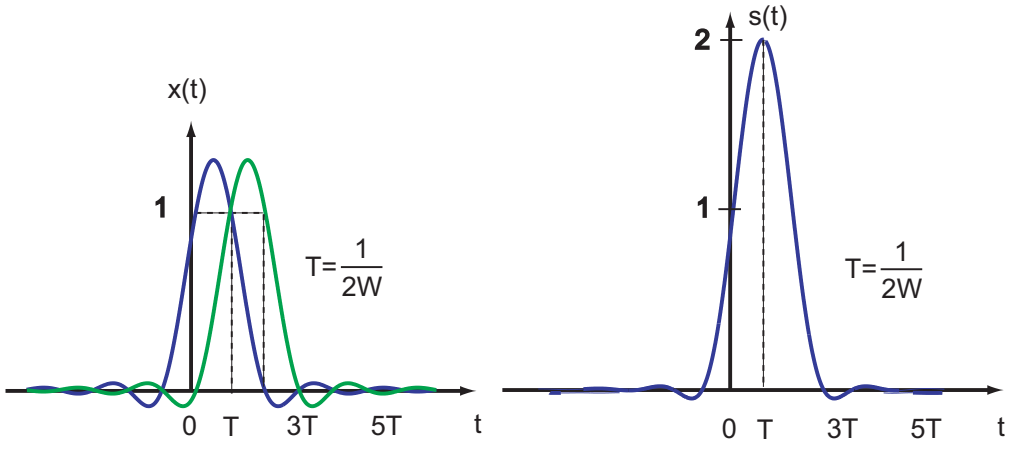


**Figure 62. Pulses generated at time 0 and T with the resulting pulse s(t) at the receiver.**

At the modulator input, we have $y_k = d_k + d_{k-1} + \nu_k$. Without noise, $d_k$ can be retrieved by subtraction at the receiver. To avoid error propagation, a differential precoding is performed at the transmitter. The precoded sequence $p_k$ is obtained according to

$$p_k = d_k \oplus p_{k-1} \text{ with } p_0 = 0\,, \tag{155}$$

where $\oplus$ is the XOR operation. The transmitted sequence $t_k$ is derived from $p_k$.

| | | | | | | | | | | | | |
|---|---|---|---|---|---|---|---|---|---|---|---|---|
| Data $d_k$ | | 1 | 0 | 1 | 1 | 0 | 1 | 0 | 0 | 1 | 0 | 1 |
| Precoding sequence $p_k = d_k \oplus p_{k-1}$ | 0 | 1 | 1 | 0 | 1 | 1 | 0 | 0 | 0 | 1 | 1 | 0 |
| Transmitted data $t_k$ | -1 | 1 | 1 | -1 | 1 | 1 | -1 | -1 | -1 | 1 | 1 | -1 |
| Reveived sequence $B_k = t_k + t_{k-1}$ | | 0 | 2 | 0 | 0 | 2 | 0 | -2 | -2 | 0 | 2 | 0 |

The received sequence $B_k$ is called duobinary since its 3 levels possible amplitudes $-2$, 0 or 2 only code for 2 original levels in the data sequence. It is easy to see how each level 2 or $-2$ is mapped to an initial data 0 and each 0 is mapped to an initial 1. From the received signal at the input of the demodulator, we have

$$d_k = \frac{1}{2} B_k \oplus 1. \tag{156}$$

One can intuitivelly understand the benefits of such a signal. In the case of a (0,1,0) sequence, the (-2,0,2) sequence produced by duobinary coding is globally less abrupt from the filtering point of view. In the Fourier domain, this will give a spectrum with a reduced occupation which is particularly interesting for WDM systems. This is what is studied in the next paragraph.

#### *4.1.1.2 Duobinary spectrum*

The goal of this paragraph is to characterize the advantage of duobinary modulation in the frequency domain. Let

$$x_{duo}(t) = \sum_k d_k \, h(t - kT) \tag{157}$$

be a duobinary signal generated by the filtering of the binary data sequence $(d_k)_k$ with mean $\mu_k$ and autocorrelation function

$$R_{d_k}(m) = \frac{1}{2} E[d_n^* \, d_{n+m}] \, . \tag{158}$$

To estimate the performance of the modulation, we compute the spectrum of the modulated signal

$$x(t) = \mathrm{Re}\left[ x_{duo}(t) \, . \, e^{j2\pi f_0 t} \right] \tag{159}$$

where $f_0(t)$ is the carrier frequency. For a wide sense stationary (WSS) signal, we have to compute the autocorrelation function $R_{x_{duo}}$ of $x_{duo}$ to express its spectrum $S_{x_b}(f)$ by Fourier transform, then deduce the power spectral density $S_x(f)$ of the modulated signal using

$$R_x(\tau) = \frac{1}{2}\mathrm{Re}\left[R_{x_{duo}}(\tau)\,.\,e^{j2\pi f_0\,\tau}\right] \tag{160}$$

$$S_x(f) = \frac{1}{4}S_{x_{duo}}(f - f_0) + \frac{1}{4}S_{x_{duo}}(-f - f_0)\,. \tag{161}$$

Developed in [111], the calculus shows that, if $(d_k)_k$ is WSS, $x_{duo}(t)$ is not because $R_{x_{duo}}(t, s)$ is not function of $(t - s)$. We can understand it: from a physical point of view, we particularize each instant $nT$ for which a new symbol is generated. So this cannot guarantee that $R_{x_{duo}}(t, s)$ is independent of the time origin, a necessary condition for wide sense stationarity. However if all the realizations taken into account in the statistical moment evaluation are synchronized (symbol emitted every $kT$), we can note that $x_{duo}(t)$ is random and has periodic mean and autocorrelation functions

$$\begin{cases} R_{x_{duo}}(t, s) = R_{x_{duo}}(t + T, s + T) \\ \\ E\left[x_{duo}(t)\right] = E\left[x_{duo}(t + T)\right] \end{cases} \tag{162}$$

$x_{duo}(t)$ is cyclostationary or periodic WSS. Its power spectral density is computed from its autocorrelation function $R_{x_{duo}}(t, t + \tau)$ averaged on one period T

$$\hat{R}_{x_{duo}}(\tau) = \frac{1}{T}\int_{-T/2}^{T/2} R_{x_{duo}}(t, t + \tau)\,dt = \frac{1}{T}\sum_{m=-\infty}^{+\infty} R_{d_k}(m)\int_{-\infty}^{+\infty} h^*(t)\,h(t + \tau)\,dt, \tag{163}$$

The Fourier transform of (163) gives the average power spectral density of $x_{duo}(t)$:

$$\hat{S}_{x_{duo}}(f) = \frac{1}{T}\,|H(f)|^2\,S_{d_k}(f) \tag{164}$$

where $S_{d_k}(f)$ is the power spectral density of the binary data sequence. This last relation shows how the spectral characteristics of the duobinary signal depend on the pulse $h$ and the data correlation. For a duobinary filter with impulse response

$$h(t) = \mathrm{sinc}(2\pi W t) + \mathrm{sinc}(2\pi(Wt - \frac{1}{2})) \tag{165}$$

or

$$H(f) = \frac{1}{W} e^{-j\frac{\pi f}{2W}} \cdot \cos(\frac{\pi f}{2W}) \, rect_{[-W;W]} \tag{166}$$

in the frequency domain, we have

$$\hat{S}_{x_{duo}}(f) = 4T\sigma^2 \cos^2(\pi f T) \, , |f| < \frac{1}{2T}. \tag{167}$$

with the assumption of a zero mean white Gaussian noise with spectral density $\sigma^2$ for the data sequence. Under the same conditions, NRZ and RZ modulation give

$$S_{NRZ}(f) = \sigma^2 A^2 T \, \mathrm{sinc}^2(\pi f T) \, , |f| < \frac{1}{2T} \, , \tag{168}$$

$$S_{RZ}(f) = \alpha^2 \sigma^2 A^2 T \, \mathrm{sinc}^2(\alpha \pi f T) \, , |f| < \frac{1}{2T} \, . \tag{169}$$

The different power spectral densities are represented on Figure 63. Duobinary modulation have a spectrum compressed by a factor 2 compared to NRZ modulation which makes it a good candidate for WDM optical communications. In particular, it shows a better dispersion tolerance. Many experiments report significant improvements in dense and long WDM transmissions [112–115].

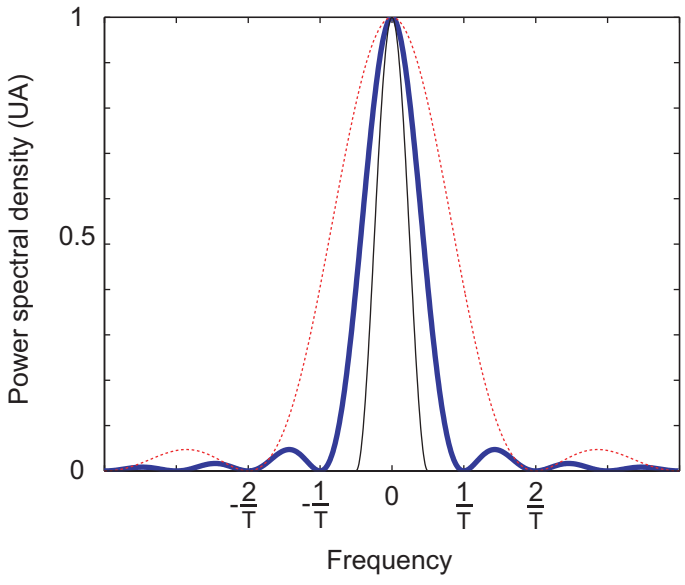


**Figure 63. Power spectral densities of NRZ (bold), RZ (shaded line) and duobinary (solid line) modulations.**

### 4.1.2 Simulations of duobinary filters

In practice, several techniques are available to generate an electrical duobinary signal. If the same precoding step is common to all schemes, different filters can be chosen to approach the cosine shape of the ideal duobinary filter. As it does not show sharp transitions, its fabrication is simple. Figure 64 presents the two methods to produce an electrical duobinary signal, which only differ in the production of the 3 logical levels (0,1,2) since a) uses a coder followed by a lowpass filter with cutoff frequency $B/2$ (Delay and Add Filter for the delay/summation and the filter) whereas b) only uses a tighter filter.

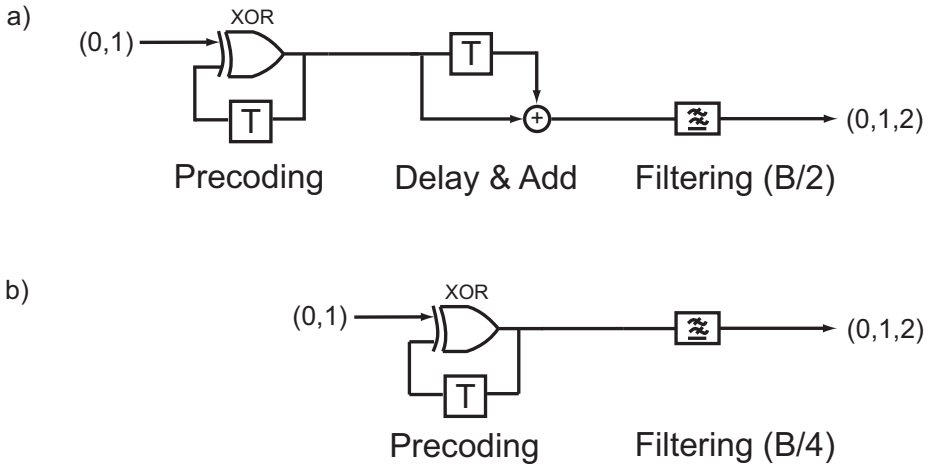


**Figure 64. Techniques used to generate an electrical duobinary signal: a) Delay and Add Filter method, b) Filtering method.**

The simulation results presented on Figure 65 show the influence of the filter on the signal waveform generated from the precoded data sequence. We note that, if at sampling instants the logical level are exactly the same, their evolutions are slightly different. The Bessel filter used in the lab produces larger variations in amplitude than the ideal filter. This is particularly visible for the (1,1) sequence in the $4^{th}$ bit slot. In practice, we will optimize the different parameters to maximize the eye diagram opening.

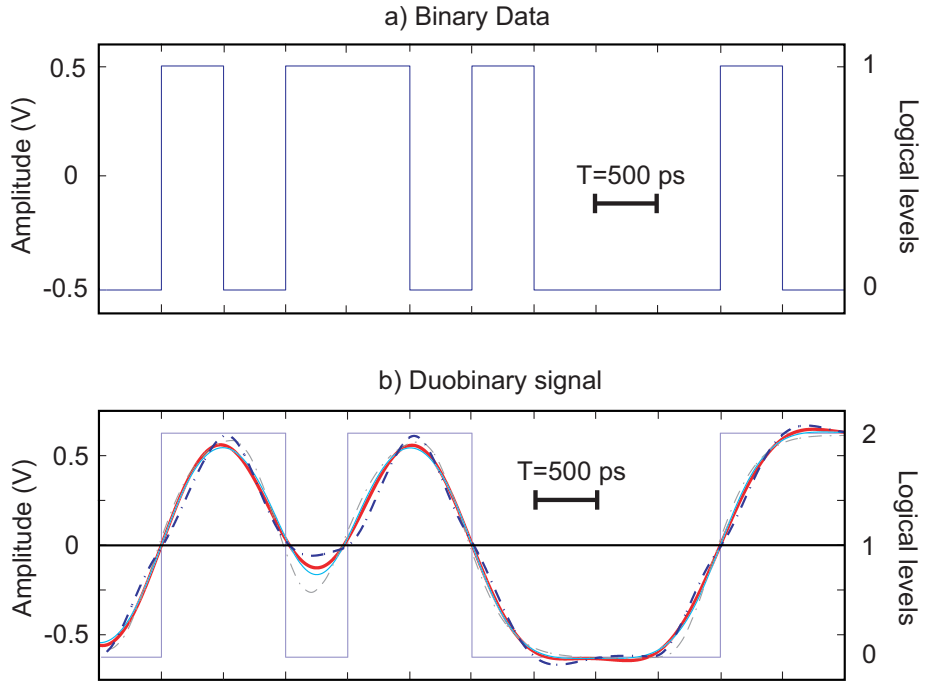


**Figure 65. Ideal filter (bold), Butterworth filter (solid line), ”Delay and add + filter” (dotted bold line), experimental Bessel filter (dotted line).**

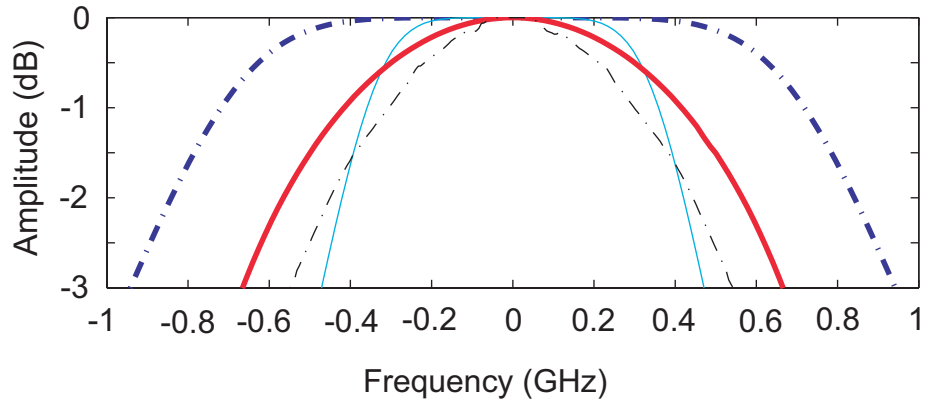


**Figure 66. Amplitude Bode diagram of various duobinary filters. Ideal filter (bold), Butterworth filter (solid line), ”Delay and add + filter” (dotted bold line), Experimental Bessel filter (dotted line).**

## 4.2 Implementation of the Duobinary DPSK modulation

In this section, we propose a modulation format called duobinary DPSK. Its first experimental implementation is done at 2 Gb/s before being performed at 10 Gb/s.

### 4.2.1 Principle

In an intensity modulation context, duobinary modulation was shown to be an attractive candidate. Because of its bandwidth compression (Figure 63), it shows a better dispersion tolerance than its RZ and NRZ counterparts [112]. This advantage could be exploited

- for metropolitan networks with SMF links longer than 40 km without dispersion compensation,
- for long-haul WDM transmissions in which the residual dispersion accumulated by the channel suffering from the dispersion slope is not controlled anymore.

At the same time, as modulation formats that possess a higher spectral efficiency are intensively studied [49, 116], attention focused on phase-modulated formats as promising updates for future optical communication systems [47, 48, 117]. Already developed in the 80's to improve the performances in terms of signal to noise ratio at the receiver, coherent systems — which use the optical phase to convey information — have been discarded by the arrival of optical amplifiers. The pre-amplification performed by an EDFA before the photodetector allowed a sufficient SNR increase. Nevertheless, phase modulation possesses several advantages over intensity modulation in a WDM system: better tolerance to channel nonlinearities and cascaded filtering, and a 3 dB higher sensitivity with balanced detection. However, on-off signalling has always been used in phase-modulated systems resulting in abrupt switchings in the time domain that translate into large spectral side lobes outside of the main spectral band. In the radio-frequency domain, continuous phase-modulated (CPM) systems were shown to overcome these limitations [118]. we present the first implementation of a partial response optical CPM system based on a duobinary phase response.

Table 13 shows a practical example of duobinary DPSK modulation. For DPSK-based modulation, the data stream $s_{data}[k]$ at rate R has to be differentially encoded. This logical XOR operation results in the first precoded sequence

$$p_1[k] = s_{data}[k] \oplus p_1[k-1]\,. \tag{170}$$

The generation of the duobinary signal requires an additional precoding step, which is identical to the first one, yielding the output sequence

$$p_2[k] = p_1[k] \oplus p_2[k-1]\,. \tag{171}$$

This signal is passed through a 5th order Bessel lowpass filter with a 0.28 R cutoff frequency. Binary precoded data $p_2[k]$ are thereby transformed into a 3 level duobinary signal [112]

$$s_{duo}[k] = p_2[k] + p_2[k-1]\,. \tag{172}$$

The operation that converts $p_1[k]$ into $s_{duo}[k]$ has the following one-to-one mapping property: a logical '1' in $p_1[k]$ results in a '1' in $s_{duo}[k]$, while a '0' in $p_1[k]$ results in a '0' or '2' in $s_{duo}[k]$ depending on the memory introduced by the duobinary filtering.

When the phase modulator is driven by a $2V_\pi$ amplitude duobinary signal, the optical phase has continuous variations between 0, $\pi$ and $2\pi$. As in intensity duobinary modulation, logical levels are well defined only at the center of the bit slots, and large oscillations occur between two successive sampling times. Allowing these oscillations is at the origin of the reduced spectral width.

**Table 13. Practical example of duobinary DPSK modulation**

| Data: $s_{\text{data}}[k]$ | | x | x | **1** | **1** | **1** | **0** | **1** | **1** |
|---|---|---|---|---|---|---|---|---|---|
| Differential precoding | | | | | | | | | |
| DPSK | $p_1[k] = s_{\text{data}}[k] \oplus p_1[k-1]$ | | | | | | | | |
| | $p_1[k]$ | x | 0 | 1 | 0 | 1 | 1 | 0 | 1 |
| Duobinary | $p_2[k] = p_1[k] \oplus p_2[k-1]$ | | | | | | | | |
| | $p_2[k]$ | 0 | 0 | 1 | 1 | 0 | 1 | 1 | 0 |
| Modulating duobinary signal | | | | | | | | | |
| $s_{duo}[k] = p_2[k] + p_2[k-1]$ | | | | | | | | | |
| | $s_{duo}[k]$ | 0 | 0 | 1 | 2 | 1 | 1 | 2 | 1 |
| MZDI | | | | | | | | | |
| Constructive port | | | | | | | | | |
| | $s^c_{mzdi}[k]$ | 0 | 1 | 0 | 0 | 0 | 1 | 0 | 0 |
| Destructive port | | | | | | | | | |
| | $s^d_{mzdi}[k]$ | 1 | 0 | **1** | **1** | **1** | **0** | **1** | **1** |

Because photo-detection is phase insensitive, a phase-to-intensity conversion is needed at the receiver. The optical signal is therefore demodulated by a Mach-Zehnder delay interferometer (MZDI) that performs the interference between two successive bits. It is clear that after removing the first two bits of MZDI sequences due to the two precodings, we recover $\overline{s_{data}[k]}$ (resp. $s_{data}[k]$) at the MZDI constructive (resp. destructive) port.

### 4.2.2 Experimental characterization of the duobinary filter

The duobinary filters used in the laboratory experiments are $5^{th}$ order lowpass Bessel filters (Picosecond Pulse Labs) with a 3 dB cutoff frequency of 542 MHz (resp. 2.69 GHz) for a 2 Gb/s (10 Gb/s) bit rate. Their spectral specifications are measured by a network analyser

and presented in Figure 67.

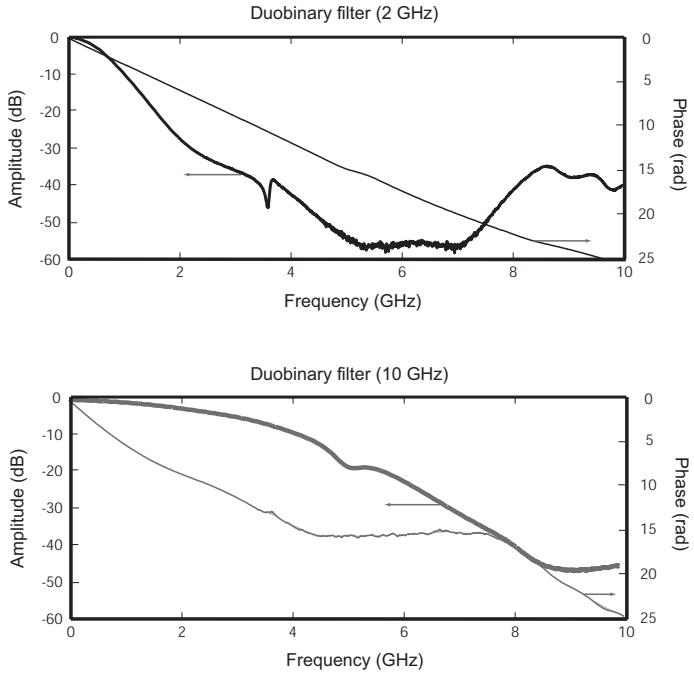


**Figure 67. Bode diagram of duobinary filters at 2 Gb/s and 10 Gb/s.**

#### *4.2.2.1 Experimental setup: 2 Gb/s feasibility with a fiber-based demodulator*

The principle of the duobinary DPSK modulation explained, we now report its first experimental implementation at the bit rate imposed by the bit error rate tester (BERT) (Anritsu MP1632): 2 Gb/s. We will compare it to its NRZ DPSK counterpart to check the trends for the optical spectra obtained by simulations. The experimental setup is depicted in Figure 68. A distributed feedback laser feeds a 10 Gbit/s phase modulator with $V_\pi = 5.8V$. This modulator is driven either directly with a 2 Gbit/s pseudo random bit sequence with amplitude $V_\pi$ for DPSK or with the corresponding duobinary signal with amplitude $2V_\pi$ for duobinary DPSK.

The fiber-based demodulator is made from two couplers put in an isotherm box (Figure 69). In this experiment, the optical phase is controlled by the following parameters

- as in the commercially available 10 Gb/s DPSK demodulator, we stabilize and control

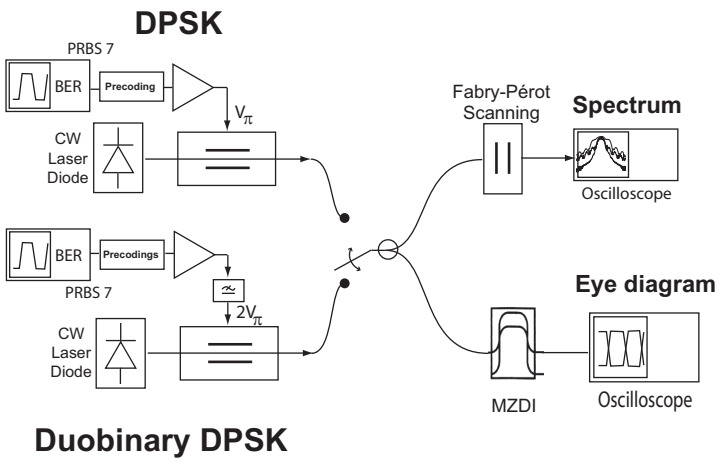


**Figure 68. Experimental setup used to generate NRZ DPSK and duobinary DPSK modulation.**

the temperature of one arm of the MZDI by a Pelletier,

- as soon as the temperature is controlled, we adjust the wavelength of the laser source (Tunics+).

As soon as the interference condition is verified, the system is stable enough to allow some significant measurements. The drift is faster for duobinary DPSK (around 90 mn) than for NRZ DPSK (more than 2 hours).

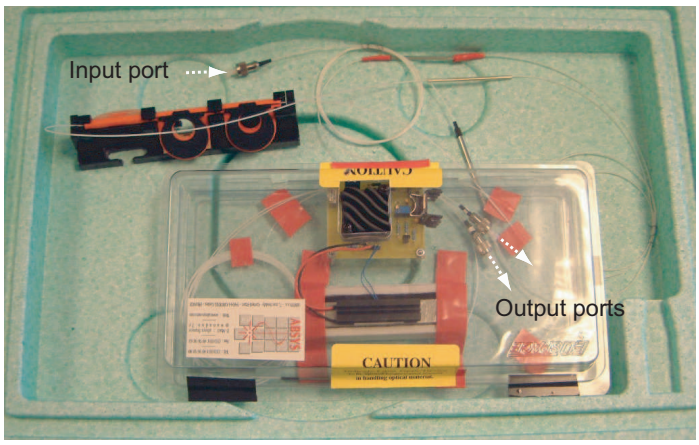


**Figure 69. Fiber-based DPSK demodulator.**

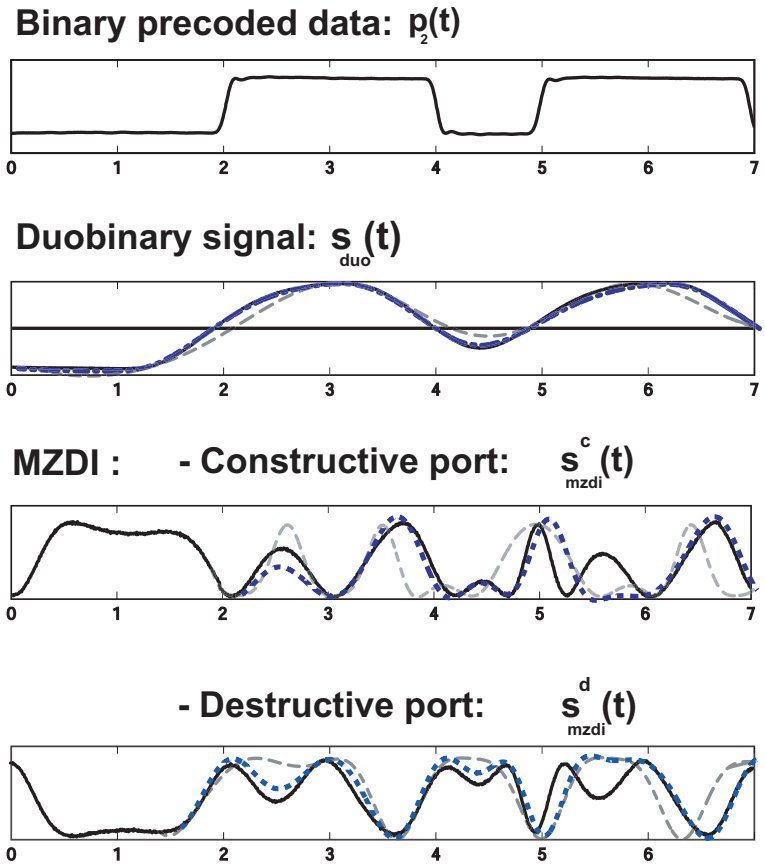


**Figure 70. Experimental signals corresponding to the data sequence of Tab.1: simulations (dashed), experimental results (solid line), simulated experimental filter (dashed bold).**

Figure 70 shows the electrical and optical signals at different points in the system obtained by the data sequence of Table 13. The simulations (dashed and dashed bold lines) are respectively obtained by use of an ideal duobinary filter ($h(\omega) = \cos(\omega T/2)$) and the experimental Bessel filter. They produce a slightly different signal compared to the experimental Bessel filter (solid line). Combined with demodulator imperfections, this explains the mismatch in the waveforms although logical values are equal at sampling times. As in a standard DPSK system, balanced detection can be used to obtain a 3 dB increase in sensitivity.

Figure 71 shows the simulated and measured eye diagrams at the output of the constructive port. The large oscillations between sampling times in the duobinary case are clearly observed. The DPSK eye diagram also shows sharp rises between two successive bit slots. This is easily explained by the use of a finite-bandwidth phase modulator that does not produce perfect $\pi$ phase jumps, as opposed to the intensity modulator technique usually used to generate the optical DPSK signals [117]. The asymmetry in the observed space level is therefore due to imperfections in the experimental setup. Moreover, the simulated eye diagram does not exhibit such an asymmetry.

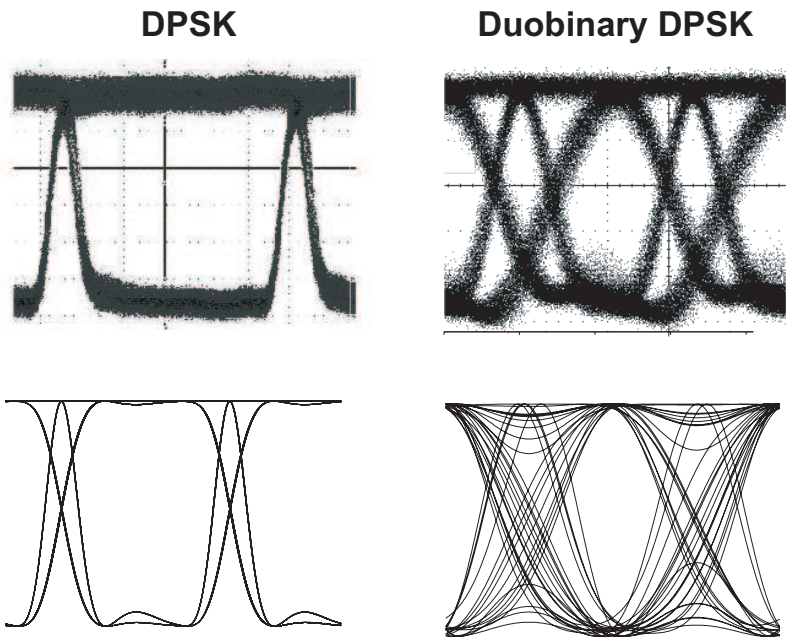


**Figure 71. Simulated and experimental eye diagram of NRZ DPSK and duobinary DPSK at the output of the MZDI constructive port.**

### 4.2.3 Optical spectrum and sensitivity: measures and comparison with NRZ-DPSK

A scanning Fabry-Pérot interferometer is used to measure the spectra of the output signals. Experimental results are presented in Figure 72 with respect to the optical frequency normalized to the transmission bit-rate.

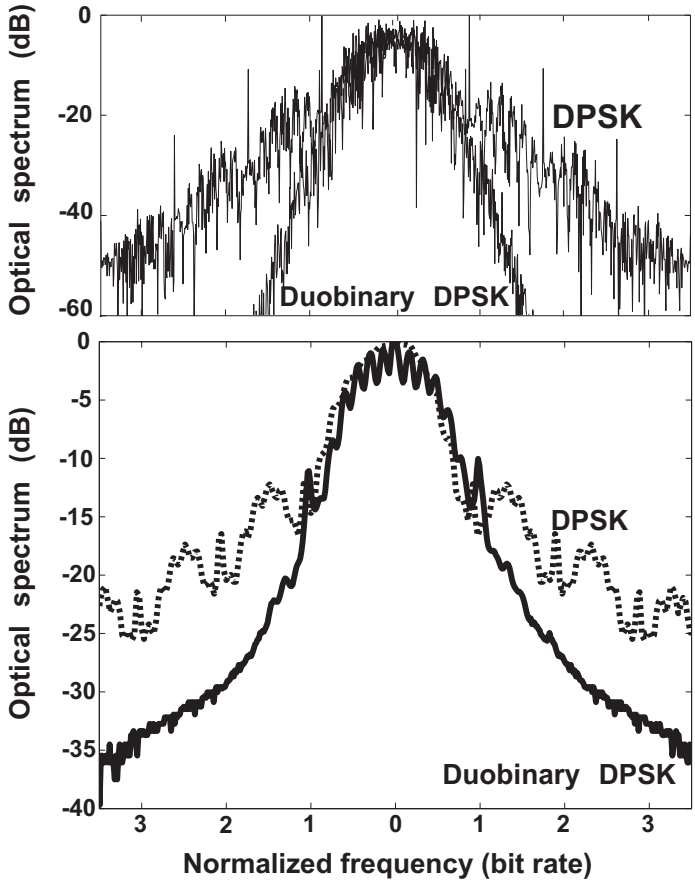


**Figure 72. Simulated and experimental optical spectrum of NRZ DPSK and duobinary DPSK modulation.**

The simulated spectra are computed from a pseudo-random bit sequence (PRBS) of length $2^7 - 1$. The superiority of duobinary DPSK over DPSK modulation in terms of bandwidth requirements is clearly observed. Although the main lobes are of comparable width, the duobinary DPSK spectrum does not exhibit side lobes. We therefore anticipate a better behavior against cascaded optical filtering used in a WDM environment. The spectrum is reduced by a factor of two if we use the 20 dB full width criterion. If no filters are

used, this reduction results in a better tolerance to group-velocity dispersion.

We then measured the sensitivity of the two formats. For this purpose, an optical attenuator was inserted between the emitter and the error detector. A 2.6 GHz electrical lowpass filter was used at the detection. A thermal noise sensitivity degradation of 3.5 dB is observed for duobinary DPSK. This is attributed to the eye opening penalty due to oscillations between sampling times and imperfections in the MZDI and duobinary filter mentioned earlier. In the context of intensity modulation, this penalty was also observed for phase-shaped binary transmission [119] when compared to NRZ and evaluated around 3 dB.

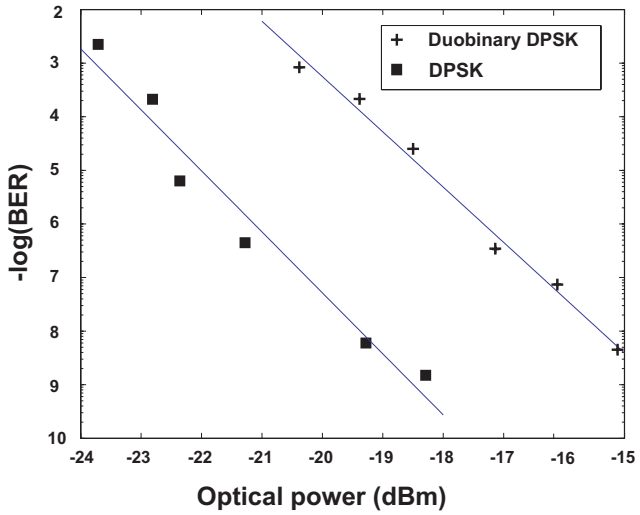


**Figure 73. NRZ DPSK and duobinary DPSK back-to-back sensitivity.**

## 4.3 Duobinary DPSK: study of a 10 Gb/s transmission

In the previous paragraph, we presented the practical implementation of a continuous-phase modulation format which shows a reduced spectrum compared to conventional NRZ DPSK. In this section, we investigate the supposed properties of duobinary DPSK in a 10 Gb/s transmission using a recirculating loop.

### 4.3.1 Optical spectrum

At 10 Gb/s, the optical spectrum is not measured with a scanning Fabry-Pérot interferometer anymore, but directly with an optical spectrum analyser (APEX AP2040A) with a 100 MHz resolution. NRZ DPSK is generated by the two methods described in Figure 25. If differences are noticed between the NRZ DPSK spectra, the conclusions drawn at 2 Gb/s for duobinary DPSK are still valid: the side lobes are suppressed.

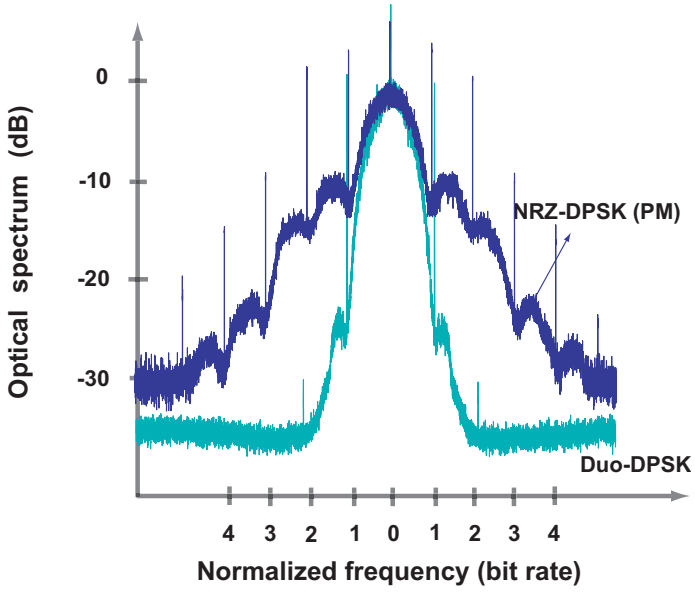


**Figure 74. Experimental optical sprectum of NRZ DPSK (PM: phase modulator, MZM: Mach-Zenhder modulator) and duobinary DPSK modulations.**

### 4.3.2 Transmission tolerance: dispersion/non lineariries

#### *4.3.2.1 Tolerance to chromatic dispersion*

Preliminary results at 2 Gb/s (Figure 72) show the reduced spectral occupation of duobinary DPSK compared to NRZ DPSK. These results are synonym of a better tolerance to group-velocity dispersion, which seems to be confirmed by the 10 Gb/s simulations (Figure 75). Although DPSK initially demonstrates a higher eye opening, the trend is reversed after 40 km propagation in standard single mode fiber with dispersion parameter $D$ = 17ps/(nm.km).

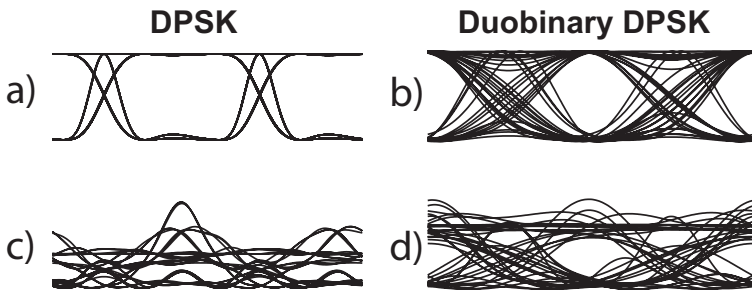


**Figure 75. Dispersion tolerance (numerical simulations).**

We measured the eye opening penalty using the experimental setup of Figure 76. The acquisition of a 10 Gb/s BERT, DPSK demodulator, and a balanced detector allowed us to operate in closer conditions to deployed lines in which the main impairment is the chromatic dispersion. We can see on Table 2 that, at 2 Gb/s, if we can demonstrate the modulation/demodulation principles, we cannot observe the same dispersion impact on such short distances (40 km) as at 10 Gb/s. The signal distortions are successively observed after 0, 20, and 40 km propagation (Figure 77).

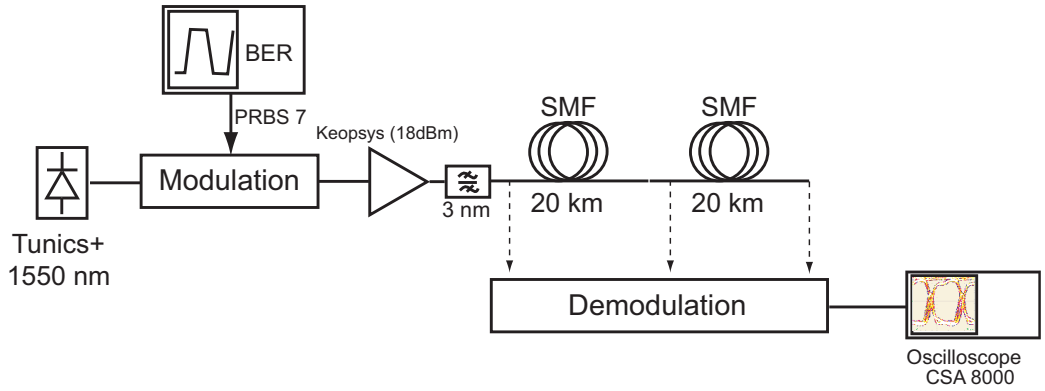


**Figure 76. Dispersion tolerance.**

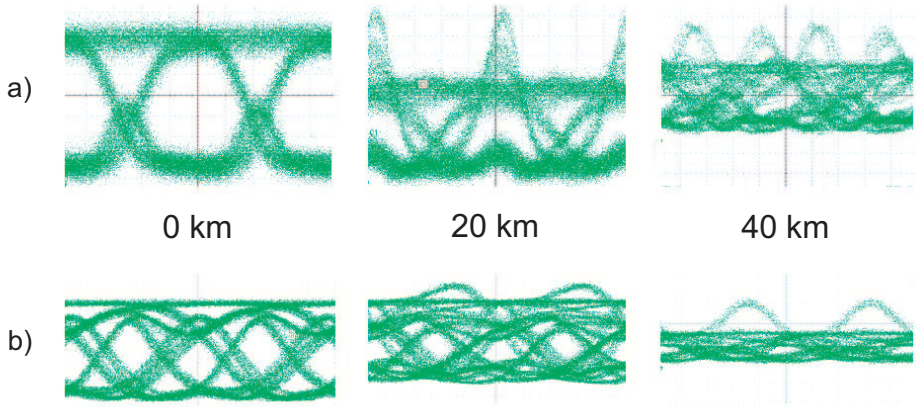


**Figure 77. Dispersion tolerance: a) NRZ-DPSK b) Duobinary DPSK.**

Conclusions that can be drawn from this experiment are in good agreement with numerical simulations. The eye opening penalty defined by equation (47) quantifies the dispersion tolerance. Results (Figure 78) show the initial trend inversion so that, finally, duobinary DPSK has a 1.2 dB higher opening than DPSK after 40 km propagation. This gain is significant since it can be used to increase the amplifier spacing for a constant performance level.

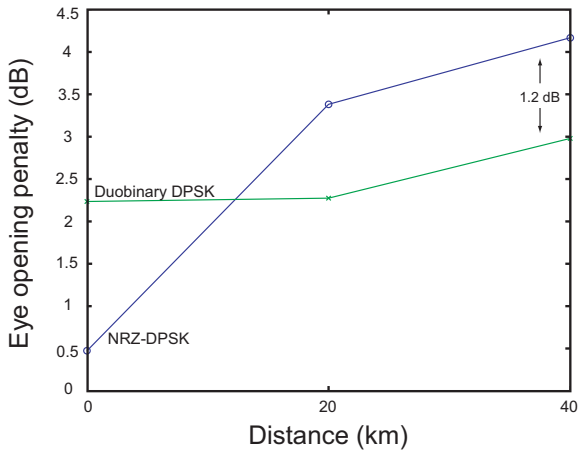


**Figure 78. Eye opening penalty (dB) as a function of propagation distance for NRZ-DPSK and duobinary DPSK modulation.**

#### *4.3.2.2 Tolerance to nonlinearity*

The idea is to introduce additional ASE noise to artificially impair the OSNR at the transmitter, then quantify the impact on the performances after transmission. After several tries, we chose the following experimental setup (Figure 79):

- The signal first propagates in 1 km of highly nonlinear fiber (HNLF) ($\gamma = 13W^{-1}km^{-1}$, $\lambda_{ZD} = 1550$ nm) then in 20 km of DSF ($\gamma = 2W^{-1}km^{-1}$, $\lambda_{ZD} = 1553$ nm).

- To get a fair comparison of all the generated formats, the average power injected in the line when the ASE source is shutdown is set to 10.4 dBm. In these conditions, the spectrum peak power is measured at a 0.07 nm resolution then normalized at 0.01 nm. The gain of the amplifiers are adjusted so that this value remains constant. If no precaution is taken, the ASE injected with the signal quickly saturates the optical amplifiers and their gains are dramatically decreased. The signal is less amplified and we don't get the same level of nonlinearity.

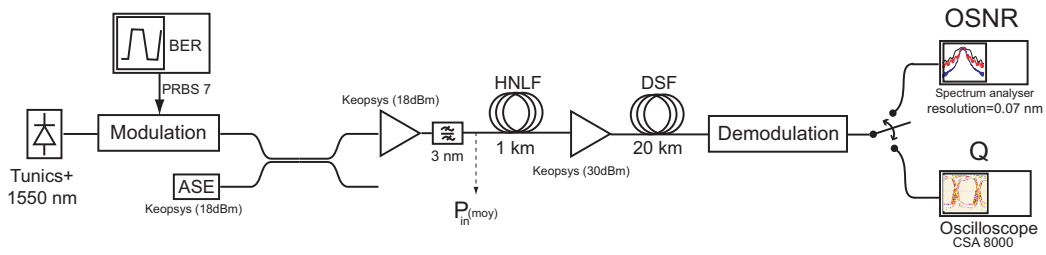


**Figure 79. Tolerance to nonlinearity.**

The absolute criterion for performance measurement is the BER. However, we encountered two experimental difficulties which forced us to use the Q factor measurement. First, our BERT was not able to synchronize the 10 Gb/s emitted and received sequences for duobinary DPSK, even in back-to-back conditions. It was not really a surprise because at 2 Gb/s, the BER (Anritsu MP1632A) was only able to synchronize in manual mode (phase and threshold). When the BER curves are plotted as a function of both phase and threshold (Figure 80), we see how duobinary DPSK requires a careful attention given the smaller range of parameters that allow the reach of a low BER.

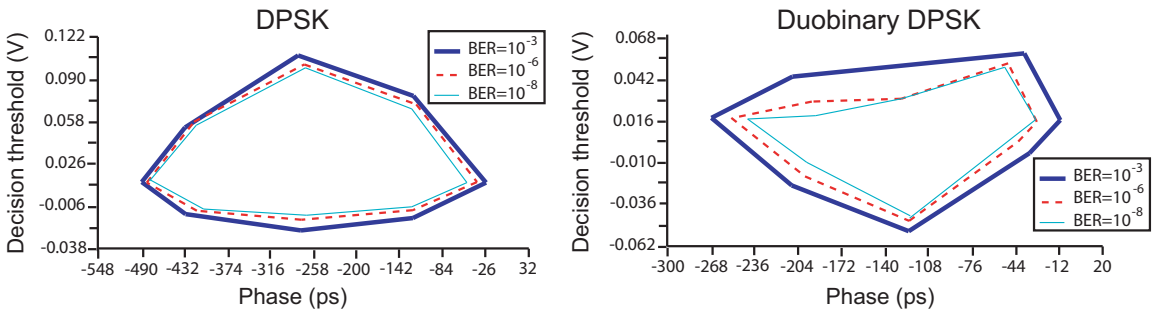


**Figure 80. BER curves as a function of both phase and decision threshold (2 Gb/s).**

The 10 Gb/s BERT had no manual mode. Moreover, we had problems with the balanced detector. That is why we have chosen to perform a Q factor measurement according to (48). For each modulation format, means ($\mu_1$, $\mu_0$) and variances ($\sigma_1$, $\sigma_0$) are measured on the

eye diagram with the histogram function of our oscilloscope (CSA8000) on a 20 ps time window. The linear Q factor obtained when the OSNR is gradually degradated by the ASE are plotted on Figure 81 for various modulation formats.

Under the classical IMDD (Intensity Modulated Direct Detection) assumptions and a Gaussian statistic for the noise, the relation between the BER and the Q factor is

$$BER(Q) = \frac{1}{2} erfc(\frac{Q}{\sqrt{2}}) \text{ o } erfc(x) = \frac{2}{\sqrt{\pi}} \int_{x}^{+\infty} e^{-\alpha^2} d\alpha. \qquad (173)$$

This relation is therefore not strictly valid for DPSK signals but gives an idea of the BER reached. As a $10^{-9}$ BER is obtained for a linear Q factor of 6, the majority of the measurements concerns very low BER. They are not in the $10^{-3}$-$10^{-9}$ range. Even if this setup does not reproduce realistic transmission conditions, it gives the general trends more than a full characterization.

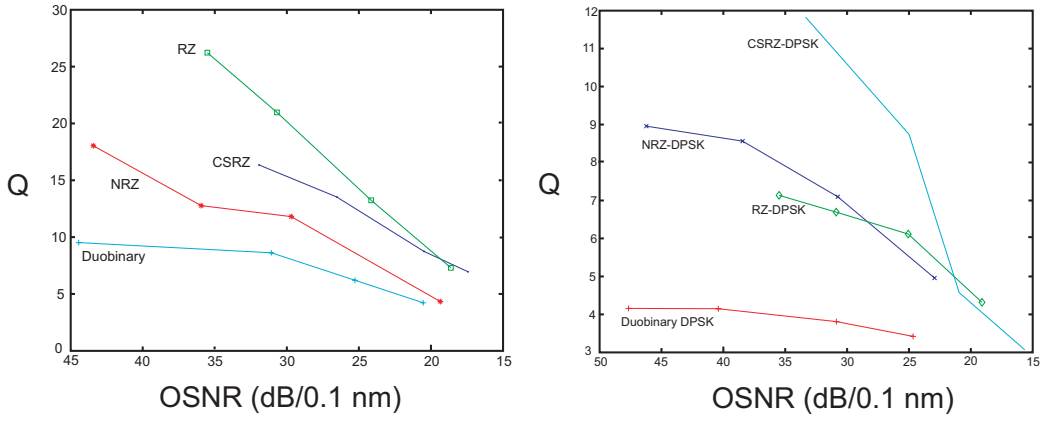


**Figure 81. Tolerance to nonlinearity.**

For intensity modulated formats, the trends are in agreement with already published results. RZ formats demonstrate a better tolerance than NRZ or duobinary although their level of SPM are a priori higher since for an equal average power, their peak power is higher than NRZ [120]. Nevertheless, the pulse train of the RZ signal is independent of the data sequence which makes it robust to SPM impairments related to pulse pattern dependence.

In the case of CSRZ, it has been shown [121, 122] that nonlinearity is mainly caused by intra four-wave mixing (IFWM) [123]. As far as the modulation phase is concerned, the trend is similar although differences in Q values are smaller except for duobinary DPSK.

#### *4.3.2.3 Sensitivity*

For various modulation format, we did the same measurements as the ones done in paragraph 4.2.3. The main difference, apart from the change in bit rate, is that only Q factors are measured. The signal is not filtered after detection before being passed to the error detector. The results on Figure 82 show the different thermal noise sensitivities. Using re-

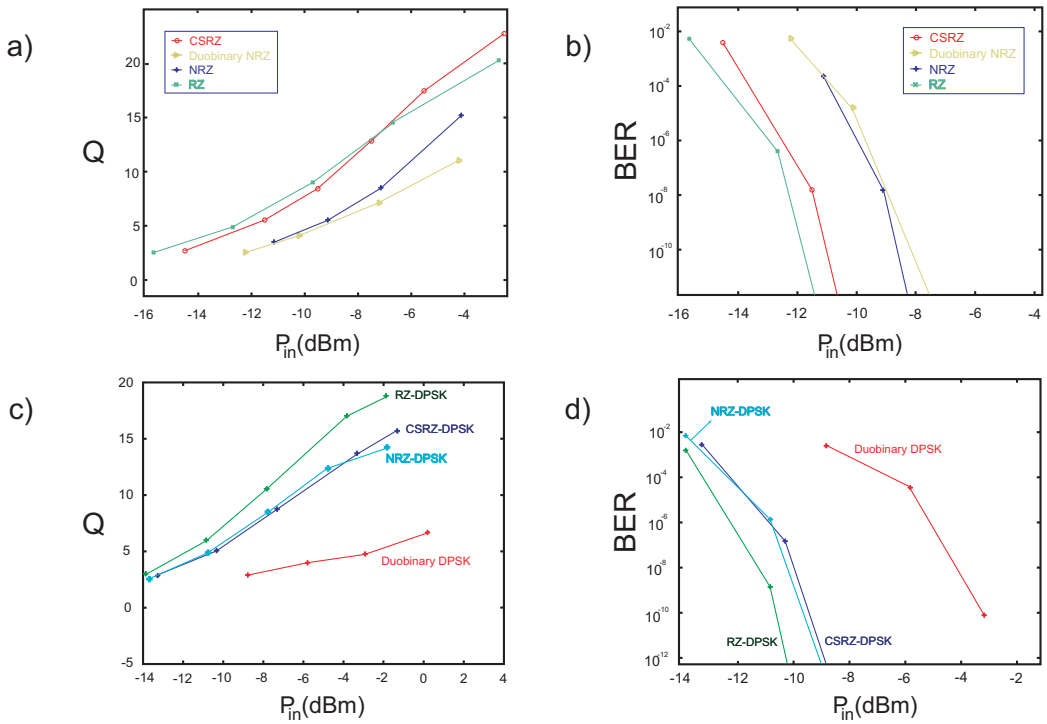


**Figure 82. Sensitivity: a)-b) intensity modulation (NRZ, RZ, CSRZ, and duobinary), c)-d) phase modulation (NRZ-DPSK, RZ-DPSK, CSRZ-DPSK, and duobinary DPSK).**

lation (173) with the same precautions leads to an estimate of the BER involved. In general, one can see the greater sensitivity of RZ formats over their NRZ counterparts [124–126]. This advantage helps in decreasing the average power injected in the fiber or in increasing the transmission distance with the same BER at receiver [127]. This difference seems less

important for phase-modulated formats. As far as duobinary DPSK is concerned, the observed difference with NRZ DPSK is larger than at 2 Gb/s. Besides a higher eye closure — which contributes in decreasing the Q factor — we have to stay cautious in the conclusions we draw and remember that they are subjected to the validity of the BER-Q relation which is strictly not valid for phase modulations.

### 4.3.3 Recirculating loop

In this paragraph, we study the behavior of various modulation formats in general ... and duobinary DPSK in particular. The experiment is very close to a real transmission because all the previously cited impairments will interplay together on longer distances. We will present the results after a description of the experimental setup.

#### *4.3.3.1 Recirculating loop: principles*

As we did not dispose of enough fiber spans to perform a straight line experiment, we built a recirculating loop [48, 106]. By controlling the light path during a certain time, we are able to simulate the signal propagation over a distance $N \times L$ where $N$ is the number of loops and $L$ the loop length. The experimental setup (Figure 83) is divided into 3 parts:

- data generation/modulation. We have only investigated NRZ (the most used), RZ (the first commercial competitor of NRZ), DPSK (the first phase modulation format used), and duobinary DPSK.

- The recirculating loop. We use a 50/50 coupler for its input/output, a 20 km SMF span compensated by a 4 km DCF span, an in-line amplifier followed by an optical bandpass filter (0.25 nm). As data are continuously emitted, the loop is controlled by two acousto-optic modulators (AO). The first one controls the data emission whereas the second one flushes the loop before the initialization of a new cycle.

- Data demodulation/detection. After each turn in the loop, the signal is demodulated and analyzed. After detection, the discrimination between all the turns is done by applying the appropriate gate to the oscilloscope trigger, defining the observation time

window. The function generator, synchronized with the AO command, pilots the gated trigger of the oscilloscope (Infiniium 86100B), allowing us to see the eye diagram of a given turn. Figure 84 presents several screen captures of the loop control oscilloscope. The first two images are obtained when the gain of the in-line amplifier does not exactly compensate the loop losses. The successive rectangles with decreasing amplitudes (channel X) represent the detected power of the successive turns between two emissions. The tuning of the observation gate delay (channel Y) allows the selection of a particular turn, respectively the $2^{nd}$ and $5^{th}$ ones in Figure 84 a and 84 b. The latter also shows that the equivalence between a recirculating loop and a straight line is not strict. The gain fluctuations of the optical amplifier occur on a time scale comparable to the time propagation in the loop (116.9 $\mu$s). That is why filling up the loop at its maximum is mandatory to avoid gain oscillations. We get Figure 84 c by optimizing the settings and compensating for the losses.

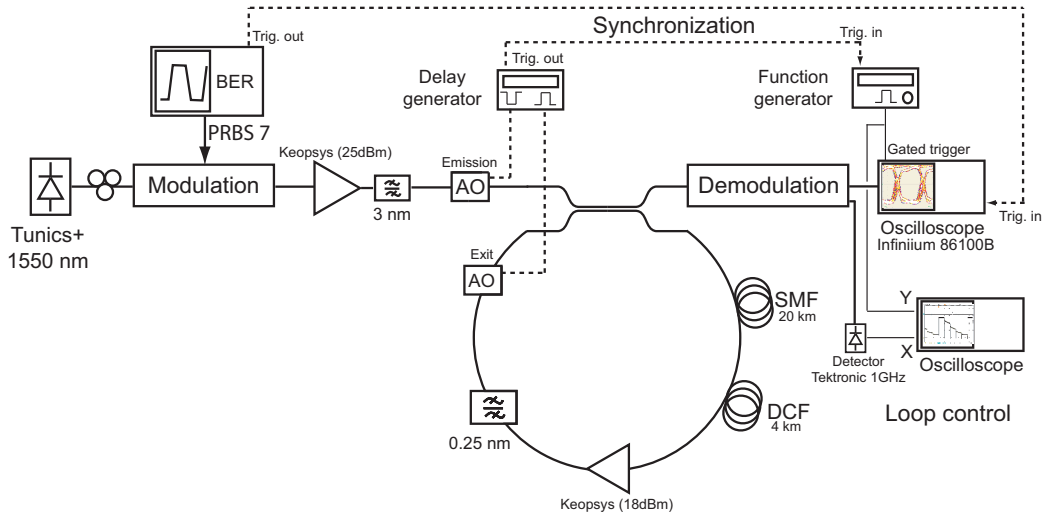


**Figure 83. Recirculating loop.**

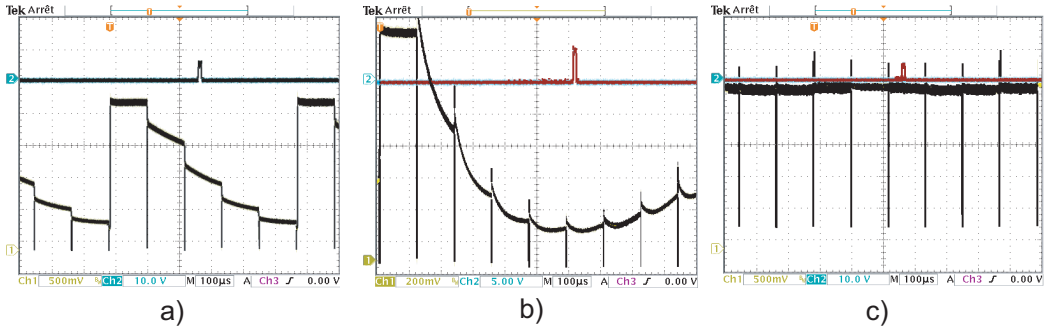


**Figure 84. Recirculating loop control.**

### *4.3.3.2 Practical implementation of the recirculating loop*

We present the aspects of the recirculating loop experiment done in our lab. The pictures in Figures (85)–(87) correspond to the particular case of a RZ DPSK modulation.

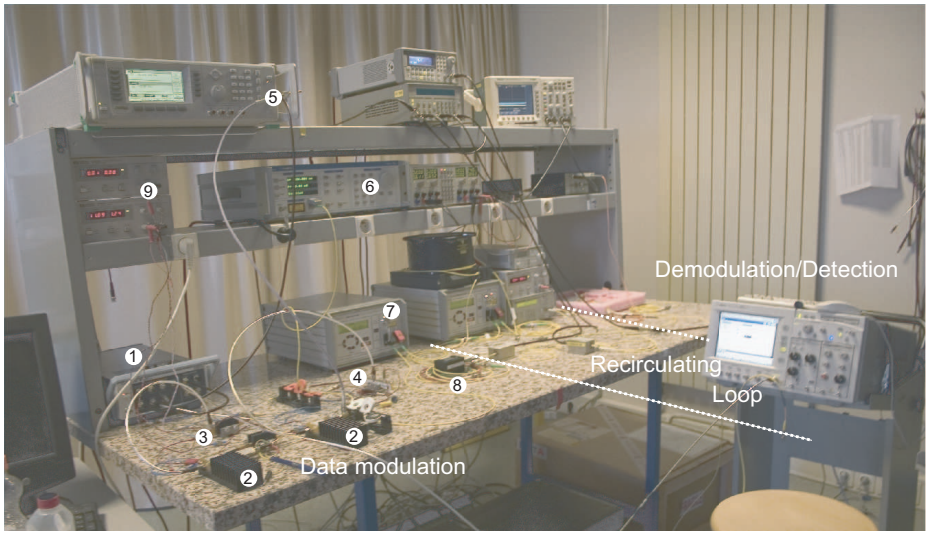


**Figure 85. General view of the experimental setup.**

- 1 BERT Yokogawa (10 Gb/s)
- 2 RF amplifiers SHF (gain 18 dB, 26 GHz bandwidth) for the data and the clock of the pulse carver
- 3 and 4 are respectively phase (for data) and intensity (pulse carving) modulators
- 5 Frequency generator, its 10 GHz output imposes the BERT clock (10G external clock in) and pilots the pulse carver
- 6 Tunnable laser source (Tunics+, $\lambda$ = 1550 nm)
- 7 8 Booster Keopsys with its optical filter (Dicon 3 nm) to decrease the level of ASE noise injected in the loop
- 9 Power sources of the RF amplifiers and DC bias of the pulse carver

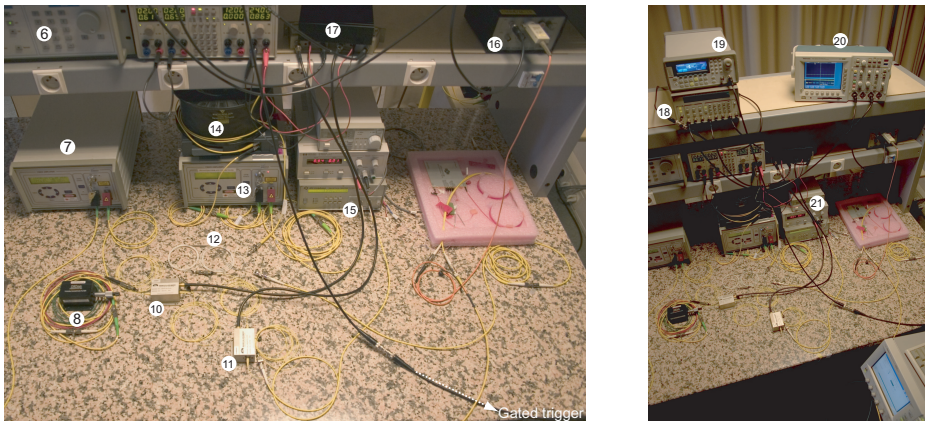


**Figure 86. Details of the experimental setup, the recirculating loop.**

- 10-11 Acousto-optic switches
- 12 Coupler 50-50 input/ouput of the loop
- 13-15 In-line optical amplifier with its optical bandpass filter (JDS Uniphase 0.25 nm)

- 14 SMF span and its compensation module of DCF
- 16 Loop control detector, loop control oscilloscope 20
- 17 Drivers of the acousto-optic switches commanded by the delay generator 18
- 19 Function generator in pulse mode (burst mode, synchronized on the acousto-optics command) piloting the gated trigger of the fast oscilloscope
- 21 Temperature controler of the DPSK demodulator, heater for phase fine tuning
- 22 DPSK demodulator

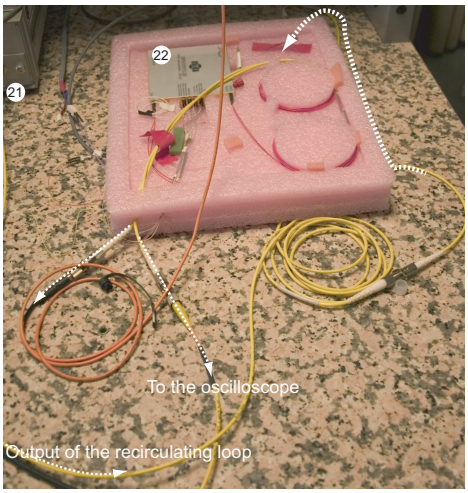


**Figure 87. DPSK demodulator.**

#### *4.3.3.3 Results*

In this paragraph, we present the experimental results we observed for the considered modulation formats on the form of eye diagrams (Figure 88). We were unable to perform a BER measurement at any given distance because our BERT did not have a burst mode trigger. For each format, the average power at the booster output is set to 10.35 dBm and 4.25 dBm at the loop input. In all cases, we observe the characteristic distortions of the chromatic dispersion. It is not exactly compensated in our loop which causes residual dispersion to

accumulate significantly after 240 km (10 turns). Dispersion is therefore the limiting effect in our setup. The resulting pulse broadening is particularly visible for RZ pulses but also affects the other formats. Although NRZ formats have reduced spectra with comparison to their RZ counterparts, the NRZ $0 \rightarrow 1/1 \rightarrow 0$ transitions become less and less abrupt.

The eye diagrams have similar eye closure evolutions except for NRZ DPSK at 480 km and duobinary DPSK from 240 km. However, several observations common to all phase-modulated formats can explain this fact. First, the tuning of the phase is sensitive enough for the optimization being difficult to perform for long distances. Moreover, direct detection is synonym of sensitivity loss since only one port of the interferometer is used for detection. Finally, NRZ DPSK and duobinary DPSK were the last 2 formats to be generated. At this step and only at this step, we measured a 11 dB loss for the optical filter in the loop [1]. That changed the power budget in the loop so that the excess gain needed by the compensation of the extra loss modified the level of ASE noise in the loop. This difference helps in explaining why it was impossible to get a clear eye diagram after 480 km (20 turns) for the duobinary DPSK modulation although its dispersion tolerance is higher than NRZ DPSK.

[1] For only 6 dB in the specifications sheets

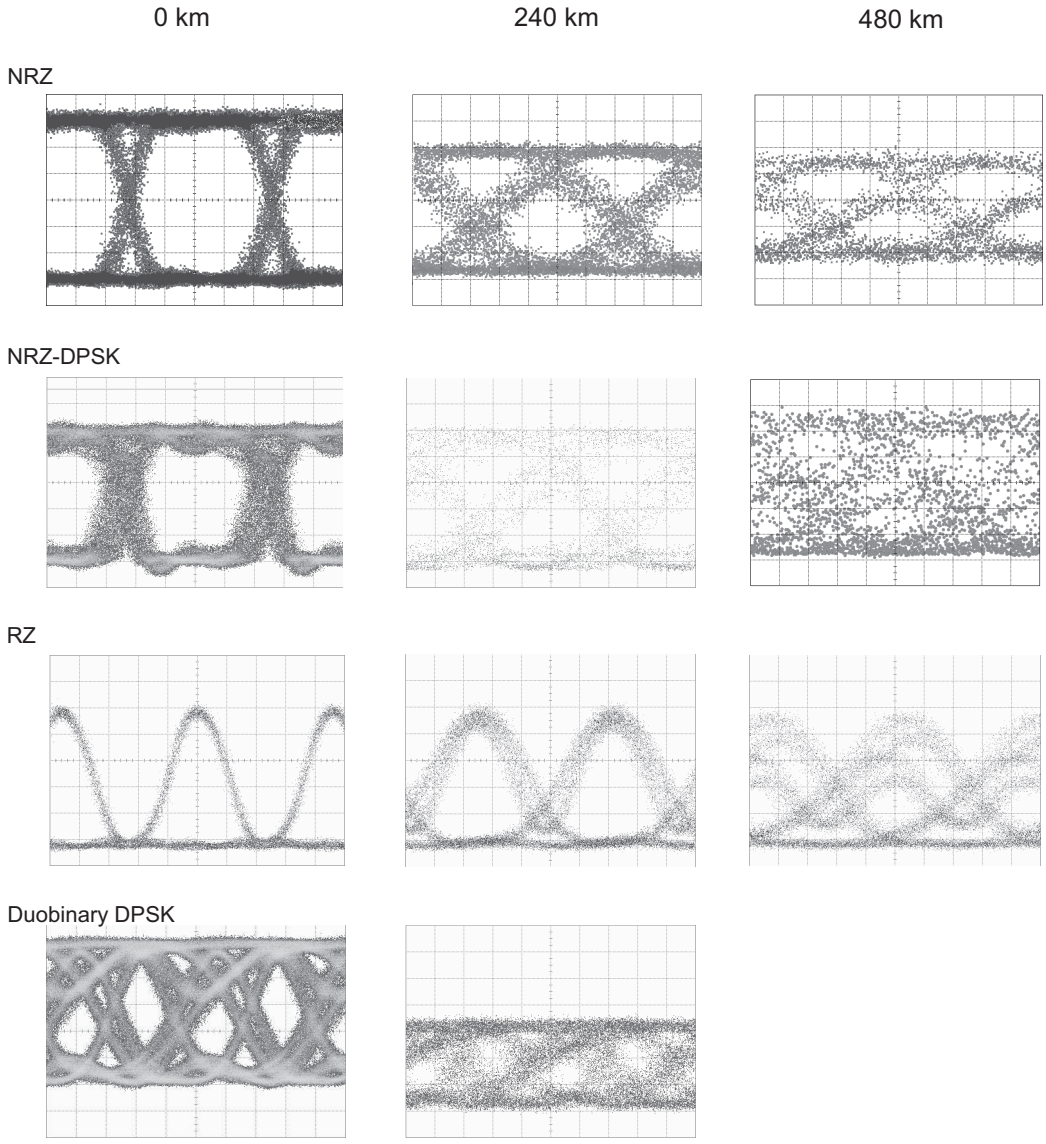


**Figure 88. Eye diagrams of the various modulation formats after 0, 240, and 480 km propagation in the recirculating loop.**

# CHAPTER 5

# CONCLUSION

In this work, we tried to better understand the implications underlying the use of optical phase-modulated communication systems. New perspectives in the field show the significant renewed interest for phase modulation. Subjected to the hegemony of intensity modulation/optical amplification, phase modulation has nonetheless all the required qualities to operate under increasingly demanding conditions. Its resistance to various nonlinear effects, to cascaded filtering and its higher spectral efficiency make it a potential future commercial standard.

That is why our research first focused on its main limitation, phase jitter, which was evaluated with a new and more efficient technique. We proposed an approach to evaluate the phase variance for arbitrary pulses in dispersion-managed links based on the moment method. This calculation only required the knowledge of the unperturbed optical signal, therefore avoiding the time consuming computation of average quantities over a statistically significant number of noise sample functions. The deterministic part of the problem is carried out numerically by use of the split-step Fourier algorithm. This approach is validated by comparison with direct Monte Carlo simulations in a DM soliton system and a quasilinear channel, which both show excellent agreement with a computation time reduced from hours to seconds on current desktop computers. As far as the transmission line was concerned, two refinements were successively considered to control the phase-to-intensity noise conversion: in-line filtering and spectral inversion.

A second approach got onto the effect of sliding filters on the optical phase jitter of soliton pulses in single-channel constant-dispersion links. As the ASE noise that has exactly the soliton center frequency is less attenuated than the soliton itself, it grows exponentially with distance, creating a strong continuum wave that deteriorates the transmission. An analytical expression for the phase standard deviation was derived in that case by use

of the soliton perturbation theory before being validated by comparison with Monte Carlo simulations. Finally, we investigated the cumulative effects of ASE and dispersion, which deteriorate the transmission performances of a 10 Gbit/s WDM transmission line using a DPSK modulation. The experimental results showed the influence of Gordon-Mollenauer and SPM-GVD effects and established the tolerance of the DPSK and CSRZ DPSK modulation format against them.

The physical insights brought by this theoretical work and our first experimental results were used in a practical setup which performed optical phase variance estimations. Previous studies have investigated the probability density of nonlinear phase noise and its impact on the degradation of phase-modulated systems. In simulations, a differential phase Q factor is used to predict the BER more accurately. This method essentially addresses the impossibility of error counting in simulations and proposes a useful BER estimate by evaluating the statistical fluctuations of the received signal. If the key parameters, i.e. the standard deviations of the differential phase on 0 and $\pi$ rails, are easily evaluated in simulations, their experimental evaluation is far from being straightforward. The experimental method we proposed is a practical answer to this challenge and allow a simple and cost effective performance evaluation of standard DPSK-based communications. This novel method is based on histogram measurements performed before and after demodulation. The estimation of the optical phase jitter relies on the assumption that the phase and amplitude noise are Gaussian and independent. This simplification allows us to relate the phase variance to easily measurable physical parameters and yields estimations in good agreement with the ones obtained by numerical simulations.

Recently, a strong interest has been shown in differential quadrature phase-shift-keyed (DQPSK) and multi-level modulation formats. These schemes have favorable spectral width and exhibit high tolerances for chromatic and polarization-mode dispersion at the same bit rate as binary modulation. Our work, although, is focused on DPSK signals is nevertheless not restricted to them because the physical mechanisms driving the nonlinear

phase noise impairment are the same.

Beyond this approach addressing an intrinsic problem related to any phase-modulated scheme, we conducted a specific study on a particular type of partial response, continuous phase-modulated format: duobinary DPSK. Such a scheme, common in RF, was not used in optical communications. After a simulation phase whose goal was a first characterization, we implemented a 2 Gb/s coder/decoder in a laboratory experiment. The first experimental validation done, we further measured the performance of duobinary DPSK modulation at 10 Gb/s. All the different experimental setups – chromatic dispersion, nonlinearity and transmission tolerance – were many occasions to compare its performances with conventional formats. Their behaviors are limited by many constraints whose complexity, interdependence and degree of expression vary with the considered system. So we can pretty much say that the general trends we observed have only the relative range of conclusions related to our particular recirculating loop structure.

# APPENDIX A

# ACRONYMS

| | |
|---|---|
| APRZ | Alternate Phase Return to Zero |
| ASE | Amplified Spontaneous Emission |
| AWG | Arrayed Waveguide Grating |
| BER | Bit Error Rate |
| BERT | Bit Error Rate Tester |
| CF RZDPSK | Chirp Free RZDPSK |
| CRZ | Chirped Return to Zero |
| CSRZ | Carrier Suppressed Return to Zero |
| DCF | Dispersion Compensating Fiber |
| DFB | Distributed FeedBack |
| DFF | Dispersion-Flattened Fiber |
| DGD | Differential Group Delay |
| DM | Dispersion Management |
| DMF | Dispersion-Managed Fiber |
| DPSK | Differential Phase Shift Keying |
| DSF | Dispersion Shifted Fiber |
| EDFA | Erbium-Doped Fiber Amplifier |
| ESNL | NonLinear Schrödinger Equation |
| FEC | Forward Error Correction |
| FFT | Fast Fourier Transform |
| FWM | Four-Wave Mixing |
| GEF | Gain Equalizing Filter |
| GVD | Group-Velocity Dispersion |
| IMDD | Intensity Modulated Direct Detection |
| IST | Inverse Scattering Theory |
| MZM | Mach-Zehnder Modulator |
| MZDI | Mach-Zenhder Delay Interferometer |
| NPSC | Nonlinear Phase Shift Compensation |
| NRZ | Non Return to Zero |
| OOK | On-Off keying |
| OPC | Optical Phase Conjugation |
| OSNR | Optical Signal to Noise Ratio |

| | |
|---|---|
| PMD | Polarisation Mode Dispersion |
| PC | Phase Conjugator |
| PRBS | Pseudo Random Bit Sequence |
| PSBT | Phase Shaped Binary Transmission |
| PSK | Phase Shift Keying |
| QPSK | Quadrature Phase Shift Keying |
| RF | Radio Frequency |
| RS | Reed Solomon |
| RZ | Return to Zero |
| SBS | Stimulated Brillouin Scattering |
| SMF | Single Mode Fiber |
| SNR | Signal to Noise Ratio |
| SPM | Self-Phase Modulation |
| SRS | Stimulated Raman Scattering |
| VSB | Vestigial Side Band |
| DWM | Wavelength-Division Multiplexing |
| WSS | Wide Sense Stationary |
| XPM | Cross-Phase Modulation |

# REFERENCES


[1] I. Kaminow and T. Li, eds., *Optical fiber communications IV B*. Academic Press, 2002.

[2] D. Bayart, P. Baniel, A. Bergonzo, J.-Y. Boniort, P. Bousselet, L. Gasca, D. Hamoir, F.Leplingard, A. L. Sauze, P. Nouchi, F. Roy, and P. Sillard, "Broadband optical fibre amplification over 17.7 THz range," *Electronics Letters*, vol. 36, pp. 1569–1571, August 2000.

[3] K. Nakagawa, "Progress in optical amplifiers and the future of optical communication systems," in Proceedings of Optical Amplifier and Applications (OAA'1999), 1999.

[4] X. Liu, X. Wei, R. E. Slusher, and C. J. McKinstrie, "Improving transmission performance in differential phase-shift-keyed systems by use of lumped nonlinear phase-shift compensation," *Optics Letters*, vol. 27, pp. 1616–1618, September 2002.

[5] C. Xu and X. Liu, "Postnonlinearity compensation with data-driven phase modulators in phase-shift keying transmission," *Optics Letters*, vol. 27, pp. 1619–1621, September 2002.

[6] A. Gnauck, G. Raybon, S. Chandrasekhar, J. Leuthold, C. Doerr, L. Stulz, A. Agarwal, S. Banerjee, D. Grosz, S. Hunsche, A. Kung, A. Marhelyuk, D. Maywar, M. Movassaghi, X. Liu, C. Xu, X. Wei, and D. Gill, "2.5 Tb/s 64 * 42.7 Gb/s Transmission Over 40*100 km NZDSF using RZ-DPSK Format and All-Raman-Amplified Spans," *OFC*, 2002. Paper FC2.

[7] J. Leibrich, C. Wree, and W. Rosenkranz, "CF-RZ-DPSK for Suppression of XPM on Dispersion-Managed Long-Haul Optical WDM Transmission on Standard Single-Mode Fiber," *IEEE Photonics Technology Letters*, vol. 14, pp. 155–157, February 2002.

[8] C. Xu, X. Liu, and X. Wei, "Ultra-Long Haul DWDM Transmission with Differential Phase Shift Keying Dispersion Managed Soliton," *ECOC*, vol. 1, September 2002.

[9] G. P. Agrawal, *Fiber-Optic Communication Systems*. Wiley-Interscience, third edition ed.

[10] M. Forzati, J. Martensson, A. Berntson, A. Djupsjbacka, and P. Johannisson, "Reduction of inttrachannel four-wave mixing using the alternate-phase RZ modulation format," *IEEE Photonics Technology Letters*, vol. 14, pp. 1285–1287, September 2002.

[11] H. Kim and A. H. Gnauck, "Experimental investigation of the performance limitation of DPSK systems due to nonlinear phase noise," *IEEE Photonics Technology Letters*, 2003.

[12] M. Hanna, H. Porte, J.-P. Goedgebuer, and W. T. Rhodes, "Soliton optical phase control by use of in-line filters," *Optics Letters*, vol. 24, pp. 732–734, February 1999.

[13] C. J. McKinstrie and C. Xie, "Phase jitter in single-channel soliton systems with constant dispersion," *IEEE Journal of Selected Topics in Quantum Electronics*, vol. 8, pp. 616–625, May-June 2002.

[14] V. S. Grigoryan, C. R. Menyuk, and R.-M. Mu, "Calculation of timing and amplitude jitter in dispersion-managed optical fiber communications using linearization," *Journal of Lightwave Technology*, vol. 17, pp. 1347–1356, August 1999.

[15] G. P. Agrawal, *Nonlinear Fiber Optics*. Academic Press, 2001.

[16] R. I. Killey, H. J. Thiele, V. Mikhailov, and P. Bayvel, "Prediction of transmission penalties due to cross-phase modulation in WDM systems using a simplified technique," *IEEE Photonics Technology Letters*, vol. 12, pp. 804–806, July 2000.

[17] S. Song, "High-order four-wave mixing and its effect in WDM systems," *Optics Express*, vol. 7, pp. 166–171, August 2000.

[18] R. M. Jopson and R. E. Tench, "Polarisation-independent phase conjugation of lightwave signals," *Electronics Letters*, vol. 29, pp. 2216–2217, December 1993.

[19] A. H. Gnauck, R. M. Jopson, and R. M. Derosier, "10 Gb/s 360 km transmission over dispersive fiber using midsystem spectral inversion," *IEEE Photonics Technology Letters*, vol. 5, pp. 663–666, June 1993.

[20] J. Herrera, F. Ramos, and J. Marti, "Nonlinear distorsion generated by DSF-based optical-phase conjugators in analog optical systems," *IEEE Photonics Technology Letters*, vol. 20, pp. 1688–1693, September 2002.

[21] G. P. Agrawal, *Applications of Nonlinear Fiber Optics*. Academic press, 2001.

[22] G. J. Foschini and C. D. Poole, "Statistical theory of polarization dispersion in single mode fibers," *Journal of Lightwave Technology*, vol. 9, pp. 1439–1456, November 1991.

[23] K. Hagimoto, K. Iwatsuki, A. Takada, M. Nakazawa, M. Saruwatari, K. Aida, K. Nakagawa, and M. Horiguchi, "250 km nonrepeated transmission experiment at 1.8 Gb/s using LD pumped $Er^{3+}$-doped fibre amplifiers in IM/direct detection system," *Electronics Letters*, vol. 25, pp. 662–664, May 1989.

[24] E. Desurvire, *Erbium doped fiber amplifiers : principles and applications*. Wiley intersciences, 1994.

[25] M. Morisaki, H. Sugahara, T. Ito, and T. Ono, "2.56-Tb/s (64x42.7 Gb/s) WDM transmission over 6000 km using all-raman amplified inverse double-hybrid spans," *IEEE Photonics Technology Letters*, vol. 15, pp. 1615–1617, November 2003.

[26] T. Okamawari, A. Maruta, and Y. Kodama, "Analysis of Gordon-Haus jitter in a dispersion-compensated optical transmission system," *Optics Letters*, vol. 23, pp. 694–696, May 1998.

[27] J. Gordon and H. A. Haus, "Random walk of coherently amplified solitons in optical fiber transmission," *Optics Letters*, vol. 11, pp. 665–667, October 1986.

[28] C. Kurtzke, "Suppression of fiber nonlinearities by appropriate dispersion management," *IEEE Photonics Technology Letters*, vol. 5, pp. 1250–1253, October 1993.

[29] T. Imai, M. Murakami, and A. Naka, "Optimum parameter guidelines for 10 Gbit/s, multimegameter transmission systems considering the nonlinear effect," *Electronics Letters*, vol. 29, pp. 1409–1411, August 1993.

[30] H. Sugahara, A. Maruta, and Y. Kodama, "Optimal allocation of amplifiers in a dispersion-managed line for a wavelength-division-multiplexed soliton transmission system," *Optics Letters*, vol. 24, pp. 145–147, February 1999.

[31] D. Marcuse, "Derivation of analytical expressions for the bit-error probability in lightwave systems with optical amplifiers," *Journal of Lightwave Technology*, vol. 8, pp. 1816–1823, December 1990.

[32] J. L. Syskind, J. Nagel, and H. D. Kidorf, *Erbium-Doped Fiber amplifiers for optical communications in Optical Fiber Communications IIIB.* Academic Press, San Diego, 1997.

[33] G. Vareille, F. Pitel, and J. F. Marcerou, "3 Tbit/s (300 x 11.6 Gbit/s) transmission over 7380 km using C+L band with 25 GHz channel spacing and NRZ format," in Proceedings of OFC'2001, Paper PD22, 2001.

[34] E. A. Golovchenko, A. N. Pilipetskii, and N. S. Bergano, "Transmission properties of chirped return-to-zero pulses and nonlinear intersymbol interference in 10 Gb/s WDM transmission," in Proceedings of OFC'00, Paper FC3, 2000.

[35] J. B. Leroy, P. Marmier, G. Vareille, and B. Julien, "12220 error-free 68x10 Gb/s transmission," in Proceedings of ECOC'02, Paper 9.1.5, 2002.

[36] Y. Miyamoto, K. Yonenaga, S. Kuwahara, M. Tomizawa, A. Hirano, H. Toba, K. Murata, Y. Tada, Y. Umeda, and H. Miyazawa, "1.2 Tbit/s (30 x 42.7 Gbit/s ETDM optical channel) WDM transmission over 376 km with 125 km spacing using forward error correction and carrier-supressed RZ format," in Proceedings of OFC'00, Paper PD26-1, 2000.

[37] Y. Miyamoto, A. Hirano, K. Yonenaga, A. Sano, H. Toba, K. Murata, and O. Mitomi, "320 Gb/s ($8 \times 40$ Gb/s) WDM transmission over 387 km with 120 km repeater spacing using carrier-suppressed return-to-zero format," *Electronics Letters*, vol. 35, pp. 2041–2042, November 1999.

[38] Y. Zhu, W. Lee, C. Scahill, C. Fludger, D. Watley, M. Jones, J. Homan, B. Shaw, and A. Hadjiofotiou, "1.28 Tbit/s (32x40 Gbit/s) transmission over 1000 km with only 6 spans," in Proceedings of ECOC00, Paper PD 1.4, 2000.

[39] H. Sugahara, M. Morisaki, T. Ito, K. Fukuchi, and T. Ono, "9000 km transmission of 32x42.7 Gb/s dense-WDM signals using 195 $\mu$m$^2$ $A_{eff}$ fiber and inverse double-hybrid span configuration," in Proceedings of Topical Meeting on Optical Amplifiers and Applications (OAA'2002), Paper PDP-3, 2002.

[40] P. Johannisson, D. Anderson, M. Marklund, A. Berntson, M. Forzati, and J. Martensson, "Suppression of nonlinear effects by phase alternation in strongly dispersion-managed optical transmission," *Optics Letters*, vol. 27, pp. 1073–1075, June 2002.

[41] D. Penninckx, "Enhanced-phase-shaped binary transmission," *Electronics Letters*, vol. 36, pp. 478–480, March 2000.

[42] H. Bissessur, L. Pierre, D. Penninckx, J.-P. Thiery, and J.-P. Hamaide, "Enhanced phase-shaped binary tranmission for dense WDM systems," *Electronics Letters*, vol. 37, pp. 45–46, January 2001.

[43] H. Bissessur, G. Charlet, W. Idler, C. Simonneau, S. Borne, L. Pierre, R. Dischler, C. D. Barros, and P. Tran, "3.2 Tb/s (80x40 Gb/s) C-band transmission over 3x100 km with 0.8 bit/s/Hz efficiency," *Electronics Letters*, vol. 38, pp. 377–379, April 2002.

[44] G. Charlet, J.-C. Antona, P. Tran, S. Bigo, W. Idler, and R. Dischler, "3.2 Tbit/s (80x42.7 Gbit/s) C-band transmission over 9x100 km of TeraLight™ fiber with 50 GHz channel spacing," in Proceedings of Topical meeting on Optical Amplifiers and Applications (OAA'2002), Paper PDP-1, 2002.

[45] Y. Yamada, S. Nakagawa, T. Kawazawa, H. Tada, and K. Goto, "2 Tbit/s (200x10 Gbit/s) over 9200 km transmission experiments using C-band EDFA and VSB format with 53% spectral efficiency," in Proceedings of SubOptic'01 Conference, Paper PDP-1, 2001.

[46] H. Bissessur, G. Charlet, E. Gohin, C. Simonneau, L. Pierre, and W. Idler, "1.6 Tbit/s (40x40 Gb/s) DPSK transmission with direct detection," in Proceedings of ECOC02, Paper 8.1.2, 2002.

[47] C. Rasmussen, T. Fjelde, J. Bennike, F. Liu, S. Dey, B. Mikkelsen, P. Mamyshev, P. Serbe, P. van der Wagt, Y. Akasaka, D. Harris, D. Gapontsev, V. Ivshin, and P. Reeves-Hall, "DWDM 40G transmission over trans-pacific distance (10000 km) using CSRZ-DPSK, enhanced FEC, and all-raman-amplified 100-km ultrawave fiber spans," *Journal of Lightwave Technology*, vol. 22, pp. 203–207, January 2004.

[48] T. Tsuritani, K. Ishida, A. Agata, K. Shimomura, I. Morita, T. Tokura, H. Taga, T. Mizuochi, N. Edagawa, and S. Akiba, "70-GHz-spaced 40x42.7 Gb/s transpacific transmission over 9400 km using prefiltered CSRZ-DPSK signals, all-raman repearters, and symmetrically dispersion-managed fiber span," *Journal of Lightwave Technology*, vol. 22, pp. 215–224, January 2004.

[49] B. Zhu, L. Nelson, A. Gnauck, C. Doerr, J. Leuthold, L. Gruner-Nielsen, M. Pedersen, J. Kim, and R.L. Lingle Jr, "High spectral density long-haul 40-Gb/s transmission using CSRZ-DPSK format," *Journal of Lightwave Technology*, vol. 22, pp. 208–214, January 2004.

[50] V. S. Grigoryan, P. S. Cho, and I. Shpantzer, "Nonlinear penalty reduction of RZ-DBPSK versus RZ-OOK modulation format in fiber communications," in Proceedings of ECOC02, Paper P 3.29, 2002.

[51] K. Sekine, N. Kikuchi, S. Sasaki, S. Hayase, C. Hasegawa, and T. Sugawara, "40 Gbit/s, 16-ary (4 bit/symbol) optical modulation/demodulation scheme," *Electronics Letters*, vol. 41, pp. 430–432, March 2005.

[52] S. Walklin and J. Conradi, "Multilevel signaling for increasing the reach of 10 Gb/s lightwave systems," *Journal of Lightwave Technology*, vol. 17, pp. 2235–2248, November 1999.

[53] R. A. Griffin and A. C. Carter, "Optical differential quadrature phase-shift key (oDQPSK) for high capacity optical transmission," in Proceedings of OFC'02, Paper WX 6, 2002.

[54] O. Vassilieva, T. Oshida, S. Choudhary, and H. Kuwahara, "Non-linear tolerant and spectrally efficient 86 Gbit/s RZ-DQPSK format for a system upgrade," in Proceedings of OFC03, Paper ThE7, 2003.

[55] P. S. Cho, G. Harston, C. J. Kerr, A. S. Greenblatt, A. Kaplan, Y. Achiam, G. Levy-Yurista, M. Margalit, Y. Gross, and J. B. Khurgin, "Investigation of 2-b/s/Hz 40-Gb/s DWDM transmission over 4x100 km SMF-28 fiber using RZ-DQPSK and polarization multiplexing," *IEEE Photonics Technology Letters*, vol. 16, pp. 656–658, February 2004.

[56] T. Tockle, C. Davidson, M. Nissov, J.-X. Cai, D. Foursa, and A. Pilipetskii, "6500 km transmission of RZ-DQPSK WDM signals," *Electronics Letters*, vol. 40, pp. 444–445, April 2004.

[57] T. Inoue, K. Ishida, T. Tokura, E. Shibano, H. Taga, K. Shimizu, K. Goto, and K. Motoshima, "150 km repeater span transmission experiment over 9000 km," in Proceedings of ECOC04, Paper Th4.1.3, 2004.

[58] S. Lin and D. J. Costello, *Error control coding : fundamentals and applications*. Prentice Hall, Englewood Cliffs, NJ., 2004.

[59] J. L. Pamart, E. Lefranc, S. Morin, G. Balland, Y. C. Chen, T. M. Kissel, and J. L. Miller, "Forward error correction in a 5 Gbit/s 6400 km EDFA based system," *Electronics Letters*, vol. 30, pp. 342–343, February 1994.

[60] C. R. Davidson, C. J. Chen, M. Nissov, A. Pilipetskii, M. Ramanujam, H. D. Kidorf, B. Pedersen, M. A. Mills, C. Lin, M. I. Hayee, J. X. Cai, A. B. Puc, P. C. Corbett, R. Menges, H. Li, A. Elyamani, C. Rivers, and N. S. Bergano, "1800 Gb/s transmission of one hundred and eighty 10 Gb/s WDM channels over 7000 km using the full EDFA C-band," pp. 242–244, in proceedings of OFC'00, Paper PD-25 1, 2000.

[61] O. A. Sab and J. Fang, "Concatenated forward error correction schemes for long-haul DWDM optical transmission systems," in Proceedings of ECOC'99, Paper ThC2.4, 1999.

[62] O. A. Sab, "FEC techniques in submarine transmission systems," in Proceedings of OFC01, Paper TuF1-1, 2001.

[63] H. Taga, H. Yamauchi, K. Goto, N. Edagawa, and M. Suzuki, "Performance improvement of highly nonlinear long-distance optical fiber transmission system using novel high gain forward error correcting code," in Proceedings of OFC01, Paper TuF3-1, 2001.

[64] T. Kobayashi, K. Shimizu, K. Ouchi, K. Ishida, Y. Miyata, T. Tokura, J. Abe, T. Mizuochi, and K. Motoshima, "10 Gbit/s RZ-DPSK receiver with a sensitivity of -50.5 dbm (7 photons per information bit) using block turbo code FEC," in Proceedings of ECOC03, Paper Tu1.6.6.

[65] K. Shimizu, Y. Miyata, T. Mizuochi, K. Ouchi, T. Kobayashi, H. Yoshida, and K. Motoshima, "Optimum soft-decision FEC thresholds for On-Off keying optical receiver using block turbo code," in Proceedings of OFC04, Paper WM2, 2004.

[66] D. G. Foursa, C. R. Davidson, M. Nissov, M. A. Mills, L. Xu, J. X. Cai, A. N. Pilipetskii, Y. Cai, C. Breverman, R. R. Cordell, T. J. Carvelli, P. C. Corbett, H. D. Kidorf, and N. S. Bergano, "2,56 Tb/s (256x10 Gbit/s) transmission over 11000 km using hybrid Raman/EDFAs with 80 nm of continuous bandwidth," in Proceedings of OFC02, Paper FC3, 2002.

[67] J.-X. Cai, D. G. Foursa, C. R. Davidson, Y. Cai, G. Domagala, H. Li, L. Liu, W. W. Patterson, N. A. Pilipetskii, M. Nissov, and N. S. Bergano, "A DWDM demonstration of 3.73 Tb/s over 11000 km using 373 RZ-DPSK channels at 10 Gb/s," in Proceedings of OFC03, Paper PD22, 2003.

[68] J.-X. Cai, D. G. Foursa, L. Liu, C. R. Davidson, Y. Cai, W. W. Patterson, A. J. Lucero, B. Bakhshi, G. Mohs, P. C. Corbett, V. Gupta, W. Anderson, M. Vaa, G. Domagala, M. Mazurczyk, H. Li, M. Nissov, A. N. Pilipetskii, and N. S. Bergano, "RZ-DPSK field trial over 13,000 km of installed non slope-matched submarine fibers," in Proceedings of OFC04, Paper PDP34, 2004.

[69] A. H. Gnauck, J. Leuthold, C. Xie, I. Kang, S. Chandrasekhar, P. Bernasconi, C. Doerr, L. Buhl, J. D. Bull, N. A. F. Jaeger, H. Kato, and A. Guest, "6x42.7 Gb/s transmission over ten 200 km EDFA-amplified SSMF spans using polarization-alternating RZ-DPSK," in Proceedings of OFC04, Paper PDP35, 2004.

[70] G. Charlet, E. Corbel, J. Lazaro, A. Klekamp, R. Dischler, P. Tran, W. Idler, H. Mardoyan, A. Konczykowska, F. Jorge, and S. Bigo, "WDM transmission at 6 Tbit/s capacity over transatlantic distance, using 42.7 Gb/s differential phase-shift keying without pulse carver," in Proceedings of OFC04, Paper PDP36, 2004.

[71] L. Becouarn, G. Vareille, S. Dupond, P. Plantady, J. F. Marcerou, A. Klekamp, R. Dischler, W. Idler, and G. Charlet, "42x42.7 Gb/s RZ-DPSK transmission over a 4820 km long NZDSF deployed line using C-band-only EDFAs," in Proceedings of OFC04, Paper PDP37, 2004.

[72] N. Yoshikane and I. Morita, "1.14 b/s/Hz spectrally-efficient 50x85.4 Gb/s transmission over 300 km using copolarized CS-RZ DQPSK signals," in Proceedings of OFC04, Paper PDP38, 2004.

[73] A. Suzuki, X. Wang, Y. Ogawa, and S. Nakamura, "10x320 Gb/s (3.2Tb/s) DWDM/OTDM transmission in C-band by semiconductor-based devices," in Proceedings of ECOC04, Paper Th4.1.7, 2004.

[74] A. Gnauck, S. Chandrasekhar, J. Leuthold, and L. Stulz, "Demonstration of 42.7-Gb/s DPSK Receiver with 45 Photons/Bit Sensitivity," *IEEE Photonics Letters*, vol. 15, pp. 99–101, January 2003.

[75] T. Hoshida, O. Vassilieva, K. Yamada, S. Choudhary, R. Pecqueur, and H. Kuwahara, "Optimal 40 Gb/s modulation formats for spectrally efficient long-haul DWDM systems," *Journal of Lightwave Technology*, 2002.

[76] C. Paré, A. Villeneuve, P.-A. Bellanger, and N. J. Doran, "Compensation for dispersion and the nonlinear Kerr effect without phase conjugation," *Optics Letters*, vol. 21, pp. 459–461, April 1996.

[77] I. R. Gabitov and P. M. Lushnikov, "Nonlinearity management in a dispersion-managed system," *Optics Letters*, vol. 27, pp. 113–115, January 2002.

[78] P. Vidaković and D. J. Lovering and J. A. Levenson and J. Webjörn and P. St. J. Russel, "Large nonlinear phase shift owing to cascaded $\chi^2$ in quasi-phase-matched bulk $LiNbO_3$," *Optics Letters*, vol. 22, pp. 277–279, March 1997.

[79] J. Hansryd, J. van Howe, and C. Xu, "Experimental demonstration of nonlinear phase jitter compensation in DPSK modulated fiber links," *IEEE Photonics Technology Letters*, vol. 17, pp. 232–234, January 2005.

[80] M. C. Tatham, G. Sherlock, and L. D. Westbrook, "Compensation fibre chromatic dispersion by optical phase conjugation in a semiconductor laser amplifier," *Electronics Letters*, vol. 29, pp. 1851–1852, October 1993.

[81] R. J. Essiambre and G. P. Agrawal, "Timing jitter of ultrashort solitons in high-speed communication systems. I. General formulation and application to dispersion-decreasing fibers," *Journal of Optical Society of America B*, vol. 14, pp. 314–322, February 1997.

[82] S. Watanabe and M. Shirasaki, "Exact compensation for both chromatic dispersion and Kerr effect in a transmission fiber using optical phase conjugation," *Journal of Lightwave Technology*, vol. 14, pp. 243–248, March 1996.

[83] S. Watanabe and T. Chikama, "Cancellation of four-wave mixing in multichannel fibre transmission by midway optical phase conjugation," *Electronics Letters*, vol. 30, pp. 1156–1157, July 1994.

[84] A. Chowdhury, G. Raybon, R.-J. Essiambre, J. Sinsky, A. Adamiecki, J. Leuthold, C. R. Doerr, and S. Chandrasekhar, "Compensation of intra-channel nonlinearities in 40 gb/s pseudo-linear systems using optical phase conjugation," in Proceedings of OFC04, Paper PDP32, 2004.

[85] S. L. Jansen, D. van den Borne, C. C. Monsalve, S. Spälter, P. M. Krummrich, G. D. Khoe, and H. de Waardt, "Reduction of Gordon-Mollenauer phase noise by midlink spectral inversion," *IEEE Photonics Technology Letters*, vol. 17, no. 4, 2005.

[86] C. J. McKinstrie, S. Radic, and C. Xie, "Reduction of soliton phase jitter by in-line phase conjugation," *Optics Letters*, vol. 28, pp. 1519–1521, September 2003.

[87] K.-P. Ho, "Probability density of nonlinear phase noise," *Journal of Optical Society of America B*, vol. 20, pp. 1875–1879, September 2003.

[88] K.-P. Ho, "Asymptotic probability density of nonlinear phase noise," *Optics Letters*, vol. 28, pp. 1350–1352, September 2003.

[89] K.-P. Ho, "Performance degradation of phase-modulated systems due to nonlinear phase noise," *IEEE Photonics Technology Letters*, vol. 15, pp. 1213–1215, September 2003.

[90] C. J. McKinstrie, C. Xie, and T. Lakoba, "Efficient modeling of phase jitter in dispersion-managed soliton systems," *Optics Letters*, vol. 27, pp. 1887–1889, November 2002.

[91] M. Hanna, D. Boivin, P.-A. Lacourt, and J.-P. Goedgebuer, "Calculation of optical phase jitter in dispersion-managed systems by use of the moment method," *Journal of Optical Society of America B*, vol. 21, pp. 24–28, January 2004.

[92] D. Boivin, M. Hanna, P.-A. Lacourt, and J.-P. Goedgebuer, "Reduction of phase jitter in dispersion-managed systems by in-line filtering," *Optics Letters*, vol. 29, pp. 688–690, April 2004.

[93] C. J. McKinstrie, "Effect of filtering on gordon-haus timing jitter in dispersion-managed systems," *Journal of Optical Society of America B*, vol. 19, pp. 1275–1285, June 2002.

[94] S. K. Turitsyn, T. Schfer, and V. K. Mezentsev, "Generalized root-mean-square momentum method to describe chirped return-to-zero signal propagation in dispersion-managed fiber links," *IEEE Photonics Technology Letters*, vol. 11, pp. 203–205, February 1999.

[95] A. Mecozzi, J. D. Moores, H. A. Haus, and Y. Lai, "Soliton transmisson control," *Optics Letters*, vol. 16, pp. 1841–1843, December 1991.

[96] E. A. Golovchenko, J. M. Jacob, A. N. Pilipetskii, C. R. Menyuk, and G. M. Carter, "Dispersion-managed solitons in a fiber loop with in-line filtering," *Optics Letters*, vol. 22, pp. 289–291, March 1997.

[97] T. Georges, "Perturbation theory for the assessment of soliton transmission control," *Optical Fiber Technology*, vol. 1, pp. 97–116, November 1995.

[98] C. J. McKinstrie, C. Xie, and C. Xu, "Effects of cross-phase modulation on phase jitter in soliton systems with constant dispersion," *Optics Letters*, vol. 28, pp. 604–606, April 2003.

[99] M. Matsumoto, "Performance improvement of phase-shift-keying signal transmission by means of optical limiters using four-wave mixing in fibers," *Journal of Lightwave Technology*, vol. 23, pp. 2696–2701, September 2005.

[100] L. F. Mollenauer, J. P. Gordon, and S. G. Evangelides, "The slidind frequency guiding filter : an improved form of soliton jitter control," *Optics Letters*, vol. 17, pp. 1575–1577, November 1992.

[101] F. Favre and D. Leguen, "20 Gbit/s soliton transmission over 19Mm using sliding-frequency guiding filters," *Electronics Letters*, vol. 31, pp. 991–992, June 1995.

[102] L. F. Mollenauer, E. Lichtman, M. J. Neubelt, and G. T. Harvey, "Demonstration, using sliding-frequency guiding filters, of error-free soliton transmission over more than 20 mm at 10 Gbit/s, single channel, and over more than 13 mm at 20 Gbit/s in a two-channel WDM," *Electronics Letters*, vol. 29, pp. 910–911, May 1993.

[103] L. F. Mollenauer, P. V. Mamyshev, and M. J. Neubelt, "Measurement of timing jitter in filter-guided soliton transmission at 10 Gbit/s and achievement of 375-Gbit/s-Mm, error free, at 12.5 and 15 Gbit/s," *Optics Letters*, vol. 19, pp. 704–706, May 1994.

[104] E. A. Golovchenko, N. S. Bergano, and C. R. Davidson, "Four-wave mixing in multispan dispersion-managed transmission links," *IEEE Photonics Technology Letters*, vol. 10, pp. 1481–1483, October 1998.

[105] A. Mecozzi, "Probability density functions of the nonlinear phase noise," *Optics Letters*, vol. 29, pp. 673–675, April 2004.

[106] A. H. Gnauck and P. J. Winzer, "Optical phase-shift-keyed transmission," *Journal of Lightwave Technology*, vol. 23, pp. 115–130, January 2005.

[107] X. Wei, X. Liu, and C. Xu, "Numerical simulation of the SPM penalty in a 10-Gb/s RZ-DPSK system," *IEEE Photonics Technology Letters*, vol. 15, pp. 1636–1638, November 2003.

[108] C. C. Hiew, F. M. Abbou, H. T. Chuah, S. P. Majumder, and A. A. R. Hairul, "BER estimation of optical WDM RZ-DPSK systems through the differential phase Q," *IEEE Photonics Technology Letters*, vol. 16, December 2004.

[109] M. Hanna, H. Porte, J.-P. Goedgebuer, and W. T. Rhodes, "Experimental investigation of soliton optical phase jitter," *IEEE Journal of Quantum Electronics*, vol. 36, pp. 1333–1338, November 2000.

[110] E. L. Lehmann and G. Casella, *Theory of point estimation*. Springer-Verlag, New York, 1998.

[111] J. G. Proakis, *Digital Communications*. McGraw-Hill, 2001.

[112] T. Ono, Y. Yano, K. Fukuchi, T. Ito, H. Yamazaki, M. Yamaguchi, and K. Emura, "Characteristics of optical duobinary signals in Terabit/s capacity, high-spectral efficiency WDM systems," *Journal of Lightwave Technology*, vol. 16, pp. 788–797, May 1998.

[113] T. Ono and Y. Yano, "Key technologies for terabit/second WDM systems with high spectral efficiency of over 1 bit/s/Hz," *IEEE Journal of Quantum Electronic*, vol. 34, pp. 2080–2088, November 1998.

[114] S. Aisawa, J. Kani, M. Fukui, T. Sakamoto, M. Jinno, S. Norimatsu, M. Yamada, H. Ono, and K. Oguchi, "A 1580-nm band WDM transmission technology employing optical duobinary coding," *Journal of Lightwave Technology*, vol. 17, pp. 191–198, February 1999.

[115] T. Ito, T. Ono, Y. Yano, K. Fukuchi, H. Yamazaki, M. Yamaguchi, and K. Emura, "Feasibility study on over 1 Bit/s/Hz high spectral efficiency WDM with optical duobinary coding and polarization interleave multiplexing," pp. 43–45, in Proceedings of OFC'97, paper TuJ1, 1997.

[116] C. Xu, X. Liu, L. F. Mollenauer, and X. Wei, "Comparison of return-to-zero differential phase-shift keying and on-off keying in long-haul dispersion managed transmission," *IEEE Photonics Technology Letters*, vol. 15, pp. 617–619, April 2003.

[117] J. H. Sinsky, A. Adamiecki, A. Gnauck, C. A. Burrus, J. Leuthold, O. Wohlgemuth, S. Chandrasekhar, and A. Umbach, "RZ-DPSK transmission using a 42.7-Gb/s integrated balanced optical front end with record sensitivity," *Journal of Lightwave Technology*, vol. 22, pp. 180–185, January 2004.

[118] J. B. Anderson, T. Aulin, and C.-E. Sundberg, *Digital Phase Modulation*. New York: Plenum Press, 1986.

[119] S. Bigo, G. Charlet, and E. Corbel, "What has hybrid phase/intensity encoding brought to 40 Gbit/s ultralong-haul systems ?," in Proceedings of ECOC'04, Paper Th.2.5.1, 2004.

[120] F. Forghieri, P. R. Prucnal, R. W. Tkach, and A. R. Chraplyvy, "RZ versus NRZ in nonlinear WDM systems," *IEEE Photonics Technology Letters*, vol. 9, pp. 1035–1037, July 1997.

[121] K. S. Cheng and J. Conradi, "Reduction of pulse-to-pulse interaction using alternative RZ formats in 40-Gb/s systems," *IEEE Photonics Technology Letters*, vol. 14, pp. 98–100, January 2002.

[122] S. Appathurai, V. Mikhailov, R. I. Killey, and P. Bayvel, "Investigation of the optimum Alternate-Phase RZ format and its effectiveness in the suppression of intrachannel nonlinear distortion in 40-Gbit/s transmission over standard single-mode fiber," *IEEE Journal of Selected Topics in Quantum Electronics*, vol. 10, pp. 239–249, March/April 2004.

[123] P. V. Mamyshev and N. A. Mamysheva, "Pulse-overlapped dispersion-managed data transmission and intrachannel four-wave mixing," *Optics Letters*, vol. 24, pp. 1454–1456, November 1999.

[124] L. Boivin, M. C. Nuss, J. Shah, D. A. B. Miller, and H. A. Haus, "Receiver sensitivity improvement by impulsive coding," *IEEE Photonics Technology Letters*, vol. 9, pp. 684–686, May 1997.

[125] P. J. Winzer and A. Kalmár, "Sensitivity enhancement of optical receivers by impulsive coding," *Journal of Lightwave Technology*, vol. 17, February 1999.

[126] W. D. Cornwell, H. O. Edwards, N. H. Taylor, D. S. Lotay, S. A. Smith, and S. Hamidi, "Comparison of 64x10 Gb/s NRZ and RZ transmission over 6000 km using a dispersion-managed fiber solution," in Proceedings of OFC02, Paper WP4, 2002.

[127] C. Frst, G. Mohs, H. Geiger, and G. Fischer, "Performance limits of nonlinear RZ and NRZ coded transmission at 10 and 40 Gb/s on different fibers," in Proceedings of OFC00, Paper WM31, 2002.